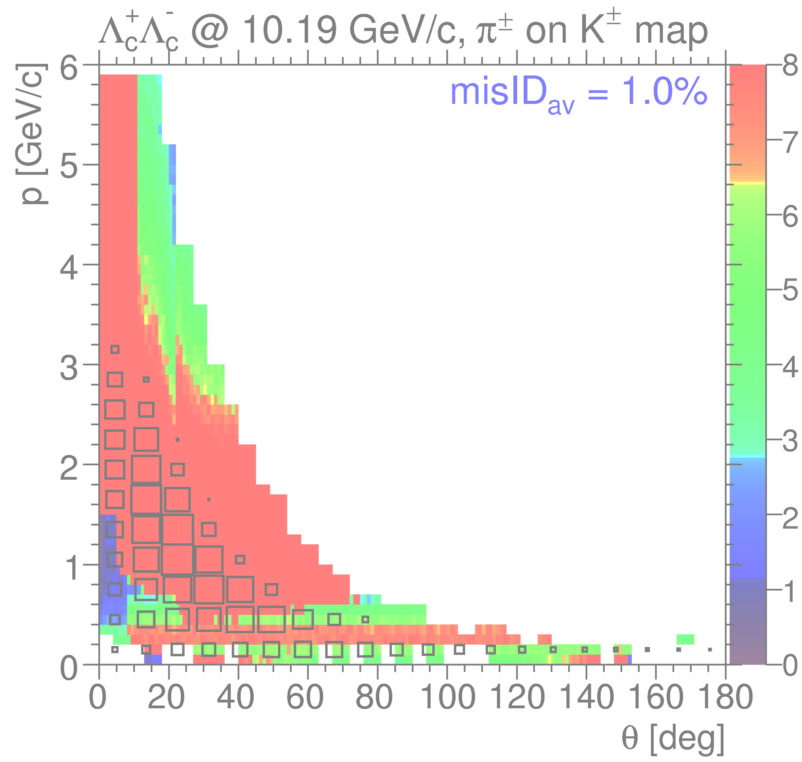


Particle Identification at $\bar{\text{P}}\text{ANDA}$

Report of the PID TAG



Draft 1.1

G. Schepers **et al.**

Contents

9	1 Introduction	4
10	2 Physics Requirements	5
11	3 PID Subsystems	6
12	3.1 Micro Vertex Detector (MVD)	8
13	3.2 Central Tracker	11
14	3.2.1 Time Projection Chamber (TPC)	11
15	3.2.2 Straw Tube Tracker (STT)	12
16	3.3 Barrel ToF	14
17	3.3.1 Barrel RPC TOF	15
18	3.3.2 TOF scintillator barrel	19
19	3.4 Barrel DIRC	21
20	3.5 Electromagnetic Calorimetry in the Target Spectrometer	23
21	3.5.1 PID Performance	24
22	3.5.2 Electron Identification	24
23	3.5.3 Afterpulse K^+ Identification	26
24	3.6 Endcap Cherenkov	27
25	3.6.1 Focussing Disc DIRC	27
26	3.6.2 Time of Propagation Disc DIRC	30
27	3.6.3 Proximity RICH	32
28	3.7 Muon Counter	33
29	3.7.1 Muon system overview	35
30	3.8 Forward RICH	36
31	3.9 Forward ToF	37
32	3.10 Forward Calorimeter	42
33	3.10.1 Electromagnetic calorimeter	42
34	3.10.2 Hadron calorimeter	44
35	4 Tools	44
36	4.1 Separation Power	45
37	4.1.1 Parameterization of the Electromagnetic Calorimeter	47
38	4.1.2 Mapping Separation Power	49

39	4.2	Phase Space Plots	50
40	4.3	Fast Simulation	58
41	4.3.1	General Technique	61
42	4.3.2	Tracking Detectors	63
43	4.3.3	Energy Loss Parameterization	63
44	4.3.4	Cherenkov Angle Parameterization	63
45	4.3.5	Time Of Flight Parameterization	66
46	4.3.6	Parameter Settings	68
47	5	Evaluation	69
48	5.1	Maps of Separation	69
49	5.2	Crucial channels	76
50	5.2.1	$\bar{p}p \rightarrow \Lambda^0 \bar{\Lambda}^0$ at 1.46 GeV/c (π/e), fig. 59	76
51	5.2.2	$\bar{p}p \rightarrow \Omega^- \bar{\Omega}^+$ at 4.954 GeV/c (p/K), fig. 59	76
52	5.2.3	$\bar{p}p \rightarrow D^0 \bar{D}^0 \gamma$ at 6.488 GeV/c (K/p), fig. 59	76
53	5.2.4	$\bar{p}p \rightarrow \Lambda_c^+ \Lambda_c^-$ at 10.187 GeV/c (π/K), fig. 61	76
54	6	Global PID Scheme	77
55	7	Conclusion	78
56	8	Acknowledgments	80
57	9	Appendix	83

1 Introduction

The $\bar{\text{PANDA}}$ ([1]) PID TAG (Particle Identification Technical Assessment Group) was installed to give to the collaboration a complete set of parameters for the evaluation of the optimal combination of particle detectors.

The task given to this TAG is described in more detail:

Subject

- Requirements from physics
- Evaluate potential of each subsystem
- Matching of systems

Deliverables

- Definition of global PID scheme
- Optimized set of detectors and parameters

This list reflects roughly the structure of the PID TAG work and of this report. In an additional subsection the tools available for the PID TAG work are presented and explained (see also [2]) .

The PID TAG evaluated the necessity of mapping the "Separation Power" in dependence of the momentum and the polar angle of the reaction products which is described in section 4.1. Since a "full simulation" was not available to calculate the performance of all the sub detectors, the TAG gathered parameterizations of the single sub detectors which went into a "Fast Simulation" explained in section 4.3. For single physics channels a "Full Simulation" was used.

Amongst others some important questions to solve were:

- PID informations from the Central Tracker (Straw Tube Tracker (STT) or Time Projection Chamber (TPC))
- PID with and without a Barrel ToF detector
- PID with and without Forward End cap Cherenkov, and with different designs (Focusing Disc DIRC, Time of Propagation Disc DIRC and Proximity RICH)
- PID with and with out a Forward RICH

For special subjects experts were asked to present informations in the meeting or to give answers to questions which arose.

The members of the TAG and their special responsibilities are listed at the end of the document (section 9).

2 Physics Requirements

The HESR (High Energy Storage Ring) of the new FAIR (Facility for antiproton and Ion Research) project provides an antiproton beam of high resolution (down to $\Delta p = 1 \times 10^{-5}$) and intensity from 1.5 GeV/c to 15 GeV/c momentum.

This offers the unique possibility of investigating a broad field of physics. The vast variety of reaction types from meson-production over Charmonium decays to Hyper nuclear reactions demands a complete and compact detector system.

The physics requirements to the detectors are:

- to cover the full angular range of the physics products
- to detect all momenta of the reaction products
- to separate particle types with a defined level of separation over the full range of momenta of the reaction products.

The full solid angle can only be covered by the full set of detectors. Sometimes the momentum coverage has to be fulfilled by a combination of two or even three sub detectors.

The rich experimental program can only be pursued with a universal and hermetic detector capable of detecting charged and neutral particles with nearly 4 solid angle coverage and high resolution.

The basic elements are:

Hidden-charm physics and the search for exotics require the concurrent detection of lepton pairs as well as good kaon identification and high efficiency for open-charm final states. In addition, the detection of low energy photons, either from radiative decays and/or background channels, is extremely important. The same, muon detection capability and a highly-segmented low-threshold electromagnetic calorimeter are important for the tagging and precise reconstruction of hidden-charm and the reduction of background. Good vertex recognition and particle identification for charged kaons from very low energies up to a few GeV/c is mandatory to reconstruct light hadronic and open charm final states.

The detector must withstand large radiation dosage from hadrons emitted from the spallation process when using nuclear targets. Spallation products are dominated by neutrons down to thermal energies.

The specific demands for experiments with a secondary target require good detection of antihyperons and low momentum K⁺ in the forward region. A compact high resolution solid state tracker for absorption and tracking of low momentum hyperons at large angles is needed. The geometry of the secondary target is determined by the short mean life time of the Ξ^- of only 0.164 ns. A high resolution and high efficiency Ge-array for γ -ray detection is envisaged in order to measure radiative transitions.

Open-charm spectroscopy and electromagnetic reactions have similar demands as are envisaged in the hidden-charm and exotics programs that the decay of a charmed hadron releases rather high pt (up to 1.5 GeV/c) as compared to light and even strange meson decays. This leads to large opening angles of particles in the laboratory reference frame.

At $\bar{\text{PANDA}}$ 2×10^7 reactions per second with 2.5 to 3.8 charged particle tracks for 2 and 15 GeV/c respectively have to be digested by the detectors.

Most of the channels of interest are expected to have very low cross sections which are typically in the order of nb or pb. Due to the fact that the total $\bar{p}p$ cross section is more than 40 mb in the energy regime of the $\bar{\text{PANDA}}$ measurements, a good background rejection power is mandatory. The most important criteria for the distinction between the signals and the huge amount of background events are in general

- the kinematics, which is especially very helpful for exclusive measurements,
- the accurate reconstruction of decay vertices for particles like D or D^* mesons, and
- an efficient and clean identification of the different particle species.

The necessity of a powerful particle identification with the $\bar{\text{PANDA}}$ detector becomes more clear with Table 1. This table shows a comparison between the cross sections of some channels which are planned to be measured with $\bar{\text{PANDA}}$ and of the corresponding major background modes. It should be noted that most of the numbers are based on assumptions only. Due to the fact that the branching ratios of some specific decay modes are very small a rejection power of up to 10^{12} has to be achieved. For these channels detailed feasibility studies have already been done and the results are summarized in the $\bar{\text{PANDA}}$ Physics Book [3].

The identification of the different final states has to be provided by single subdetectors or groups of subdetectors described in the following section.

3 PID Subsystems

The different behavior of charged particles traversing active and passive detector material can be used to identify (on a probabilistic level) the nature of a charged particle. The PID detectors used in PANDA take advantage of the following effects:

- **Specific Energy Loss.** The mean energy loss of charged particles per unit length, usually referred to as dE/dx , is described by the Bethe-Bloch equation which depends on the velocity rather than momentum of the charged particle.
- **Cherenkov Effect.** Charged particles in a medium with refractive index n propagating with velocity $\beta > 1/n$ emit radiation at an angle $\Theta_C = \arccos(1/n\beta)$ with Θ_C being the Cherenkov angle. Thus, the mass of the detected particle can be determined by combining the velocity information obtained from Θ_C with momentum information from the tracking detectors.
- **Time-of-flight.** Particles with the same momentum, but different masses travel with different velocities, thus reaching a time-of-flight counter at different times relative to a common start.
- **Absorption.** A thick layer of passive material absorb most particles due to electromagnetic ($e+e-, \gamma$) or hadronic interactions (all charged and neutral hadrons). After a certain amount of material only muons and neutrinos survive. The muons can then be detected easily with any kind of charged particle detector, depending on the desired speed and resolution.

Physics Case	Signal Channel	Background Channel	Final State	$\sigma \cdot \mathcal{BR}$ (estimate)	s/bg ratio	PID challenge
Charmonium Spectroscopy	$Y(4260) \rightarrow J/\psi 2\pi^\pm$	$2\pi^+ 2\pi^-$	$2e^\pm 2\pi^\pm$ $4\pi^\pm$	60 pb 46 μb	$1 \cdot 10^{-6}$	e/ π sep.
	$Y(4260) \rightarrow J/\psi 2\pi^0$	$\pi^+ \pi^- 2\pi^0$	$e^+ e^- 4\gamma$ $2\pi^\pm 4\gamma$	30 pb 50 μb	$6 \cdot 10^{-7}$	e/ π sep.
	$X(3872) \rightarrow J/\psi \eta$	$\pi^+ \pi^- \pi^0$	$e^+ e^- 2\gamma$ $2\pi^\pm 2\gamma$	20 pb 290 μb	$7 \cdot 10^{-8}$	e/ π sep.
	$\chi_c \rightarrow J/\psi \gamma$	$\pi^+ \pi^- \pi^0$	$e^+ e^- \gamma$ $2\pi^\pm 2\gamma$	0.8 nb 0.29 mb	$2 \cdot 10^{-6}$	e/ π sep.
	$h_c \rightarrow \eta_c \gamma \rightarrow 2\Phi \gamma$	$\Delta^{++} \Delta^{--} \pi^0$ $4\pi^\pm \pi^0$	$4K^\pm \gamma$ $\bar{p}p 2\pi^\pm 2\gamma$ $4\pi^\pm 2\gamma$	20 pb 530 μb 750 μb	$4 \cdot 10^{-8}$ $3 \cdot 10^{-8}$	p/K/ π sep.
	$\psi(3770)$	$\bar{p}p \rightarrow X$	$2K^\pm 4\pi^\pm$ X	14 pb 60 mb	$2 \cdot 10^{-10}$	K/ π sep.
	$\psi(4040) \rightarrow D^* \bar{D}^*$	$\bar{p}p \rightarrow X$	$2K^\pm 4\pi^\pm$ X	0.46 pb 60 mb	$1 \cdot 10^{-11}$	K/ π sep.
Exotics	$\eta_{c1} \eta \rightarrow DD^* \eta$	$\bar{p}p \rightarrow X$	$2K^\pm 2\pi^\pm 8\gamma$ X	0.06 pb 50 mb	$1 \cdot 10^{-12}$	K/ π sep.
	$\xi(2230) \rightarrow 2\Phi$	$\bar{p}p \rightarrow X$	$4K^\pm$ X	3 nb 60 mb	$5 \cdot 10^{-8}$	K/ π sep.
Baryon Production	$\Xi^+ \Xi^-$	$\bar{p}p \rightarrow X$	$\bar{p}p 4\pi^\pm$ X	1 μb 60 mb	$2 \cdot 10^{-5}$	
Electromagn. Formfactors	$\bar{p}p \rightarrow e^+ e^-^a$	$\bar{p}p \rightarrow \pi^+ \pi^-$	$e^+ e^-$ $\pi^+ \pi^-$		$2 \cdot 10^{-6}$	e/ π sep.
Drell-Yan Process	$\bar{p}p \rightarrow \mu^+ \mu^- X$	$\bar{p}p \rightarrow X$	$\mu^+ \mu^- X$ X	60 mb	?	μ/π sep.
Hadrons in Nuclear Medium	$\bar{p}^{40}\text{Ca} \rightarrow J/\psi X$	$\bar{p}^{40}\text{Ca} \rightarrow X$	$e^+ e^- X$ X	0.3 nb 1 b	$3 \cdot 10^{-10}$	e/ π sep.

^a s=8.2 GeV² in the angular range of $|\cos(\Theta_{CMS})| < 0.8$

Table 1: Comparison between the cross sections of some important channels which are planned to be investigated with $\bar{\text{P}}\text{ANDA}$ and the cross sections of the corresponding major background where a good separation of the various particle species is mandatory. Since most of the channels could not be measured so far, the cross sections are mainly based on rough assumptions. The numbers have been extracted from the $\bar{\text{P}}\text{ANDA}$ Physics Book [3].

The subsystems building the particle identification system of $\bar{\text{P}}\text{ANDA}$ are listed with growing distance to the Target point:

- Time Projection Chamber (TPC)
- Staw Tube Tracker (STT)
- Barrel Time of Flight Detector (ToF)
- Barrel DIRC
- Electromagnetic Calorimeter (EMC)

- Endcap Cherenkov Detector
- Muon Counter
- Forward Cherenkov Detector
- Forward Time of Flight Detector
- Forward Calorimeter

3.1 Micro Vertex Detector (MVD)

The Micro Vertex Detector will provide precise space point measurements for particle tracking and the reconstruction of decay vertices. The detector will be build of state-of-the-art silicon semiconductor detector layers of pixel and strip type. A schematic overview is given in figure 1.

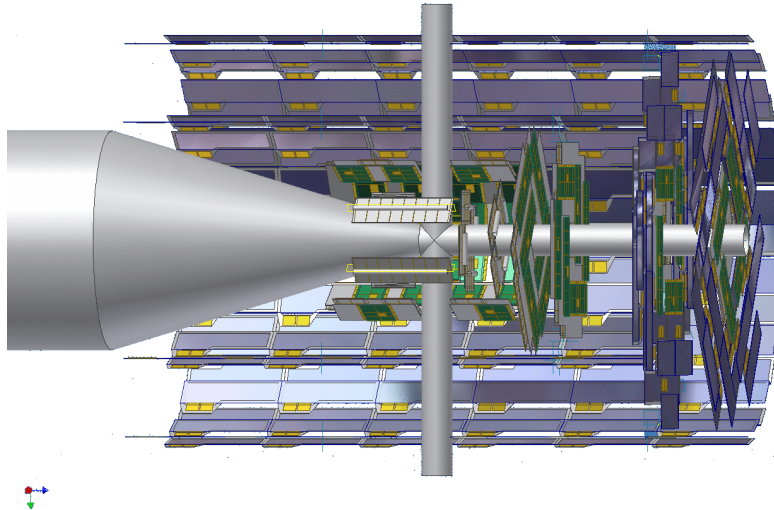


Figure 1: Artist view of the MVD design together with beam and target pipe cross. A half shell of the barrel section has been removed for insight. The inner detector elements (green) are pixel sensors, the outer (blue) are strip sensors.

Although the number of reconstructed MVD hit points per track is limited to 4 in the barrel section and 5-6 in the forward domain the energy loss information provided by the readout electronics can be used as part of the particle identification decision. The ability of separating different particle species relies on an accurate energy loss information and a good knowledge of the track position with respect to the sensors. Figure 2 shows the computed dE/dx information for tracks of different particle types in a momentum range from 50 MeV/c to 1.2 GeV/c.

In general the MVD might be able to contribute to the global PID for particle momenta below ≈ 600 MeV/c. Protons (highest band) and kaons (middle) can be separated from pions, muons and electrons (lowest band). In Figure 2,b) a typical dE/dx signal for protons with momentum of 400 MeV/c is shown. The signal can only be described sufficiently by a convolution of a gaussian

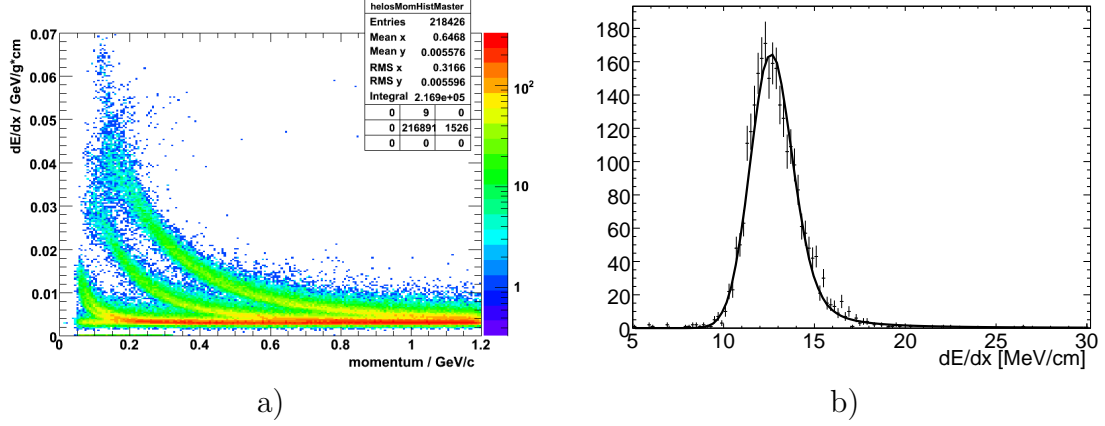


Figure 2: Energy loss information for different particle species and its dependence on momentum (a). The upper band corresponds to protons, whereas the middle band shows kaons and the lowest band is a superposition of pions, muons and electrons. Part (b) shows an individual fit of the dE/dx signal from protons with a momentum of 400 MeV/c.

and a Landau component by using:

$$w(s) = \int L(x) G(s - x) dx \quad (1)$$

The used parameterizations are

$$G_{\sigma}(x) = \frac{1}{\sqrt{2\pi}\sigma} e^{-x^2/\sigma^2} \quad (2)$$

for the Gauss distribution and

$$L_{\tau}(x) = \frac{1}{\pi\tau} \int_0^{\infty} e^{-t(\ln t - x/\tau)} \sin(\pi t) dt \quad (3)$$

for the scaled Landau distribution. The sensors, where the deposited charge is collected, are very thin silicon devices of typical thicknesses of 200 – 300 μm . Therefore the energy signal will be dominated by Landau fluctuations, which can not be fully suppressed by a truncated mean method. The remaining tail for the proton signal is still visible in figure 2,b). The dE/dx signal can be then described by only three parameters, the Gauss width σ_G , σ_{τ} respectively for the Landau width and s , which is the most probable value of the Landau distribution.

The dE/dx bands for individual particle types are following the well known Bethe-Bloch relation given in equation 19 in section 4.3.3. The method described here makes use of a full detector simulation using a combined tracking of the MVD and the outer tracking detectors. To very low momenta the momentum uncertainty increases, which causes a widening of the individual bands. In order to estimate the separation ability the momentum axis has been divided in 25 MeV/c wide bins and for each bin the shape of the the dE/dx distribution has been determined. The momentum dependence of the three parameters σ_G , σ_{τ} and s was input for the probability for each particle type. Based on the obtained parameterizations for each particle type and each track the probability was calculated and input for the global PID decision.

The likelihood for proton trajectories is shown in Figure 3. The upper picture shows the calculated proton probability and its dependence with momentum. The figure shows in addition the

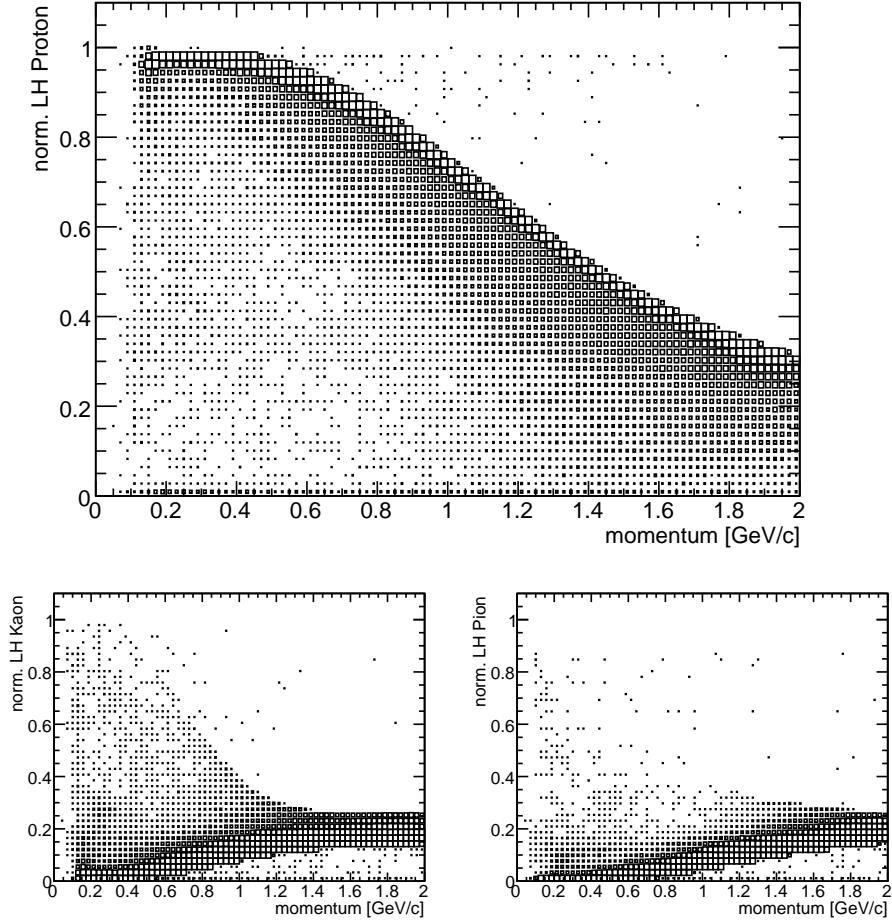


Figure 3: Computed normalized likelihood for proton tracks in a momentum range $p = 0.1 \dots 2.0$ GeV/c. The upper picture show the proton probability, whereas the lower left shows the kaon misidentification probability and the lower right the pion miss identification, respectively.)

210 probability to misidentify the track as kaon (lower left), or pion (lower right) respectively. Muons
 211 and electrons can not be further separated from each other and their probability is equal to the
 212 pion case. The calculation takes the full convolution integral into account which causes a smearing
 213 to lower likelihood values apart from the maximum value.

214 As explained above the calculation was done for fully reconstructed single particle events under
 215 the assumption of equal abundance¹. Several additional error sources have not been considered
 216 and will be subject to further investigation. The properties of the front end electronics are not
 217 yet fully fixed and an additional uncertainty ΔdE was omitted. This is usually in the order of a
 218 few percent but depending on the gain of the energy measurement of the front end. The sensors
 219 were assumed to be perfectly aligned. The position calibration in the final experiment has to be
 220 in the order of the hit reconstruction accuracy in order to avoid a larger additional smearing.

¹This is not true for most physics channels and in particular for annihilation background, e.g. strange production is suppressed, but a common way to compare directly the efficiency for particular particle types.

The MVD can contribute to the global PID in the momentum region below 1 GeV/c to separate protons and kaons from the other particle species. It is therefore together with the outer tracking detector complementary to the DIRC measurement and can improve the global PID information.

3.2 Central Tracker

Since the central tracker depending on the detector type provides as a surplus a dE/dx-information it can give important help for the particle identification in the low momentum regime ($< 700\text{MeV}$). For PANDA there are two options for the central tracker which are a Straw Tube Tracker on the one hand and a Time Projection Chamber on the other hand.

3.2.1 Time Projection Chamber (TPC)

The working principle of a GEM-based TPC and the geometrical design of the PANDA TPC [1] are sketched in Figs. 4a and 4b. Charged particles traversing the detector volume ionize the counting gas and an electric field separates positive ions from electrons. The cylinder axis of the TPC coincides with the direction of the electrical field lines and also the direction of the solenoid magnetic field of the target spectrometer. The primary electrons drift towards an amplification stage, which consists of a triple-GEM stack. No gating grid is foreseen for the PANDA TPC to allow a continuous operation at the HESR antiproton storage ring. In order to keep the build-up of space charge inside the drift volume at a minimum, the back flow of slow ions from the amplification stage has to be suppressed as much as possible. GEM foils [4] offer an intrinsic ion suppression if the settings of the whole stack are optimized accordingly. A continuous readout including online tracklet reconstruction is envisaged for the TPC.

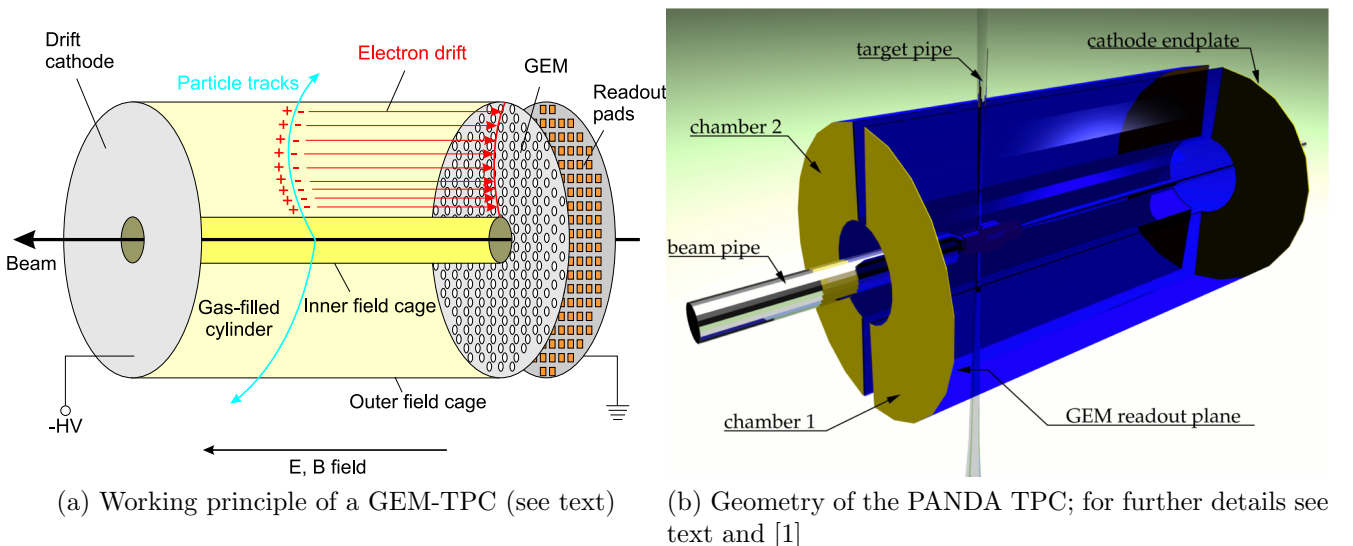


Figure 4: Time Projection Chamber

In order to accommodate the target pipe, the TPC is split into two half-cylinders of a length of 150 cm. The inner and outer radius is 15 cm and 42 cm, respectively. 65 000 to 100 000 pads of an area of $4\text{-}6\text{ mm}^2$ are planned. A Ne/CO₂ gas mixture (90/10), possibly with a small admixture

of CH_4 , and a gain of a few thousand are furthermore foreseen. The drift field is 400 V/cm. Under these conditions ≈ 50 -100 energy loss measurements per track are feasible. This allows, in combination with a truncated mean algorithm, the identification of charged particles via their mean energy loss per track length dE/dx (Bethe-Bloch-formula, see equation 19). The TPC therefore contributes significantly to the overall PID performance of PANDA, in particular in the momentum regime below $1 \text{ GeV}/c^2$. In Fig. 5 the energy loss distributions for different particle types are shown up to $1.5 \text{ GeV}/c^2$. The plot has been obtained from the “Fast Simulation” described in section 4.3 assuming a dE/dx resolution of 8% for the TPC (cf. table 10).

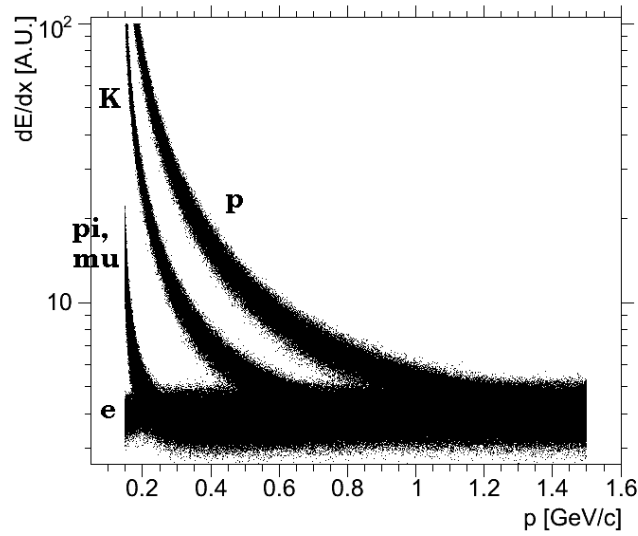


Figure 5: Energy loss in the TPC vs. particle momentum up to $1.5 \text{ GeV}/c^2$.

3.2.2 Straw Tube Tracker (STT)

The single straw tube is a gas filled tube with a wire along its axis. The wire is the anode the inner conductive wall is the cathode and a high voltage of some kV is applied between the two. An electric field is then present in the gas filled area: when a charged particle transverses it, ionization takes place; the electrons drift toward the wire, while the ions drift toward the wall. Once the electrons are near enough to the wire ($\simeq 50 \mu\text{m}$), an avalanche multiplication takes place with an amplification of $10^4 - 10^5$ of the primary charge signal which allows the readout of the electric signal. Concerning the gas choice, it is necessary to find a compromise between the material budget, which must be small to minimize the multiple scattering, and a good spatial resolution. An Ar/ CO_2 gas mixture (90/10) has been chosen, since the simulations with Garfield [5] have demonstrated that even though He would give a lower material budget, it would worsen the resolution. The arrival time of the signal defines the drift radius and the charge collected is proportional to the particle energy lost by ionization.

The Straw Tube Tracker consists of an ensemble of 150 cm long drift tubes, arranged in an hexagonal shape around the beam axis. The present solution consists of 4204 tubes, arranged in double layers, 2800 of which parallel to the beam axis, the others inclined with respect to the beam

STT characteristics		
internal radius	15	cm
external radius	42	cm
skew angle	3°	
tube wall thickness	30	μm
tube diameter	1.006	cm
tube standard length	150	cm
wire diameter	20	μm
wall material	mylar	
wire material	gold plated W	
gas mixture	2 atm argon Ar/CO ₂ (90/10)	
transparency X/X_0	< 1%	
r - ϕ plane resolution	< 100 μm	

Table 2: Dimensions and material budget of the Straw Tube detector. X/X_0 is the thickness expressed as the radiation length fraction. The quantities listed in this table are under study and the final layout of the STT could be different.

axis (skewed tubes); the skewed tubes are necessary to allow the z coordinate determination. The present layout of the Straw Tube tracker is shown in fig.6. The tubes in two consecutive layers are staggered in order to resolve the left-right ambiguity.

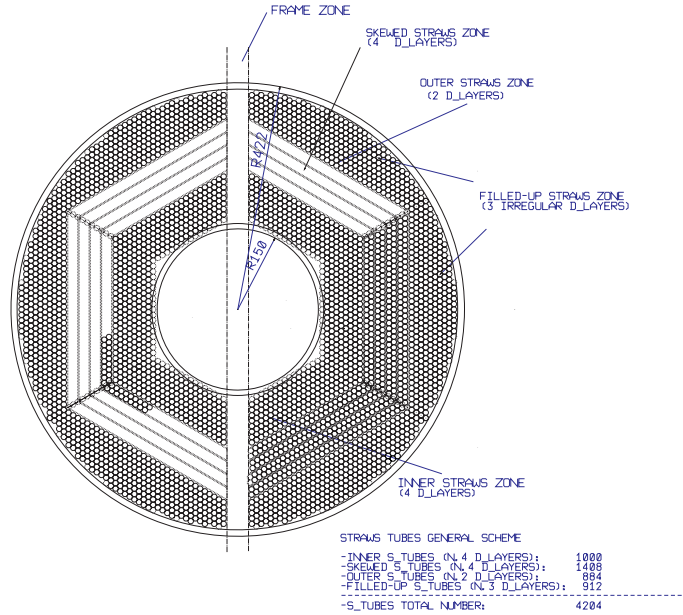


Figure 6: Present layout of Straw Tube Tracker

270

271 The geometric characteristics used for the simulations are summarized in tab.2. Among the STT
272 advantages we recall:

273

- the small signal's cross-talk;

- the insensitivity of neighboring straws in case of broken wires;
- the high mechanical stability if the straws are arranged in close-packed multi-layers;
- the high tracking efficiency;
- the good spatial resolutions
- the high rate capability.

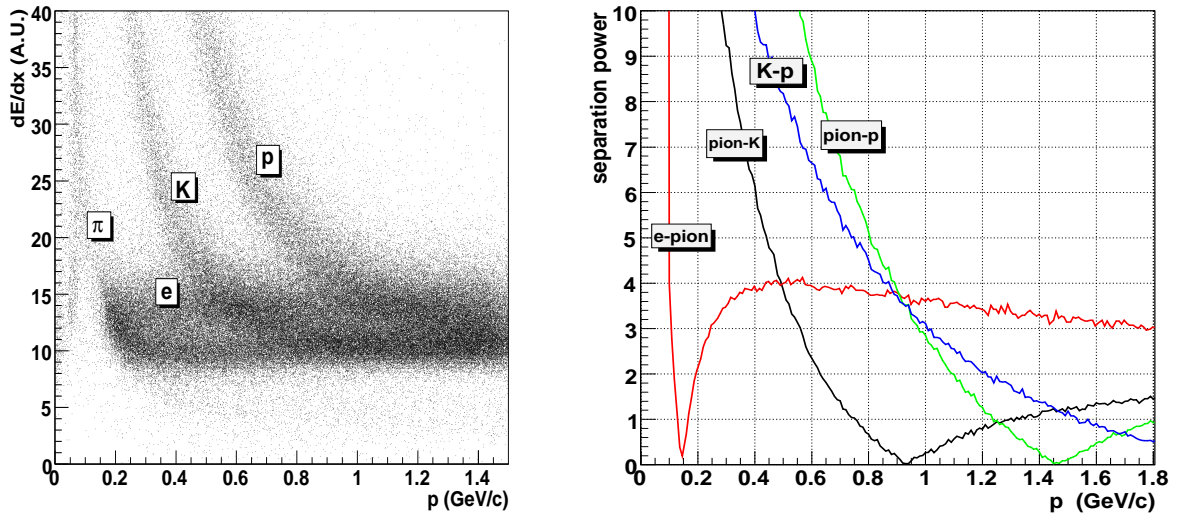


Figure 7: Energy loss by a 40% truncated mean algorithm for various particles vs the reconstructed momentum (left) and corresponding separation power (right) in the STT detector.

For a 1 GeV track, the STT detector allows about 25 energy loss measurements. We considered a sample of simulated tracks fully reconstructed with the helix fit. In each tube, the deposited energy has been reproduced with the detailed simulation of the cluster formation, charge multiplication and collection, whereas the radial path has been reconstructed by the measured drift radius and by the dip angle resulting from the helix fit.

The 40% truncated mean of these sampled dE/dx values is reported in fig 7 (left), whereas the corresponding separation power is shown in fig. 7 (right). These results clearly demonstrates the capability of the STT detector in the low energy PID.

3.3 Barrel ToF

The Barrel Time-of-Flight detector (TOF) has to be placed inside the solenoidal magnet to provide the identification of soft particles at large polar angles from 22 to 140 degrees. The required resolution of the Barrel TOF detector has to be better than 100 ps. It is assumed the Barrel TOF will consist of separate modules arranged around the tracking detector, TPC or STT. The proposed length of the TOF is about 190 cm, the inner radius is 48 cm. Two variants of the Barrel TOF detector are presented: Resistive Plate Chambers TOF and Scintillator TOF.

3.3.1 Barrel RPC TOF

The recently developed timing Resistive Plate Chambers (RPC) in principle offers the required resolution of better than 70 ps and almost 100% detection efficiency (see Fig. 8 and [6]). With these parameters, identification of pions, kaons and protons becomes possible up to a few GeV/c. A stable operation of such RPCs was observed in extensive tests during many years in various experiments. The RPCs were found to be fully efficient and low-noise chambers. One of useful feature of the RPC is its immunity to magnetic field. Choice of RPC type for the PANDA barrel TOF should be made basing on specific requirements, including time resolution and its rate dependence, as well as radiation hardness. Two RPC options are discussed below: HARP-type RPC (developed by IHEP-JINR) and single-cell DRPC (developed by ITEP).

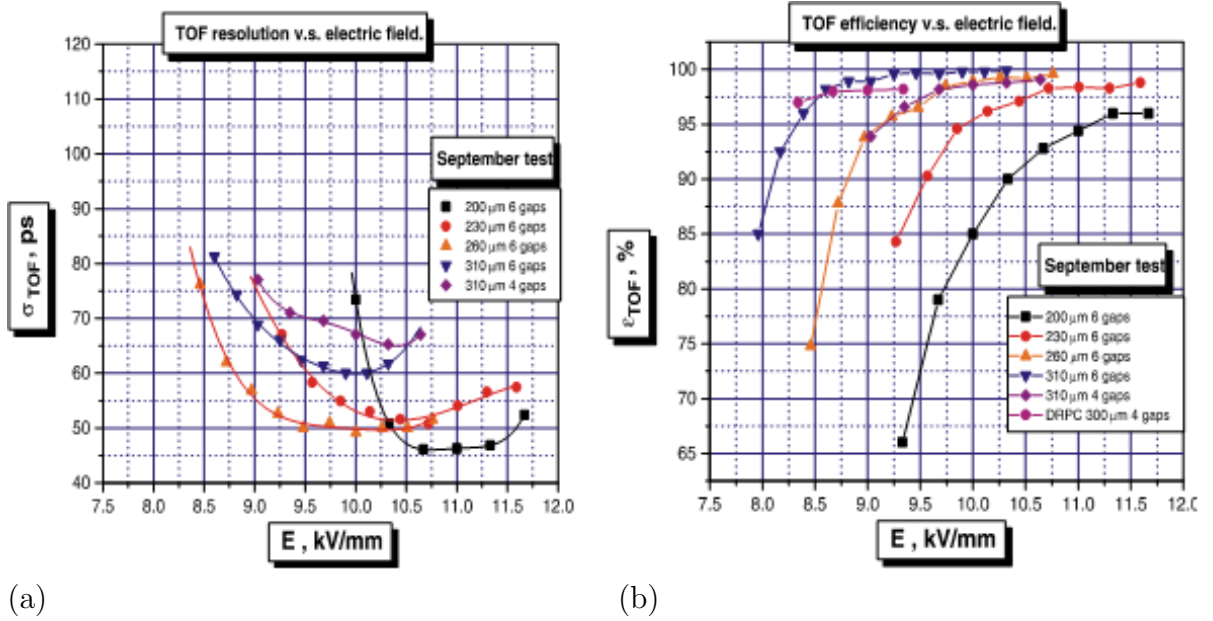


Figure 8: (a) Time resolutions and (b) efficiencies of different RPC types.

HARP-type RPC TOF The design proposed here is based on experience obtained during the work for the HARP experiment [7]. The RPC-TOF consists of 11 modules arranged around the central tracker in the way shown schematically in Fig. 9. The length of each module is ~ 190 cm, the width of its active area is ~ 30 cm.

Each module is a multi-gap glass RPC placed inside aluminum case. To have a full coverage in the azimuthal angle, the active areas of neighbor modules will be overlapped as it is shown in left Fig. 9. PCB with FEE electronics will go along both long sides.

Because of hard demands on the amount of material for the Barrel-TOF detector, a variant of the four-gap glass RPC was chosen (see right Fig. 9). A beam test [8] of a four-gap RPCs has demonstrated that a time resolution of ~ 75 ps can be reached even with the old HARP FEE. The RPCs can be made from a "standard" float glass with thickness of 0.6 mm. The gaps between glass plates are kept with spacers made of fishing line. The thickness of the TOF module (including aluminum box) is $X/X_0 \approx 6.0\%$.

Each RPC will be equipped with 64 strips with a double ended readout. Each strip has a length

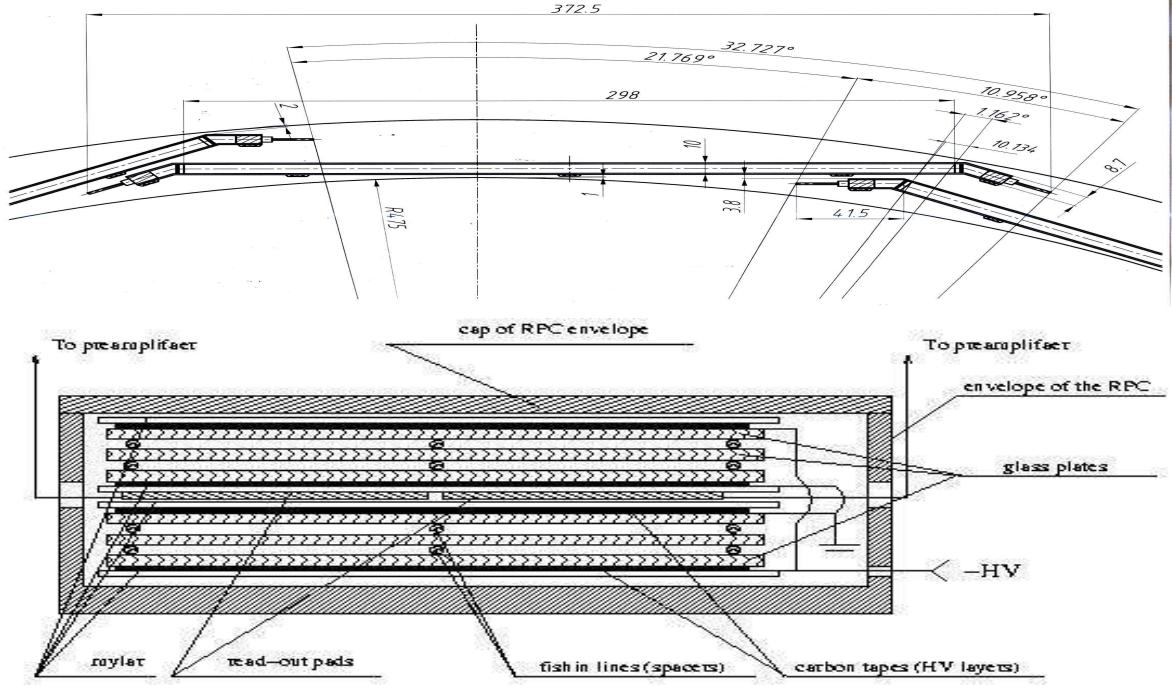


Figure 9: Possible arrangement of 11 barrel RPCs (left figure) and Four-gap RPC. Cross-section through its short side (right figure).

of ~ 30 cm at 30 mm width. Already existing data [9] on multi-gap RPC with strips (strip length: 95 cm and width: 25mm) inspire a hope that time resolution of 60-70 ps can be reached with double-end readout. The signals will be amplified and digitized at the RPCs to use the Time-Over-Threshold (TOT) method for slewing correction as it was proposed in [10]. The total number of HPTDC channels needed to read all strips is about ~ 1410 . The development of the read-out system has to be a major task during R&D study for the PANDA RPC.

A set of eleven TOF modules having total gas volume of ~ 60 liters is operating with a non-flammable gas mixture containing 90%*R134A*, 5% isobutane and 5%*SF₆*. The flows of three gas components are metered with "electronic mass flow meters". At total flow rate of about $200 \text{ cm}^3/\text{min}$, a gas exchange of one volume will be every ~ 5 hours. The TOF modules are supplied with gas in groups, say, of four. Each group has its own control and protection systems. Very important question is the **rate capability**. Since the bulk resistivity of glass is $\sim 10^{13} \Omega \cdot \text{cm}$, the rate capability of a glass RPC could bring a potential problem due to the time needed to neutralize the charge deposited on the resistive plates after discharge inside the gas gaps. During measurements performed in the GIF test area for the ALICE TOF detector, it was observed that there was no deterioration of the efficiency and the resolution for the ALICE MRPCs up to $1 \text{ kHz}/\text{cm}^2$. This result found for 10-gap glass RPC should be well for a four-gap chamber too. The estimations using the DPM generator for minimal bias events showed that particle flux in the PANDA barrel for momenta of the incident anti-proton between $1.5 \text{ GeV}/c$ and $15 \text{ GeV}/c$ is less than $1 \text{ kHz}/\text{cm}^2$.

Particle Identification. The Barrel RPC-TOF provides a particle identification using a mea-

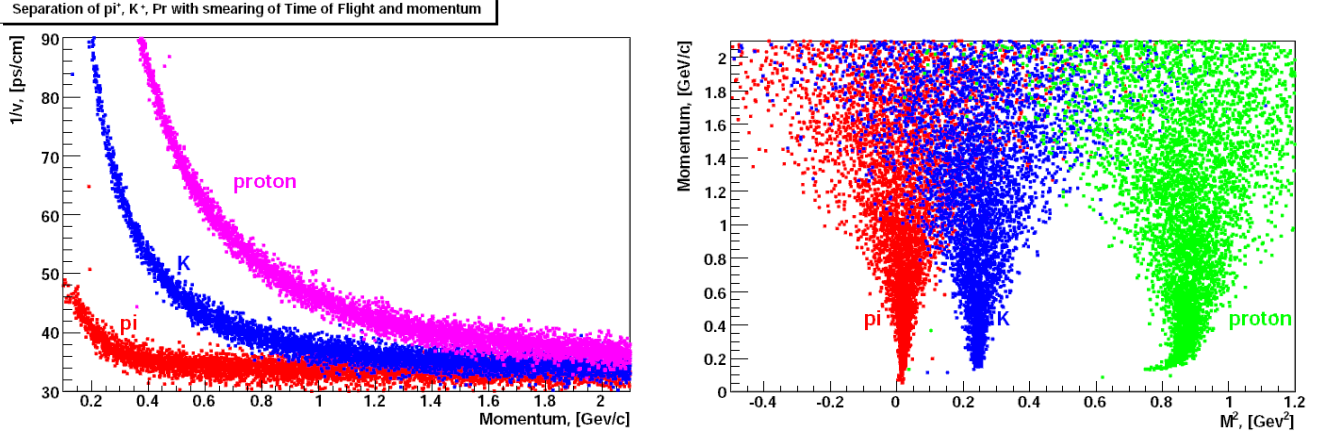


Figure 10: Inverse velocity of particles vs. momentum (left figure) and momentum of particles vs. squared mass reconstructed with RPC-TOF (right figure).

surement of a particle arrival time and a momentum and length of a track information from the tracking detectors (TPC or STT). In the PandaRoot framework, we generated events of K, Pi, proton production isotropically through the RPC-TOF with momenta from 0.1 to 2.1 GeV/c. We simulated and reconstructed the events using RPC-TOF, and calculated velocity and squared mass of the particles by the formulas: $1/v = t/l$ and $M^2 = P^2(1/v^2 - 1)$. Fig. 10 gives the results of a particle identification using the $1/v$ and the M^2 information from the RPC-TOF.

Separation power. Fig. 11 shows calculation of a separation power. The difference between time of flight of two different particles divided by the TOF resolution, $(t_1 - t_2)/\sigma_t$ ("separation power"), is presented in Fig. 11 for different pairs of particles for the most hard case - for polar angle $\Theta = 90^\circ$, and for polar angle $\Theta = 30^\circ$. The computation was done for two values of σ_t : 70 ps and 100 ps.

The calculations of the separation power for angle $\Theta = 30^\circ$ demonstrate that the barrel TOF with resolution of ~ 70 ps will be able to identify hadrons with momentum up to few GeV/c. The RPC-TOF providing the particle identification at low momentum can be a good supplement to the DIRC.

Furthermore, the RPC-TOF can help as a reference detector for the one-dimensional DIRC.

In ideal case, the time-of-flight is measured with information from two detectors: start time, t_0 , from a reference detector placed somewhere near the target and a stop time of flight t from the barrel TOF. However, even in case of no start detector, t_0 can be found by fitting measured values of t in multi particle events with different hypothesis.

Single-cell DRPC TOF The suggested design of the DRPC-based TOF system (hereinafter, DRPC-TOF) consists of 124 identical modules (two modules are joined in the center of the system) arranged around the central tracker in the way shown in Fig. 12. The average barrel radius is 50 cm and its total system thickness is about 7 cm.

Such setup guarantees 100% geometrical efficiency even in case of a zero magnetic field and straight tracks. The length of each module is 90 cm, the width of its active area is 5 cm. Each module contains 18 DRPC cells with 4 or 6 gas gaps sized 5×5 cm² attached on both sides to a multi layer PCB. The PCB is also used to route signals from the FEE to the readout electronics (TDC

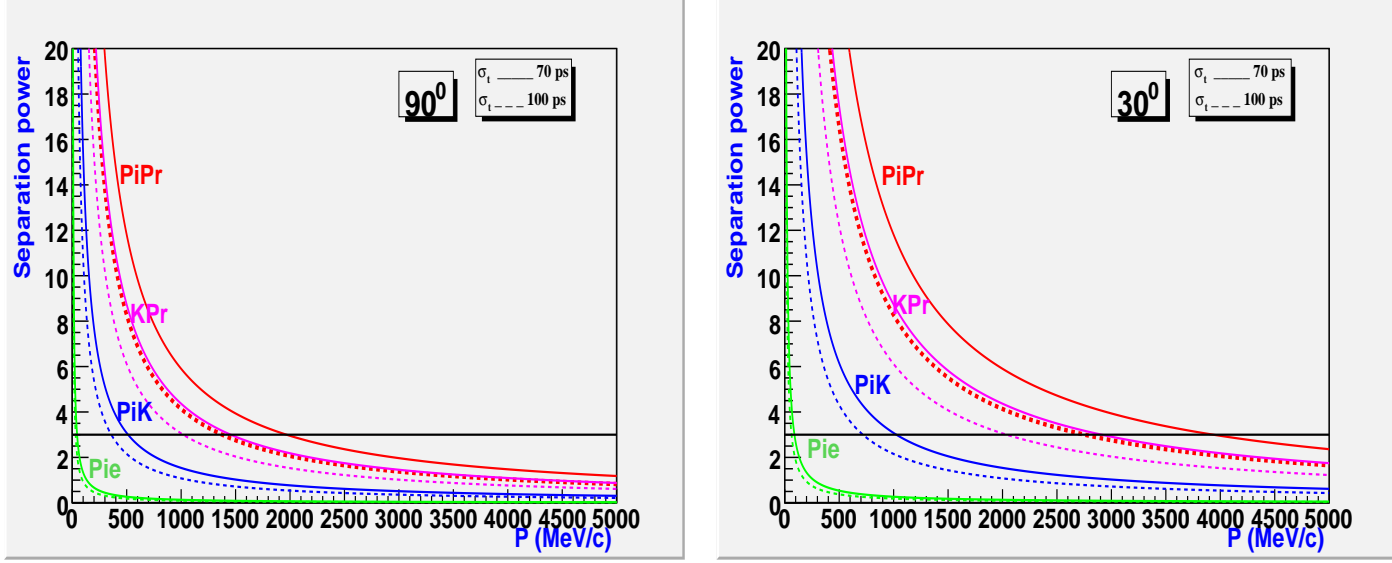


Figure 11: Separation as a function of momentum for polar angles $\Theta = 90^\circ$ and $\Theta = 30^\circ$.

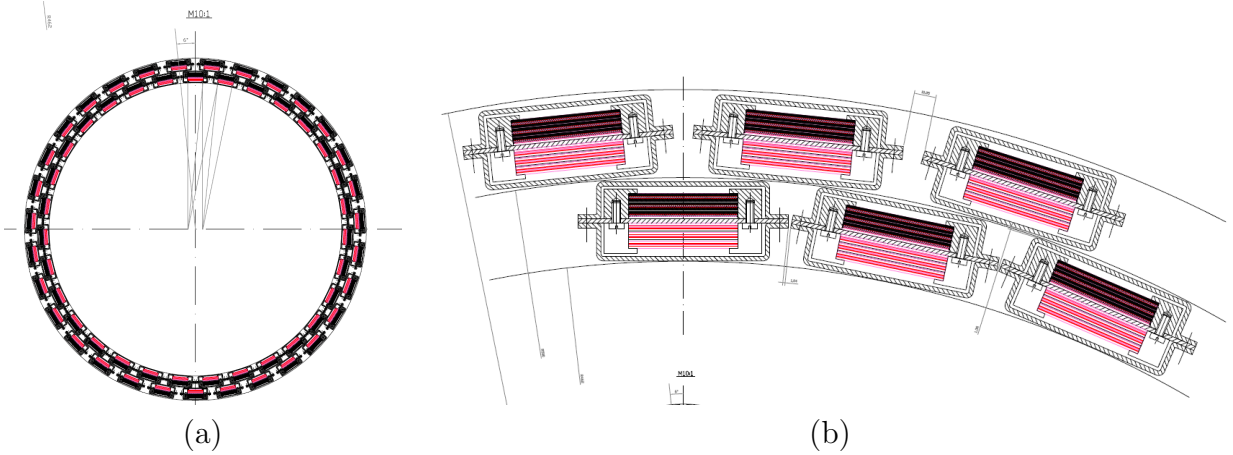


Figure 12: (a)View of DRPC TOF and (b)positioning of DRPC modules inside the barrel.

and QDC, or only TDC), as well as to provide low voltage for the FEE and high voltage for the chambers.

The part of the PCB containing the DRPC cells is placed inside an aluminum case. The rest part of the PCB is left outside the case and is intended to provide space for low voltage and high voltage connectors, filters, signal repeater for sending signals to the TDC (or the TDC itself) and a scheme for fast OR Region of Interest (RoI) trigger. The total sensitive region of the Barrel DRPC-TOF is about 5.6 m^2 , the total number of channels is 2232.

FEE and readout electronics Basing on the experience of the ALICE TOF project we suggest to use 8-channel NINO ASIC chips for FEE. These chips can be placed on the same PCB with the chambers between neighboring cells. For the readout an ALICE TOF end cap crate with commercial TDC (TRM module) and crate controller (DRM module) can be used [11]. In this variant, the Time-Over-Threshold (TOT) method of time-amplitude slewing correction may be implemented. Since the magnetic field in the PANDA environment is expected to be 4 times higher than that in ALICE, two such crates can be placed in the counting room.

DRPC cell design, rate capability and granularity. The DRPC is one of the RPC types developed during the R&D for the ALICE TOF. It was specifically designed to operate in a high-rate and high-occupancy environment. The DRPC may be described as a ceramic parallel-plate chamber with conductive electrodes, the anode of which possesses surface resistivity. This is done through depositing thin SiC layer on the anode by evaporation. Thereby, a quench circuit appears, formed by the SiC resistivity R and the chamber capacitance C [12].

Almost no change in the efficiency and time resolution of DRPC was observed under the rates of up to 5 kHz/cm² (Fig. 8b) whereas using conventional glass with the bulk resistivity of 10¹³ Ω cm limits the rate capability of RPC up to 1 kHz/cm². Since the rate in PANDA at $z \approx 0$ is expected to be more than 700 Hz/cm² in proton-antiproton collisions and even more in antiproton-Au collisions, the DRPC becomes a competitive alternative to the glass RPC.

To calculate the optimal TOF granularity, occupancy simulations were performed for the antiproton-p and antiproton-Au collisions by means of the UrQMD1.3 generator. The magnetic field was assumed to be equal to 2 T, the antiproton beam momentum was set at 15 GeV/c, no interaction with matter was taken into account.

The simulation proves that 80% of charged particles with the momentum of more than 0.15 GeV/c reach the TOF barrel. The main discovered PID problem is that particles with low p_T can hit TOF many times because of being caught by the magnetic field. Plots (a) and (b) in Fig. 13 show the number of hits per track in this case. The total occupancies in antiproton-proton and antiproton-Au collisions are presented in the plots (c) and (d) of Fig. 13. Despite small average numbers, the distributions have long tails and, for instance, in case of antiproton-Au collisions the occupancy can even reach 0.1 hits/dm². Therefore, to keep the total occupancy within 5%, the granularity has to be limited with 0.45 dm². We have decided to set the active size of the cell at 5×5 cm². More realistic simulation in the framework of the PandaRoot package will be done in the near future.

Material budget The radiation length of a module containing a 4-gap DRPC is estimated at 10-13% X_0 . The main part of it (8.5% X_0) comes from the ceramics. The exact value of radiation length will be defined after rigidity test of prototype with real PCB.

3.3.2 TOF scintillator barrel

The TOF scintillator barrel at Panda consist of 16 bars, each of these bars contains 6 scintillators slabs.

The scintillator material is BICRON 408. Due to the fact that the decay constant of this kind of scintillator doesn't allow a high light yield, the slab should have a thickness of 4 cm to obtain a time resolution of about 80 ps. Unfortunately such a thickness would create too many secondary electrons which could affect the other detectors, such as DIRC, and the calorimeter. The thickness of the TOF barrel assumed here has been 0.5 cm for simulations.

The TOF barrel has been implemented in the PandaRoot software, and a set of several particles, such as protons, pions and kaons, has been simulated isotropically inside the PANDA spectrometer. This simulation shows the ability to perform some particle identification, making use of the TOF system and providing some knowledge on the mass of the simulated particle. At the end the results can be compared to the ones obtained from the RPC TOF.

Fig. 14 shows the behavior of the particle velocity(beta) with the momentum. The beta parameter

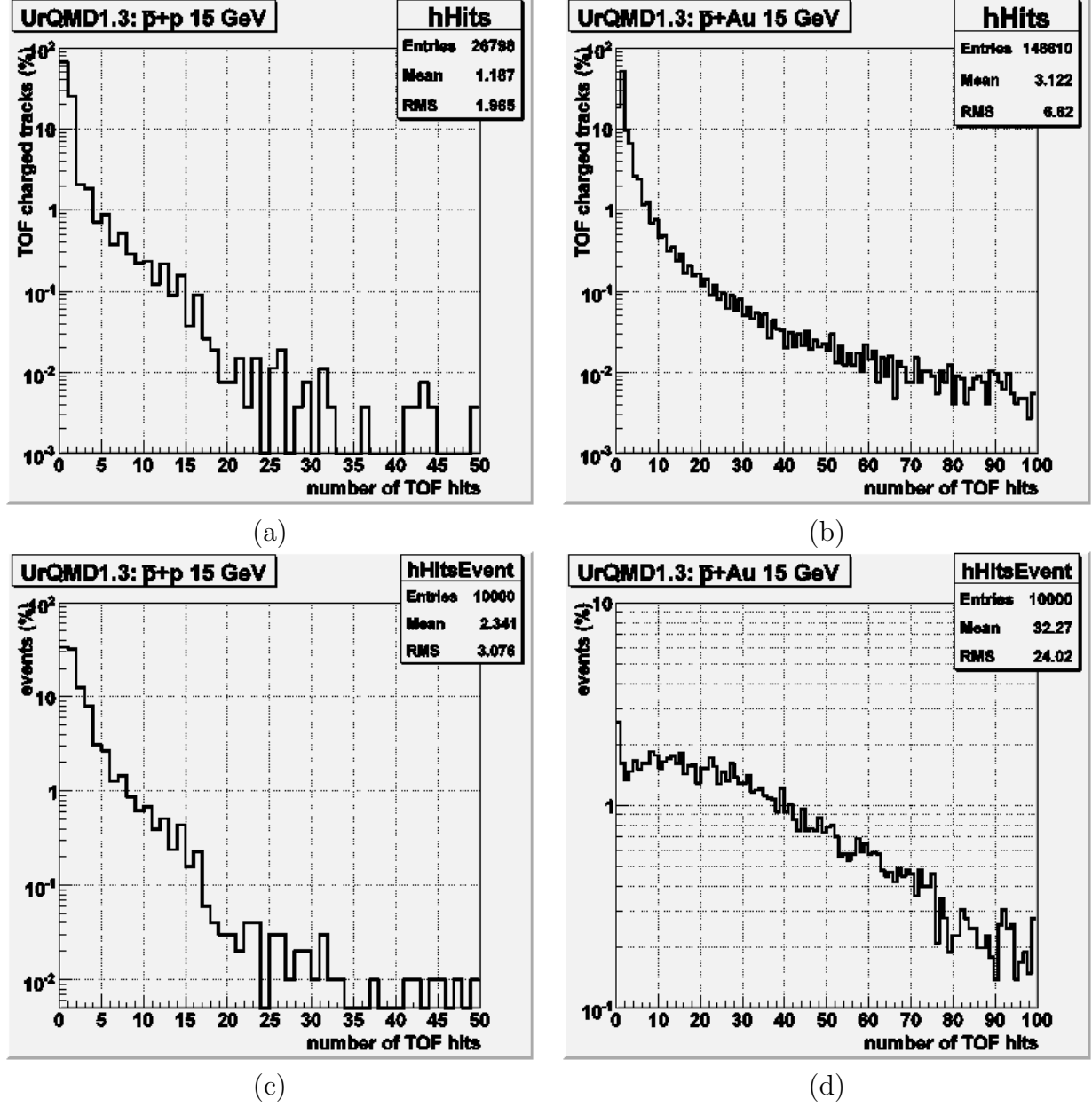


Figure 13: (a,b) Number of total TOF hits per track and (c,d) total number of TOF hits per event for antiproton-proton and antiproton-Au collisions.

is obtained by dividing the track length of the simulated particle by the time of flight measured by the TOF detector. In the figure the dark points represent pions, the blue kaons and the red ones protons. One can even observe that a good separation occurs for momenta lower than 1 GeV/c. In the figure below, the mass of the particles has been reconstructed by taking the track length, the momentum and the tof of the particle.

For this result, the tof hits were used in combination with the tpc hits, in order to perform a good track for the particle.

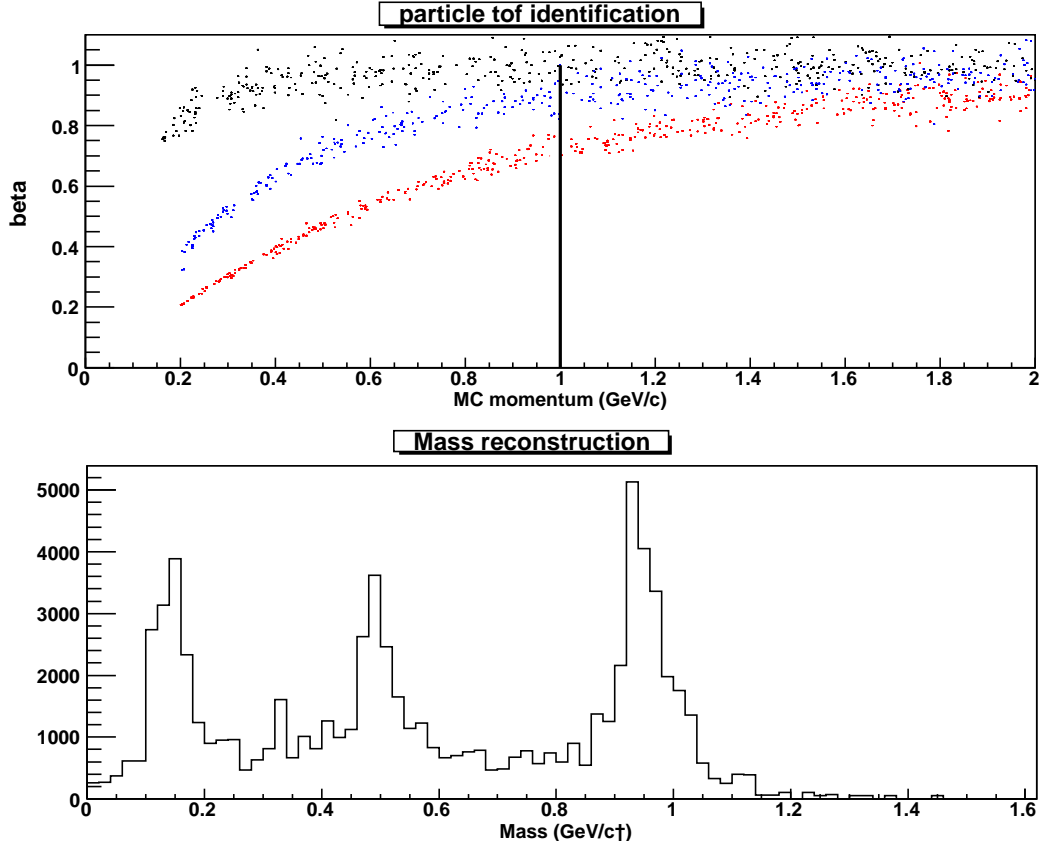


Figure 14: Particle identification using tof scintillator barrel. The upper plot shows the behavior of the beta and the momenta of the particle. The figure below represents the mass reconstruction for pion, proton and kaons

3.4 Barrel DIRC

The purpose of the Barrel DIRC (Detection of Internal Reflected Cherenkov photons) is to provide a particle identification. The mass of the particle can be obtained by combining the velocity information of the DIRC with momentum information from the tracking detectors. In addition the distinction between gammas and relativistic charged particles entering the EMC behind the DIRC is possible.

Basis for the calculations and simulations are the bar dimensions taken from the BaBar DIRC [13]. With the length adapted to the PANDA setup there are quartz bars of $17 \times 35 \times 2300 \text{ mm}^3$ and a distance of 480 mm to the target point. Thus the barrel DIRC covers the solid angle between 22 and 140 degrees. The lower momentum threshold for kaons to produce Cherenkov light is for an envisaged refractive index of $n=1.47$ as low as 460 MeV/c for single photon production. For larger photon numbers the momentum threshold increases. With 17mm (of thickness) of fused silica the DIRC bars present approximately 14% of a radiation length to normal incident particles. The support structure will add 3%.

This design is initially based on the BaBar DIRC (Fig. 15) but at PANDA further improvements of the performance are under development. The combination of the spatial image of the photons with their time of arrival gives access not only to their velocity but also to the wavelength of

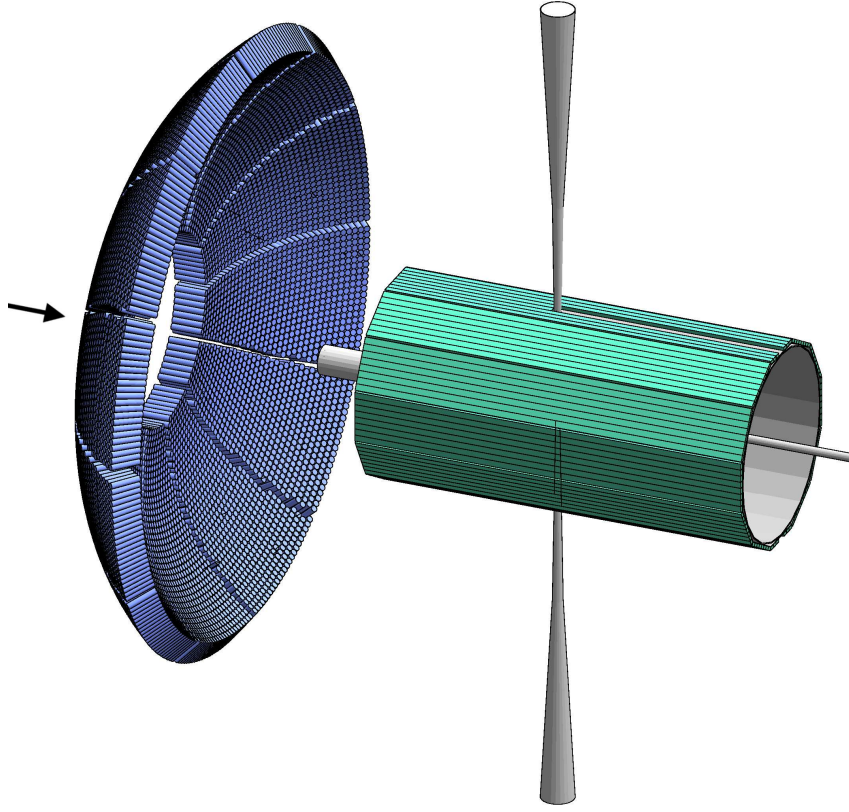


Figure 15: The PANDA barrel DIRC as a version of the BaBar-DIRC scaled down in size. The diameter of the barrel is 1 m.

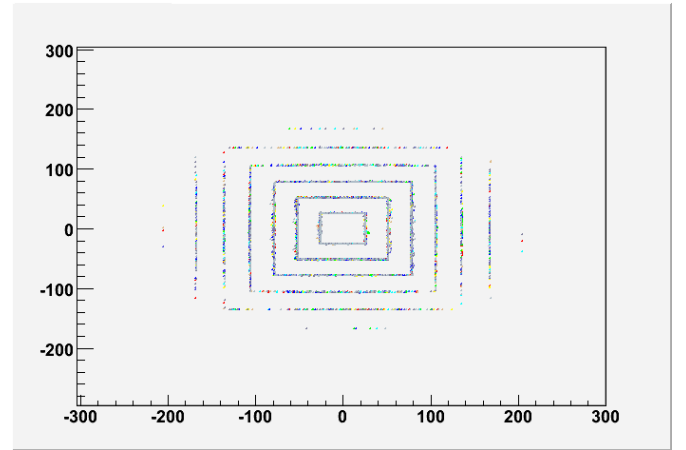
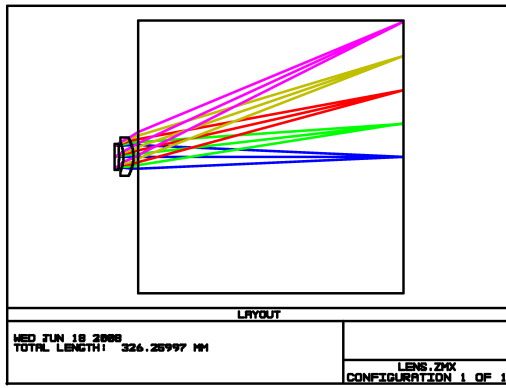
the photons. Thus dispersion correction at the lower and upper detection threshold becomes possible. Further on the reduction of the photon readout in size and number of photon detectors is envisaged. A lens or a set of lenses at the exit of the quartz bar focus the photons to a focal plane behind a readout volume of about 30 cm length. When this volume is filled with a medium with the same refractive index as the radiator material ($n_{medium}=n_{radiator}=1.5$) additional dispersion effects and other image distortions are avoided.

A major issue is the maintenance of the barrel DIRC. While in the Babar DIRC a removal of the radiator barrel and the photon detector was not foreseen, the PANDA barrel DIRC is to be planned removable. The disassembly is not planned as default operation during maintenance breaks. Rather the access to other detector parts and the replacement of broken DIRC items need a removal procedure. For that purpose a photon detector smaller in size is favorable. The segmentation of the radiator barrel and the optical joints between radiator and photon detector need also careful design. As shown below the design of the photon detector and its link to the radiator define the geometric dimensions of the latter.

Without having focussing elements each single PMT of the photon detector of the Babar-DIRC can measure photons coming from all of the radiator slabs. The only optical limitation is some space around the beam line which blocks photons from the other side. Introducing focussing elements like lenses or mirrors define a focal surface. A possible orientation of this focal surface

would be a flat plane perpendicular to the beam line. In this way each radiator slab focusses its photons on the same plane and each photon detector element can measure the photons from all radiator slabs. The design with different focal planes for different subsections (bar boxes) of the radiator barrel would cause split ring images caused by photons from one subsection entering the photon detector of another subsection. Blocking these photons reduces the photon detection probability by factors of two to three.

The design of a flat focal plane with a lens doublet consisting out of the glass NLAK33 and fused silica is shown in Fig. 16a. This lens combination was designed with the help of the ZEMAX optical program [14] focusses on a flat focal plane at a distance of 30 cm even for large angles of up to 40 degree. The results of the implementation in a ray tracer program (drcprop) within the PANDAROOT framework is shown in Fig. 16b.



(a) Design of a lens doublet with the optical software ZEMAX. The photon detector box is 300 mm in size

(b) Test pattern of photon images on the focal plane of a photon detector 300mm by 300mm in size. For a perfect image rectangular structures are expected to be observed.

Figure 16: Development of a photon readout with flat focal plane using a system of lenses.

The coordinates show the position on the photon detector in millimeter for photons coming from one of the slabs. In case of a perfect image one expects rectangular structures. The structures are for different opening angles which are from 5- 30 degree in 5 degree steps measured where one of the coordinates is zero. They allow to identify pin-cushion like or barrel like distortions. It is seen that here the photons are focussed up to angles of 30 degree. Large angles hit the side of the lens combination. There is still optimization for the design needed in order to keep the lens combination more compact.

3.5 Electromagnetic Calorimetry in the Target Spectrometer

The major purpose of the electromagnetic calorimeter (EMC) is to measure photons very precisely over a large energy range from approximately 10 MeV up to 15 GeV.

Lead-tungsten (PbWO_4) is chosen as crystal material due to its good energy resolution, fast response and high density. The crystals will be operated at -25°C to guarantee a high light yield and thus to achieve the required low energy threshold. Each of them will be 20 cm long, which is

equivalent to a radiation length of approximately $22 X_0$, and are tapered with a front size of $2.1 \times 2.1 \text{ cm}^2$.

The EMC is very compactly designed and is subdivided in three different parts, namely:

- the barrel calorimeter which consists of 11360 crystals and covers the Θ range between 22° and 140° ,
- the forward endcap calorimeter with 3600 crystals which is located within the Θ range between 5° and 22° , and
- the backward endcap consisting of 592 crystals which is placed in the Θ region $> 140^\circ$.

The various requirements for the EMC in the target spectrometer, its final design and resulting performance are extensively described in the EMC Technical Design Report [16].

3.5.1 PID Performance

Besides the detection of photons, the EMC is also the most powerful detector for the identification of electrons. The recognition of this particle species will play an essential role for most of the physics program of $\overline{\text{PANDA}}$. An accurate and clean measurement of the J/Ψ decay in e^+e^- is needed for many channels in the charmonium sector as well as for the study of the \bar{p} annihilation in nuclear matter like the reaction $\bar{p}A \rightarrow J/\psi X$. In addition the determination of electromagnetic form factors of the proton via $\bar{p}p \rightarrow e^+e^-$ requires a suppression of the main background channel $\bar{p}p \rightarrow \pi^+\pi^-$ in the order of 10^8 .

The performance of the electron identification with the EMC has already been investigated in detail utilizing the offline software which has been devised for the $\overline{\text{PANDA}}$ Physics Book benchmark studies. This will be briefly summarized in the following. More detailed documentations about these investigations can be found in the EMC Technical Design Report [16] and in the $\overline{\text{PANDA}}$ Physics Book [3].

In section 3.5.3 the possibility to identify K^+ at momenta below $0.8 \text{ GeV}/c$ via the EMC timing information will be briefly discussed.

3.5.2 Electron Identification

The footprints of deposited energy in the calorimeter differ distinctively for electrons, muons and hadrons. The most suitable property is the deposited energy in the calorimeter. While muons and hadrons in general lose only a certain fraction of their kinetic energy by ionization processes, electrons deposit their complete energy in an electromagnetic shower. The ratio of the measured energy deposit in the calorimeter to the reconstructed track momentum (E/p) will be approximately unity. Due to the fact that hadronic interactions can take place, hadrons can also have a higher E/p ratio than expected from ionization. Figure 17 shows the reconstructed E/p fraction for electrons and pions as a function of the momentum.

Furthermore, the shower shape of a cluster is helpful to distinguish between electrons, muons and hadrons. The largest fraction of an electromagnetic shower originating from an electron is contained in just a few crystals. On the other hand a hadronic shower with a similar energy

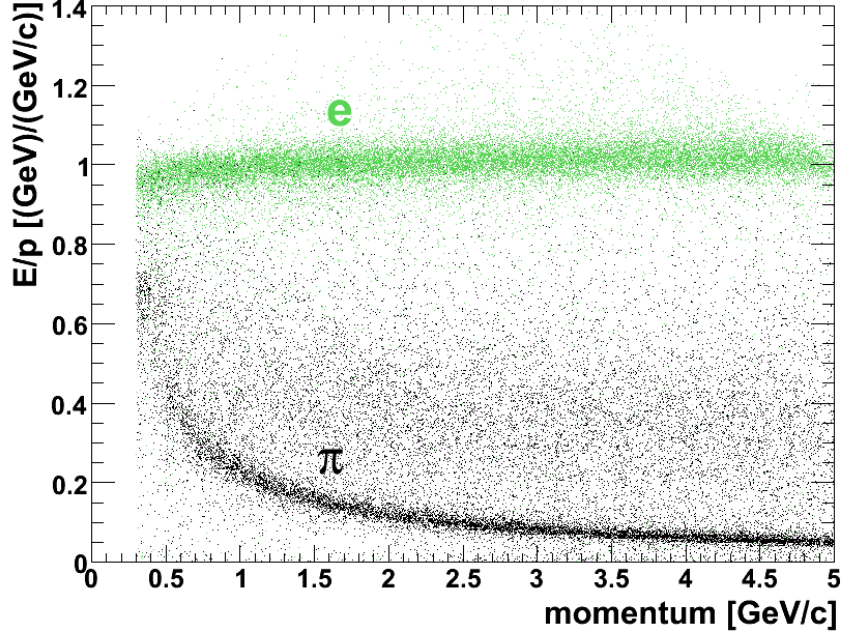


Figure 17: E/p versus track momentum for electrons (green) and pions (black) in the momentum range between 0.3 GeV/c and 5 GeV/c.

deposit is less concentrated. These differences are reflected in the shower shape of the cluster. The most important properties are:

- E_1/E_9 which is the ratio of the energy deposited in the central crystal and in the 3×3 crystal array containing the central module and the first innermost ring. Also the ratio between E_9 and the energy deposit in the 5×5 crystal array E_{25} is useful for electron identification.
- The lateral moment of the cluster defined by

$$mom_{LAT} = \frac{\sum_{i=3}^n E_i r_i^2}{(\sum_{i=3}^n E_i r_i^2 + E_1 r_0^2 + E_2 r_0^2)} \quad (4)$$

with

- n : number of modules associated to the shower
- E_i : deposited energy in the i TH crystal with $E_1 \geq E_2 \geq \dots \geq E_n$
- r_i : lateral distance between the central and the i TH crystal
- r_0 : the average distance between two crystals.
- A set of Zernike moments which describe the energy distribution within a cluster by radial and angular dependent polynomials.

Since a lot of partially correlated EMC properties are suitable for electron identification, a Multilayer Perceptron (MLP) has been applied to obtain the optimal performance. The advantage of

a neural network is that it can provide a correlation between a set of input variables and one or several output variables without any knowledge of how the output formally depends on the input. 10 input variables in total have been used for the training of the MLP, namely E/p , p , the polar angle θ of the cluster, and 7 shower shape parameters (E_1/E_9 , E_9/E_{25} , the lateral moment of the shower and 4 Zernike moments).

This trained network has been tested with a data set of single particles in the momentum range between 300 MeV/c and 5 GeV/c. The obtained performance is illustrated in Figure 18, which shows the electron efficiency and contamination rate as a function of momentum by requiring an electron likelihood fraction of more than 95%. For momenta above 1 GeV/c one can see that the electron efficiency is greater than 98% while the contamination by other particles is substantially less than 1%.

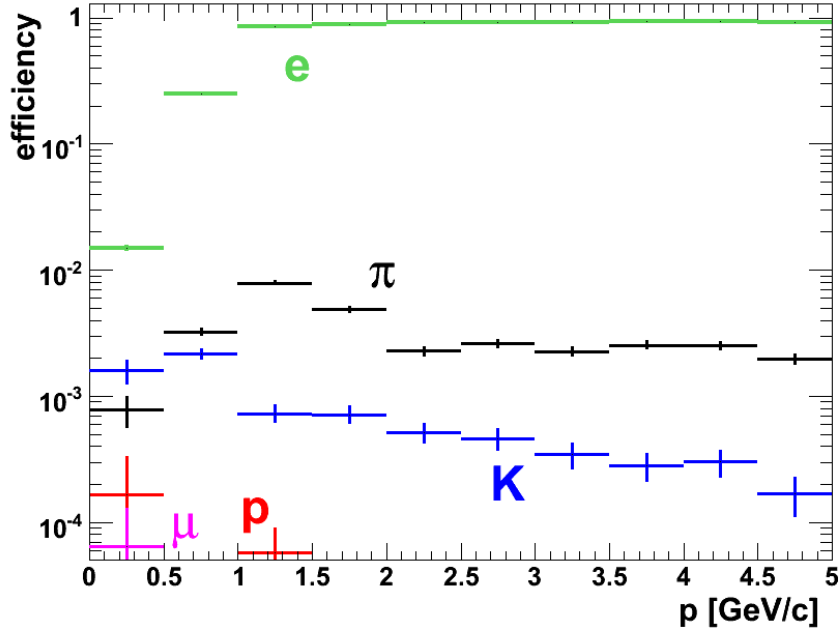


Figure 18: The electron efficiency and contamination rate for muons, pions, kaons and protons in different momentum ranges by using the EMC information.

3.5.3 Afterpulse K^+ Identification

The EMC crystals of 20 cm length have enough stopping power for $p=700\text{MeV}/c$ (or $T=360\text{MeV}$) kaons. Stopped positive kaons remain in the crystal lattice until they decay, with 63% branching ratio into muon plus neutrino. With 110 MeV kinetic energy the muons have enough energy to reach and deposit energy in one or two adjacent crystals. There is also the hadronic decay branch with 21% into π^+ and π^0 .

With a mean kaon lifetime of $\tau=12\text{ns}$ a delayed time tag from crystals adjacent to the kaon stopping crystal is a clean kaon identification, if the EMC timing is at least a few ns.

This positive kaon tagging works well with the Crystal Ball (CB), currently installed and running

at MAMI in Mainz[17], with NaI crystals of about the same stopping power as foreseen for the $\overline{\text{PANDA}}$ EMC, wider crystals and a 2 ns time resolution. Typically, the afterpulse time window opens at 8 ns after the prompt pulse. At MAMI, about 20% of the stopped positive kaons can be tagged with such an afterpulse.

In $\overline{\text{PANDA}}$, 10-30% of $p=700\text{MeV}/c$ kaons decay before they can be stopped in the EMC, depending on the flight path length. The finer granularity for the $\overline{\text{PANDA}}$ EMC (as compared to Crystal Ball) will allow a moderate increase in the fraction of afterpulse tagged K^+ . Crucially this method depends on the availability of timing information in the ns range.

This method allows some kaon identification capability in the momentum range which lies below the momentum range of the DIRC detectors with fused silica radiators foreseen for $\overline{\text{PANDA}}$.

3.6 Endcap Cherenkov

Two DIRC design options exist for the endcap part of the target spectrometer section. These differ in the photon readout design but both use an amorphous fused silica radiator disc. The endcap detector position covers forward angles of up to $\vartheta = 22^\circ$ excluding an inner rectangular area of $\vartheta_x = 10^\circ$ horizontal and $\vartheta_y = 5^\circ$ vertical half-angles. Simulations using the DPM generator [15] give an average charged particle multiplicity per $\bar{p}p$ interaction of 1.0 ± 0.8 (at $2\text{ GeV}/c$) to 2.3 ± 1.8 (at $15\text{ GeV}/c$) emitted from the target vertex into this acceptance.

In such a one-dimensional² DIRC type, a photon is transported to the edge of a circular disc while preserving the angle information. Avoiding too much light scattering loss at the surface reflections requires locally (in the order of millimeters) a surface roughness not exceeding several nanometers RMS.

The lower velocity threshold, which is common to both designs, depends on the onset of total internal reflection for a part of the photons emitted in the Cherenkov cone.

There are several boundary conditions for the disc thickness. Radiation length considerations as the detector is upstream of the endcap EMC call for a thin disc. The focussing design is workable with 10mm thickness ($X_0=126\text{mm}$). Regarding the mechanical stability and handling during polishing, current company feedback recommends 20mm minimum thickness. The resulting thickness of the radiator disc has to be a compromise.

3.6.1 Focussing Disc DIRC

In the Focussing Light guide Dispersion-Correcting design (Figures 19 and 20), when a photon arrives at the edge of the circular or polygonal disc, it enters into one of about hundred optical elements on the rim. Here the two-fold angular ambiguity (up-down) is lifted, the chromatic dispersion corrected and the photon focused onto a readout plane. While the optical element entered determines the ϕ coordinate, measuring the position in the dispersive direction on the focal plane of the focussing light guide yields the θ coordinate.

Lithium fluoride (LiF) is UV transparent and has particularly low dispersion. Proton beam irradiation of a test sample shows that radiation-produced color centers are confined to sufficiently

²Light is only reflected on surfaces of one spatial orientation, here the two disc surfaces both normal to the z axis.

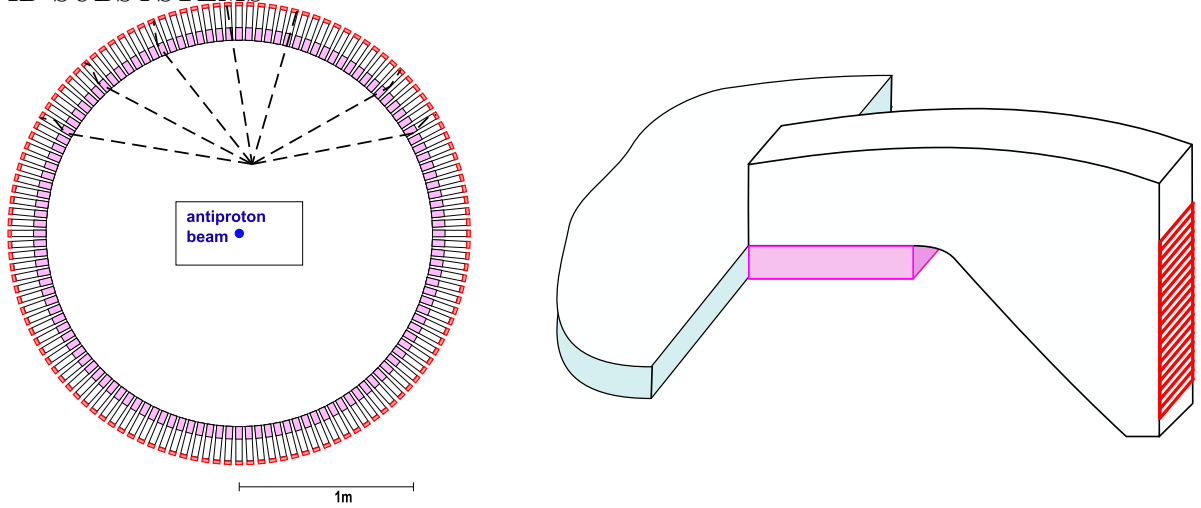


Figure 19: Polygonal disc with focussing light guides attached to the rim used as optical readout components.

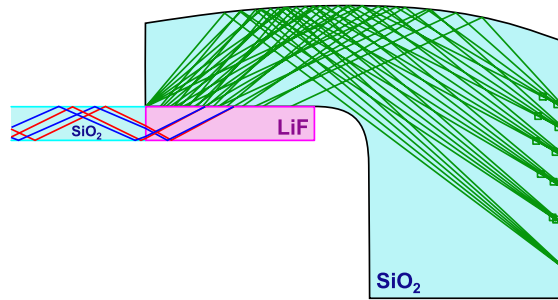


Figure 20: Light guide side view shown with a set of rays used for optimising the light guide curvature. Reflections at the parallel front and back surfaces keep the light inside but do not affect the focussing properties.

598 small wavelength ranges, and are only partially absorbing at the expected $\bar{\text{PANDA}}$ lifetime dose.
 599 Hence we believe we can use LiF as a prism element (see Fig. 20) to correct the Cherenkov
 600 radiation dispersion. The two boundary surfaces, with the radiator disc and the subsequent light
 601 guide, make the chromatic dispersion correction angle-independent to first order.

602 As with the radiator, the light impinging on the inside of the light guide's curved surface undergoes
 603 total internal reflection, hence no mirror coating is needed. This reflection makes the focussing
 604 also independent of the wavelength.

605 With the light staying within the dense optical material of the light guide, most of the incoming
 606 light phase space from the disc is mapped onto the focal plane with its one-coordinate readout.
 607 The focussing surface with cylindrical shape of varying curvature has been optimised to give an
 608 overall minimum for the focus spot sizes of the different angles on the focal plane, individual
 609 standard deviations being well below 1 mm for the instrumented area.

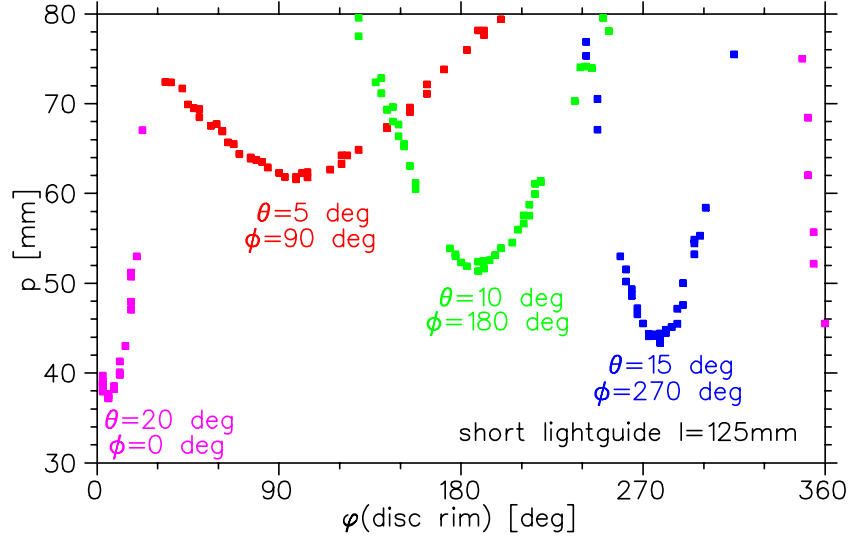


Figure 21: Simulated photon hit pattern for four particles emitted at different angles θ and ϕ from the target vertex.

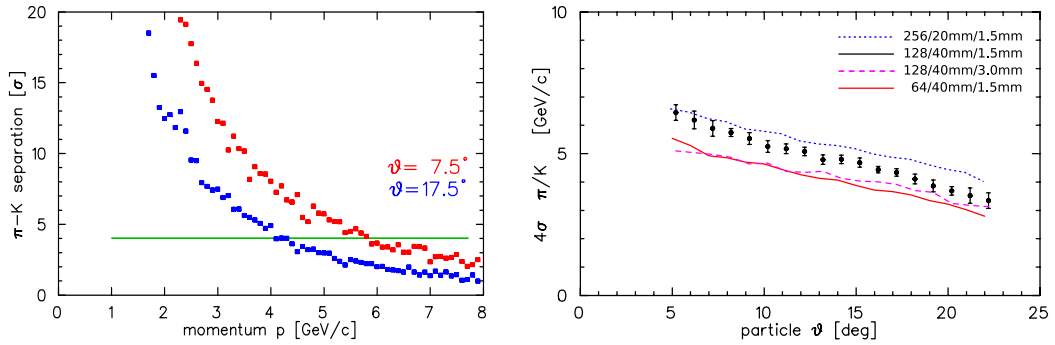


Figure 22: Simulation-derived pion-kaon separation power for a focussing lightguide design with a 15 mm thick amorphous fused silica disc and 0.4 eV photon detection efficiency. On the left the momentum dependence for two selected emission angles at the target vertex, on the right 4σ values as a function of the angle, black data points are the reference design.

For an Endcap DIRC detector with 128 lightguides and 4096 detector pixels that fits inside the target spectrometer return yoke, Figure 22 shows the angle-dependent upper momentum limit being about 4–6 GeV/c for 4σ pion-kaon separation within the acceptance $\vartheta=5^\circ\text{--}22^\circ$.

Typically all of the 40 detected photons per particle arrive within a 4 ns time window.

Each lightguide can individually be assigned its own 0.4 ns acceptance window. For the pixel size used in this simulation they are contained inside a 40 pixel·ns volume, which at 4000 detector pixels amounts to 10 ps detector occupancy time per particle signature.

The detected photon rate (source: presentation KF 2007-03-27 Genova, $2E7$ interactions; scaled to 4000 pixels) is $3E7\text{ s}^{-1}$ per PMT and $1E6\text{ s}^{-1}$ per detector pixel.

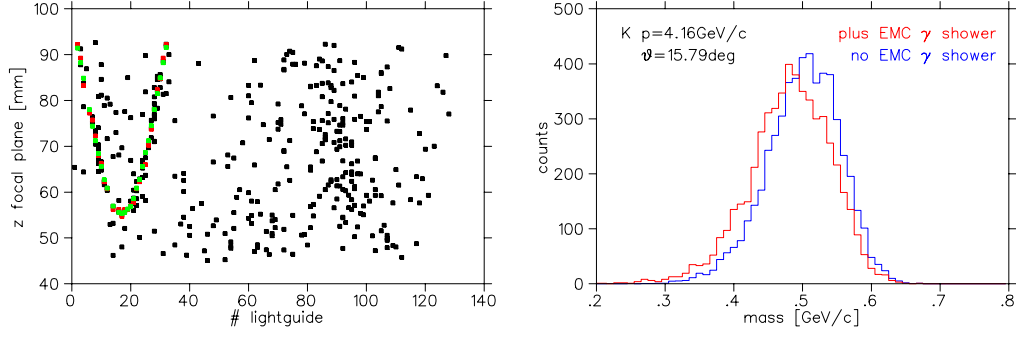


Figure 23: Left: Measured photon distribution from a γ Barrel EMC shower leaking out of the EMC edge towards the Endcap. Photons from one kaon of $4.16\text{GeV}/c$ are added, and the kaon velocity is derived from candidate kaon photons. Right: Analysed mass distributions for kaon with and without shower. The road for kaon photon acceptance is derived from simulations, and within some simulation simplifications the bounds are set such to include (almost) 100 percent of the photons. The systematic offset with the onset of background is thought to be caused by the true kaon photon centre of gravity being off the middle of the road interval, probably explained by the coma aberration of the curved lightguide focussing (an improved interval algorithm should help). At this level of background there is a small increase in the width of the reconstructed kaon mass distribution.

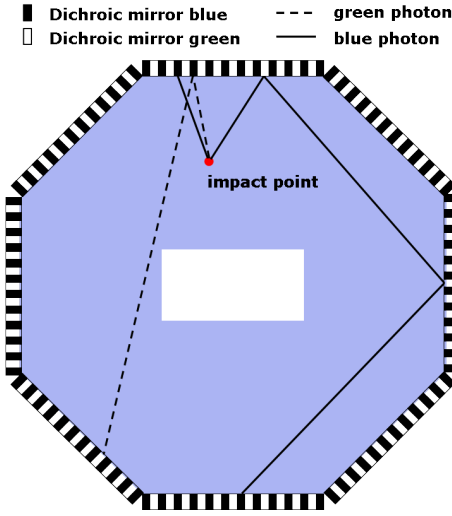


Figure 24: Sketch of the flight-path in the ToP Disc

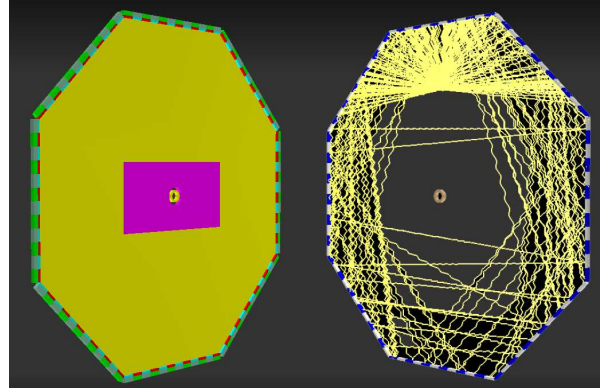


Figure 25: Current scheme of TOP DIRC, 960 photon detectors mounted at rims of octagon disc, located at $Z=180\text{cm}$ in the PANDA coordinate system(left side). On the right side the disc was hit by $4\text{ GeV}/c$ pion at 15° , the yellow lines shows the path of generated Cherenkov photons. Some of them hit dichroic mirrors, are reflected and travel longer.

619 3.6.2 Time of Propagation Disc DIRC

620 In the Multi-Chromatic Time-of-Propagation design ([18]) small detectors measure the arrival
 621 time of photons on the disc rim, requiring $\sigma_t=30\text{--}50\text{ ps}$ single photon time resolution.

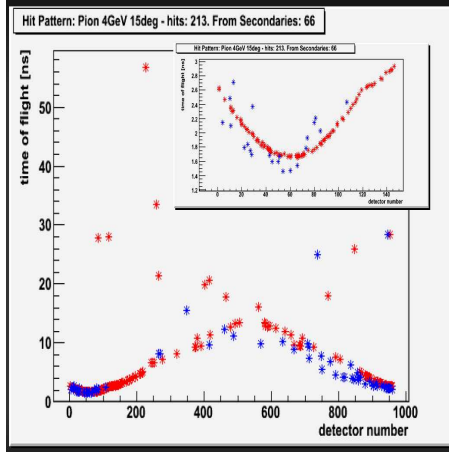


Figure 26: Hit pattern of photons in two-dimensional(ϕ, t) space. The Cherenkov photons coming from primary particle are marked red and from secondary particles, marked blue.

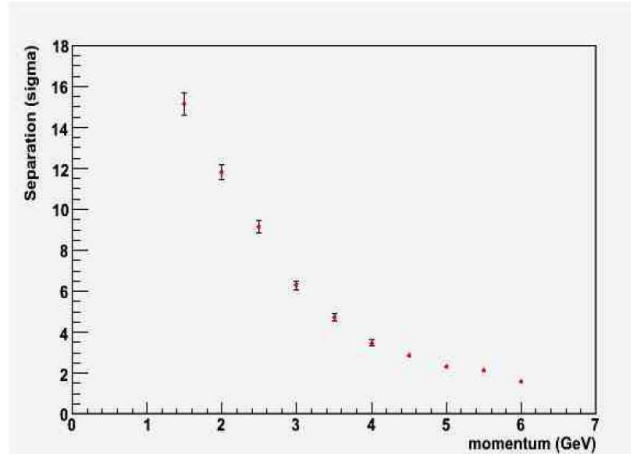


Figure 27: Separation power between kaons and pions from Slope fitting.

For any given wavelength, the disc edge is effectively covered alternately with mirrors and detectors. Only due to the resulting different light path-lengths one can determine accurately enough the start reference time, i.e. the time when the initial charged particle enters the radiator, as the stored anti proton beam in the HESR has no suitable time structure to be used as an external time start.

As some of the light is reflected several times before hitting a detector, the longer path lengths allow a better relative time resolution.

The use of dichroic mirrors as color filters allows the detection of multiple wavelength bands within the same radiator (the current design suggesting two bands) resulting in higher photon statistics. The narrow wavelength bands minimize the dispersion effects, and the quantum efficiency curve of the photo cathode material could be optimized for each wavelength band individually.

To verify the Principle of the ToP Disc the geometry of the disc was implemented into PandaRoot and multiple sets of Monte-Carlo data were generated with subsequent reconstruction of the generated particle types. The fig.25 shows the ToP Disc implementation into PandaRoot (left) and generated photons from an incident pion and their path from the impact point on disc(right).

The reconstruction of particle types using different methods, like pattern fitting or slope fitting in two-dimensions (detector number and time of propagation(fig.26) in first case, the calculated arrival time of Cherenkov photons and MC time from GEANT in second case) yields acceptable separation and low percentage of misidentification. See fig.27 for example in case of kaons and pions.

Already first simulations indicate the possible hurdles in particle identifications in the ToP Disc DIRC. One of them is the smearing of the patterns from secondary particles, marked as blue points in figure26. The possible effect from this is depicted in the next figures, where we present the misidentification between kaons and pions without inclusion of secondaries (see figure28a) and with inclusion of them (see figure28b).

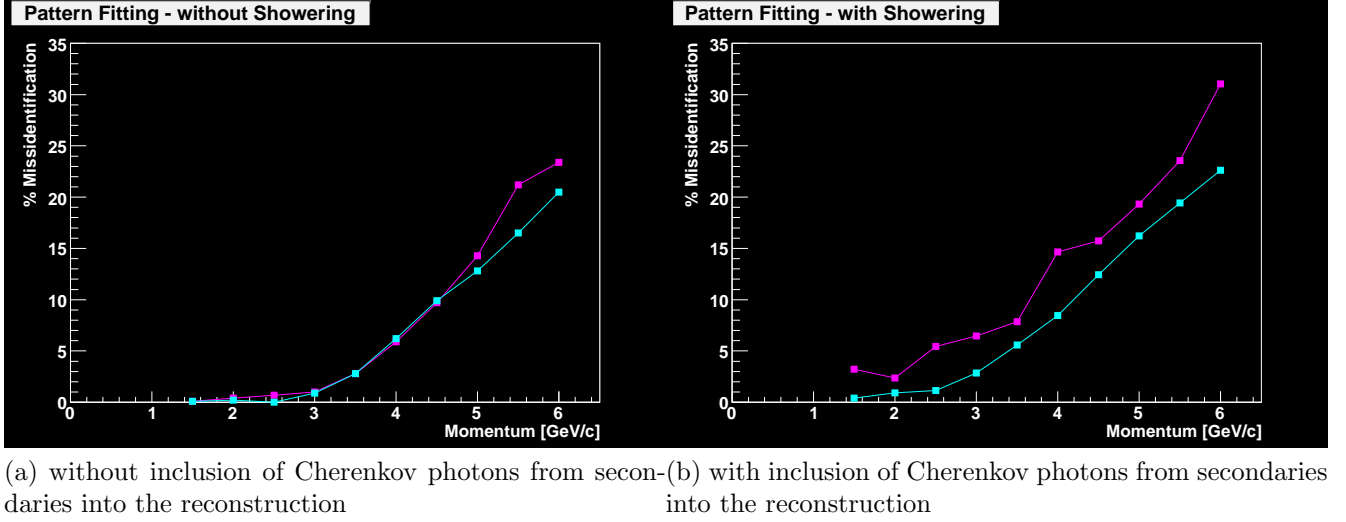


Figure 28: Misidentification between kaons and pions

To show that electrons can imitate Cherenkov radiation like pions we have performed MC simulation of pions and electrons passing through 2cm thick quartz glass. The resulting spectra are depicted in the figure29. As we can see $\approx 60\%$ of electrons pass the glass without showering(red), like most of the pions(magenta). In both cases we have secondaries, significantly more from electrons(blue) than from pions(green). This is the more difficult situation than in case of pions, but for the test, its better to have checks done in difficult case than in simplified ones.

3.6.3 Proximity RICH

As alternative approaches Proximity Imaging Solutions were considered.

- Liquid radiator proximity RICH using CsI GEMs: Proximity focusing RICH detectors use the most simple imaging geometry. Their resolution depends on the optical quality and crucially on the ratio of radiator thickness to stand-off distance, the distance between the creation and detection of the photon. Using liquid or solid radiators yielding enough Cherenkov photons, the radiator can be kept rather slim, which in turn only requires moderate stand-off distances on the order of 100 mm. The ALICE HMPID detector is build in this fashion using a C6F14 liquid radiator and CsI-photon cathodes in an MWPC. This requires a UV optic. It is proposed to use the same radiator technique and combine the third tracking station with a CsI coated GEM photon detector. The detector will be thicker along the beam direction than the DIRC detector previously described, but can be essentially moved to any position along the beam axis. The estimated performance and the ALICE/STAR test results show a significant decrease in performance compared to the DIRC solutions.
- Solid radiator proximity RICH using CsI GEMs: One of the main drawbacks of using the ALICE design is the use of C6F14. This radiator is rather sensitive to impurities and radiation damage requiring a purification system. Using a fused silica disc with a properly machined surface as radiator circumvents the problem while keeping the geometrical advantages of the design. Initial studies show a further reduction of performance mainly due to strong dispersive effects in the UV region.

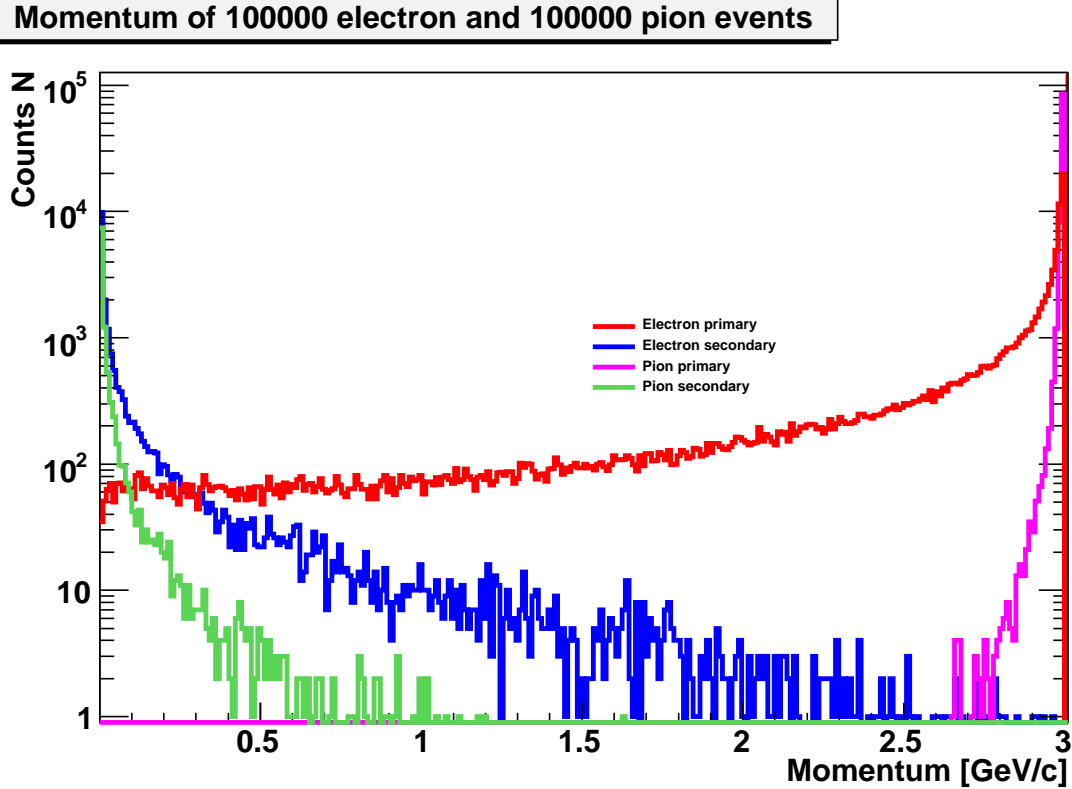


Figure 29: Energy spectra of primary and secondary charged particles inside 2cm thick glass after hitting it with electrons(pions) with 3.0 GeV energy. Unfortunately the energy of secondary particles are high enough to create Cherenkov photons and as they doesn't have the same direction as the primary particle, the photons created by them smear the coordinate or the timing pattern of the primary particle, hence, making reconstruction difficult.

- Aerogel proximity RICH using PMTs: The Belle endcap Cherenkov threshold counter will be replaced by a proximity imaging RICH counter using an Aerogel radiator and conventional BiAlkali based multi-pixel PMTs as photon detectors. Using a so-called focusing radiator scheme, prototypes show excellent performances. The main technological challenge for this detector is to realise a photon detection matrix in a strong magnetic field. Recent developments in the field of proximity focusing HAPDs seem to make such a detector realistic.

3.7 Muon Counter

The main purpose of the PANDA muon system is to achieve the highest efficiency in identification of muons in the medium-to-high energy range. Muons are present in the final state of many annihilation channels. Among them the physics program is mostly concentrated on dimuon production from Drell Yan at the maximum HESR momentum of 14.5 GeV/c or J/ψ formation and decay in nuclear matter at 4.1 GeV/c momentum. In addition the study of rare decay of charmed particles could require a single muon identification. The most severe PID requirements to the muon system are set by the DY dimuon production, that has been selected as benchmark channel. Looser identification requirements are set by the J/ψ production channels, because of

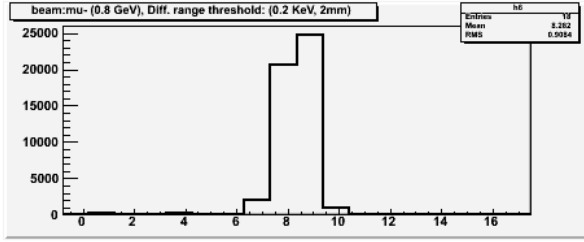


Figure 30: Range measured as number of crossed planes for a muon with 0.8 GeV energy.

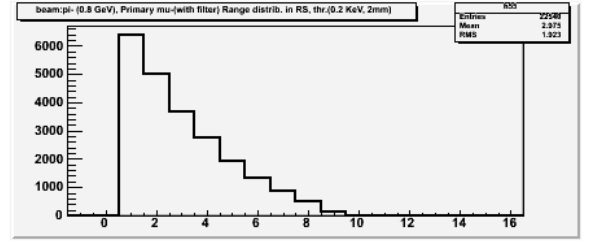


Figure 31: Range measured as number of crossed planes for a pion with 0.8 GeV energy.

the strong kinematics constraint on the dimuon mass.

In general the interesting processes having muons in the final state have small cross sections compared with the background, e.g. the DY channel features a very low cross section ($\approx 1nb$) and an unfavorable signal-to-noise ratio of $\approx 10^{-6}$. As a consequence the muon system must provide the maximum acceptance and efficiency. In the dimuon channels the simultaneous identification of a slow and of a fast muon is needed, with a strong correlation angle-momentum.

Muon counters are foreseen both in the Target barrel part and endcap. In the Forward spectrometer the muon counters and filters will act as hadronic calorimeter. The azimuthal angle covered by the muon system ranges from 0° to 120° with a 2π polar angle coverage. With respect to the Letter of Intent the muon system has retained the original idea to use the solenoid yoke as muon filter. However the concept design has changed following the results of a preliminary acceptance study and the iron segmentation has been considered for the system optimization.

The momentum range of the DY muons reaching the barrel extends up to few GeV/c. The lower end of the range is fixed by the energy losses and the magnetic bending in the inner detectors (500 MeV/c).

The DY muons crossing the forward endcap show an energy range going from 1 to 3 GeV, with an average energy loss of 250 MeV before to enter the muon counters. The energy of the muons travelling through the Forward spectrometer can be greater than 10 GeV.

As a consequence slow muons, mainly produced in transverse direction cannot reach the muon system and must be identified by the inner detector. Medium and high energy muons are identified by the muon system only if they are positively detected by the muon detectors and properly match a charged primary track detected by the central tracker. The muon detector output that can be considered for identification purposes is the hit multiplicity in a selected region and, for isolated tracks, a direction and, where possible, a momentum measurement. Range measurement was also suggested as an effective tool for μ/π separation and the arrangement presently under simulation is conceived for this purpose, see fig. 30 and fig. 31.

The following plots show the behavior of some parameters useful for the muon identification.

The background coming from primary hadrons (mostly pions) could be rejected by the evaluation of the number of planes in the muon system crossed by the charged particle (see fig. for muon and pion of equal energy).

The contamination coming from secondary muons produced by the pion decay could be reduced by considering the angular correlation between the track extrapolated from the vertex and the track segment measured by the muon detectors. In this case (see fig. 32) the measurement of the track momentum by the muon detectors could help.

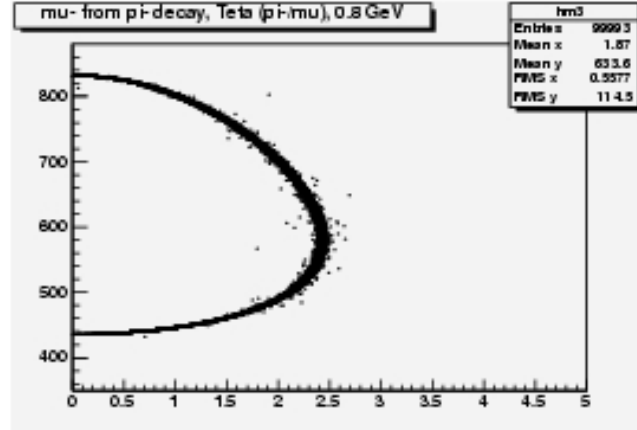


Figure 32: Muon from decaying pion with 0.8 GeV energy: energy vs decay angle in the Lab system.

here(relevant plots

3.7.1 Muon system overview

The parameters considered in the choice of the muon detectors are the spatial and time resolution, to allow independent reconstruction of the track segment direction, the simplicity and flexibility of the design, since the area to be covered is large and divided in different shapes, the robustness the reliability, also in terms of ageing and finally the cost. the Muon Drift Tubes (MDT) have been proven to be a mature and widely used technique that join a very high detection efficiency ($\approx 95\%$) to a great simplicity of construction and operation. Following the proposal of the JINR-Dubna group an eight-cell module of MDT is constituted by a metallic cathode extruded with a comb-like profile and covered by a stainless steel cover. The signal wires pitch is 10 mm, the thickness of the profile is ≥ 0.45 mm and gives the main contribution to the inefficiency of the counter.

here the MDT cross section and the table of the performances

The MDT are one-coordinate detectors and at least two layers must be installed to get a track space point. An R&D project is going on at JINR Laboratories aiming to use MDT as two-coordinate detector. For this purpose the stainless steel cover should be removed and substituted by a plastic support for strips or pads. In this case the second coordinate is obtained by reading out the induced signal.

The MDT are operated in proportional mode. Both the Yes/No readout or the wires and drift time measurement are considered for the PANDA operation. The best spatial resolution is obtained in drift mode operation, corresponding to 0.5-0.8 mm r.m.s.

The detector coverage presently considered corresponds to a full coverage of the Target Spectrometer in the transverse direction with respect to the beam axis (Barrel) and in the forward direction (Forward Endcap), using the yoke of the solenoid as a muon filter. One of the eight parts of the barrel will be only partially covered by muon counters to allow the insertion and the operation of the target and its services. In the Forward Spectrometer (angular coverage from $5^\circ - 10^\circ$ to 0° the hadron calorimeter could be combined with muon counters forming a range system, too 3.10.2.

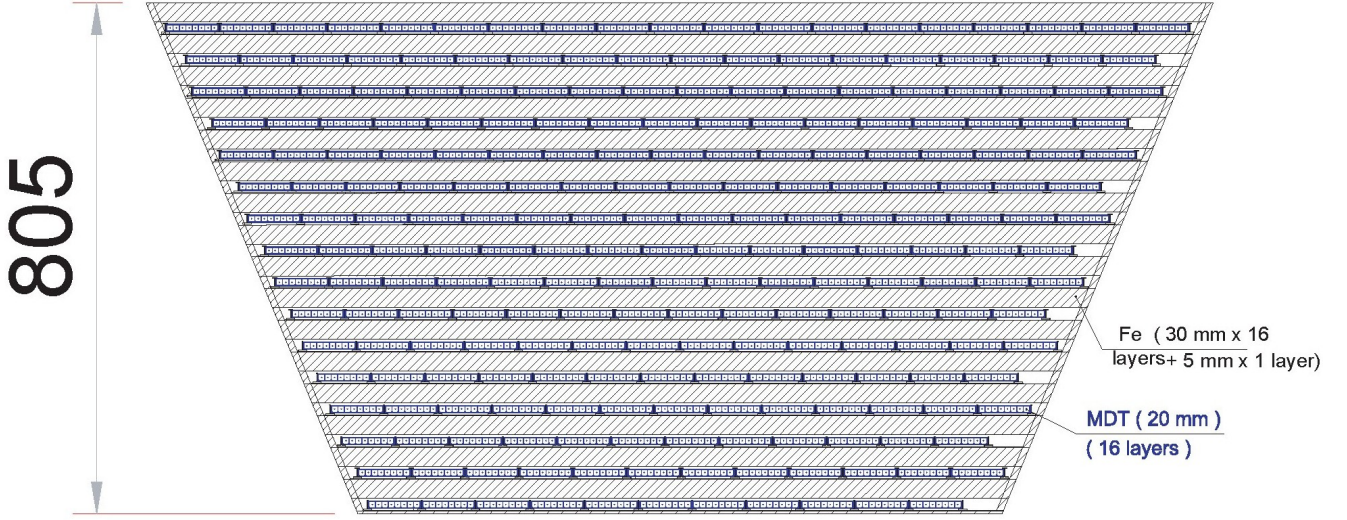


Figure 33: *Cross section of the Muon range system in the Target Spectrometer.*

3.8 Forward RICH

The forward boost of the reaction products, being a characteristic feature of fixed-target experiments, calls for good particle detection and identification at small scattering angles.

The Forward RICH is the solution proposed to perform PID for the ejectiles emitted at laboratory angles $\vartheta_X < 10^\circ$ and $\vartheta_Y < 5^\circ$. Physics, geometrical limitations and location of this detector impose the following requirements on the design of this detector:

- wide momentum range for hadron identification (up to $\sim 10 \text{ GeV}/c$),
- minimum material budget (in order not to deteriorate momentum and energy resolution of the downstream detectors),
- radiation hardness.

The first feature requires a careful choice of radiators. The current design proposes to build the Forward RICH as a dual radiator Cherenkov detector, with aerogel (PID for lower momenta) and perfluorhexane (PID for higher momenta). This option is used in other experiments, *e.g.* HERMES [19] and LHCb [25]. HERMES RICH design ranges of particle separation based on the signal from each of the radiators are shown in fig. 34. The limits were calculated assuming realistic photon resolution of $\sigma(\vartheta) = 7 \text{ mrad}$, and the number of photons produced in the gas and the aerogel as 12 and 10, respectively. In the calculation of upper momentum limit of the separation, the demanded number of standard deviations between the two distributions $n_\sigma = 4.652$.

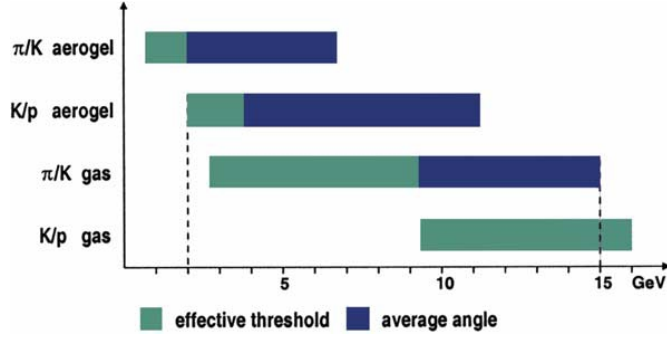


Figure 34: Momentum ranges for hadron separation in aerogel and perfluorhexane (C_4F_{10}). Between the dashed lines, the hadrons can be separated (figure from [19]). Light parts of the bars indicate the momentum regions, where the detector acts as a threshold Cherenkov.

The main disadvantage of this choice of radiators is a relatively high kaon threshold at 2.0 GeV/c. However, at lower momenta identification of ejectiles can be performed with the use of a TOF wall, as discussed in sec. 3.9.

The need to reduce the material budget to the necessary minimum favors mirror imaging. Using carbon-fibre based mirrors allows to move the photon detector outside of the acceptance of the Forward Spectrometer and thus reduce the overall detector thickness to ca. 8 – 11% X_0 . The Forward RICH of \bar{P} ANDA will be much larger than the HERMES RICH and the space available for it is very limited. This requires a careful study of the optics. One of the currently considered options includes four spherical mirrors and four detection planes, the other exploits the LHCb design (see fig. 35).

The last requirement, radiation hardness, can be fulfilled choosing HPDs or MA-PMTs for photon detection. With the appropriate shielding, they have capability to operate in the fringe field of the dipole magnet. The granularity of the photon detectors can only be adjusted when the design of the RICH geometry is finalised.

3.9 Forward ToF

Typical momentum spectra of the charged hadrons produced within the acceptance of the forward spectrometer FS (± 10 deg. in horizontal plane and ± 5 deg. in vertical plane) for primary beam momentum of 15 GeV/c are shown in Fig.36. The spectra are calculated in the Pandaroot framework using the Dual Parton Model (DPM) Monte Carlo generator. The hadrons with momentum below 4-5 GeV/c are assumed to be identified with the help of time of flight (TOF) technique. Identification of hadrons with higher momenta requires a forward RICH. This is in particular important for identification of anti-hyperons. For example, practically all anti-lambda hyperons produced in the $\bar{p}p \rightarrow \bar{\Lambda}X$ reactions (including two-body reaction $X = \Lambda$) are boosted forward such that the anti-protons from the $\bar{\Lambda}$ decay are detected mostly by the FS. In general, a combination of the TOF and RICH looks as the best one for the PID in the whole momentum range of the produced forward hadrons. The combination of TOF and RICH detectors is successfully used in the HERMES experiment [19]. The HERMES RICH thresholds are 2 GeV/c for pions and 4 GeV/c for protons, respectively. Here we focus on PID performed using TOF technique in the forward part of the PANDA detector.

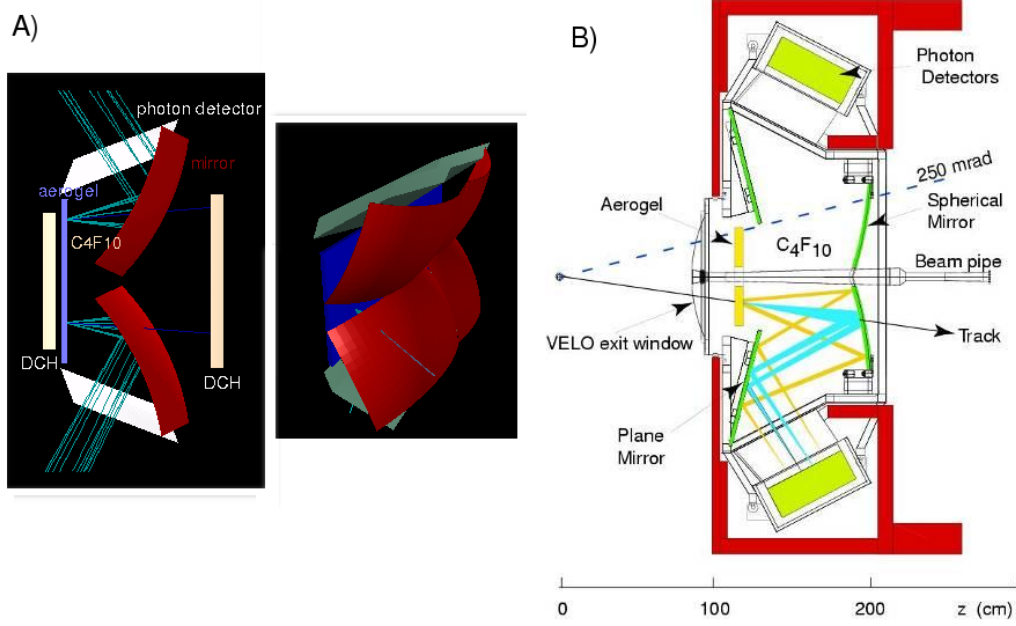


Figure 35: Two options of mirror imaging for the Forward RICH: A) direct, with 4 mirrors looking at different points B) exploiting additional plane mirrors which allow the use of spherical mirrors with a longer focal length.

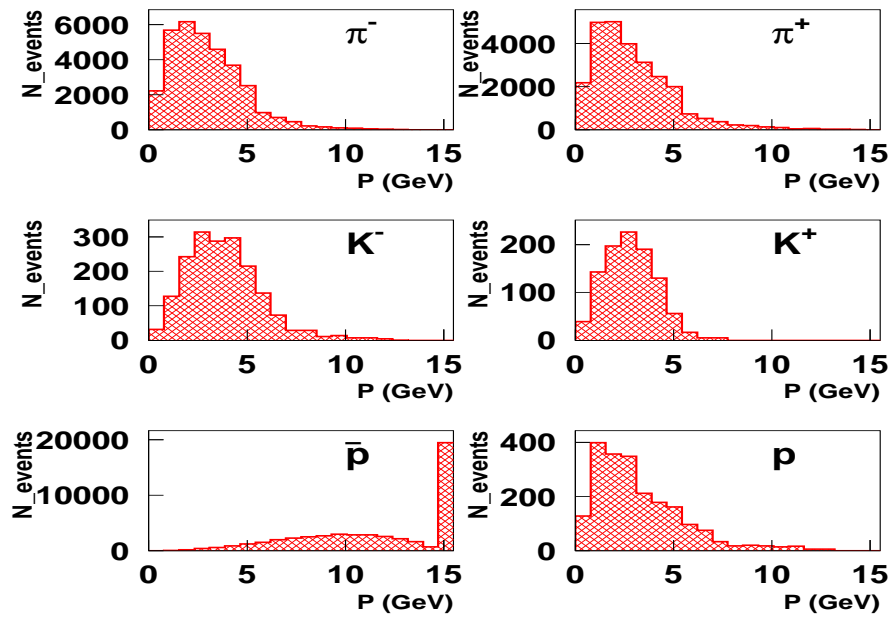


Figure 36: Momentum spectra of charged hadrons emitted within the FS angular acceptance in $\bar{p}p$ collisions at 15 GeV/c.

799 **TOF detector performance.** High-resolution TOF detectors are widely used in many exper-
800 imental setups [20]. The PANDA forward detector consists of two parts: the forward TOF wall
801 and two side TOF walls placed inside the FS dipole gap [1]. The side detectors are designed for

the registration of low momentum particles, not being detected by the forward wall as they are bent inside the FS dipole by the magnetic field to the left or to the right towards the magnet yoke. Unfortunately, the exact configuration of the FS dipole magnetic field is not yet available which makes it difficult to simulate tracking through the dipole. According to our estimations, at the primary beam momentum of 15 GeV/c a particle with momentum below 0.8-1.2 GeV/c (depending on scattering angle) is bent to one of the side detectors. Each side detector consists of 5 vertical scintillation strips with dimensions $100 * 10 * 1.5 \text{ cm}^3$. It is not decided yet whether a magnetic field protected PMT or a SiPMT is to be used for light collection in the side detectors. The forward TOF wall is located at 7.5 m downstream the interaction point. Proceeding from the FS angular acceptance and taking into account deviations in the FS dipole of the particles with momenta higher than $\sim \frac{1}{15}$ of the \bar{p} beam momentum, the dimensions of the forward TOF wall are taken to be 1.4 m in vertical and 5.6 m in horizontal direction. It consists of 66 scintillation counters. A scintillation counter consists of a vertical strip made of plastic scintillator BC408 of 1.5 cm thickness (material budget $\frac{X}{X_0} \approx 3.5\%$). The strip is coupled at the both edges via light-guides to a PMT Hamamatsu R2083 or R4998. The central part of the wall which is close to the beam pipe consists of 20 scintillation counters with $140 * 5 \text{ cm}^2$ strips, and left and right outer parts consist of 46 scintillation counters with $140 * 10 \text{ cm}^2$ strips. Granularity indicated here for the forward TOF and in particular for the side TOF detectors is optional. It is subject to careful MC simulations and experimental investigations of the TOF resolution. The light-pulse amplitude and shape at each end of the strip depends on a particle hit position which is to be specified in off-line analysis using tracking information. The (off-line) time resolution of a TOF wall-scintillation counter is estimated to be 50-60 ps. It is not yet decided which equipment is to be used as a "start" pulse for the time of flight. If no start counter is available a possibility to measure time correlation between two stop counters is considered provided at least two particles from an event is detected by the TOF wall [21]. In all the cases the time resolution of both pulses (start and stop or two stop ones) not worse than 50-70 ps is needed. The overall TOF time resolution then is expected to be on the level of ~ 100 ps.

MC simulations of the detector capabilities. The MC-simulations presented in this section have been performed using DPM generator. A simple cut on the FS acceptance has been applied. No magnetic field has been included in the simulations such that a track has been approximated with a straight line coming out of the interaction point. This is a very coarse approximation for low momentum particles, which however underestimates the TOF length and, respectively, overestimate the value of TOF resolution. The hadron rates calculated in this approach for 4π acceptance and for the FS acceptance at luminosity $2 \cdot 10^{32} \text{ cm}^{-2} \text{ s}^{-1}$ are given in Table 3 and Table 4, respectively.

Table 3: 4π rates for various beam momentum and particles.

Beam momentum (GeV/c)	σ_{tot} (mbarn)	4π rates (1/sec)	$\pi\pm$ (1/sec)	$K\pm$ (1/sec)	Proton (1/sec)	P_{bar} (1/sec)
2	90	$1.8 * 10^7$	$7.17 * 10^6$	$6.47 * 10^4$	$2.23 * 10^6$	$2.25 * 10^6$
5	64.8	$1.3 * 10^7$	$5.4 * 10^6$	$6 * 10^4$	$1.37 * 10^6$	$1.36 * 10^6$
15	50.8	$1 * 10^7$	$4.15 * 10^6$	$1.48 * 10^5$	$9.16 * 10^5$	$9.18 * 10^5$

Distributions of the particle rates over the TOF detector are not uniform and momentum depen-

Table 4: Forward Spectrometer rates for various beam momentum and particles.

Beam momentum (GeV/c)	Forward rates (1/sec)	π^\pm (1/sec)	K^\pm (1/sec)	P (1/sec)	\bar{P} (1/sec)
2	$1.8 * 10^6$	$3.9 * 10^5$	$2 * 10^3$	$1.2 * 10^4$	$1.07 * 10^6$
5	$2.17 * 10^6$	$6 * 10^5$	$7.8 * 10^3$	$3.8 * 10^4$	$9.5 * 10^5$
15	$2.93 * 10^6$	$9.56 * 10^5$	$4.7 * 10^4$	$3.2 * 10^4$	$8.2 * 10^5$

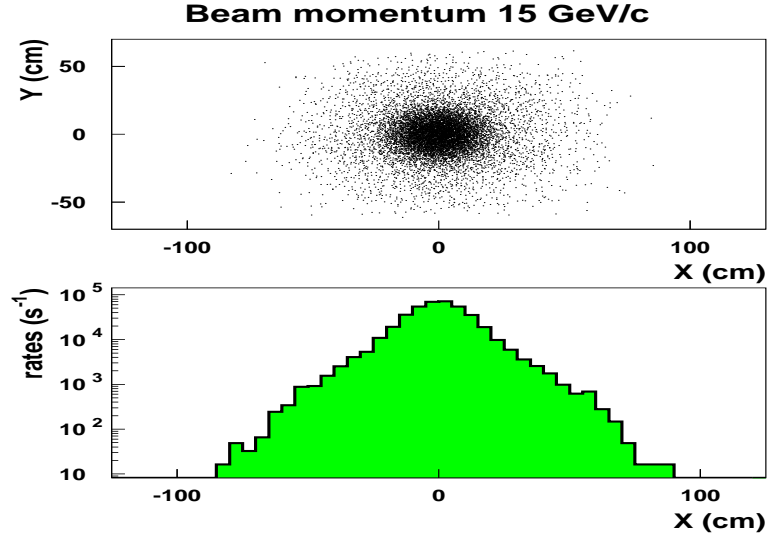


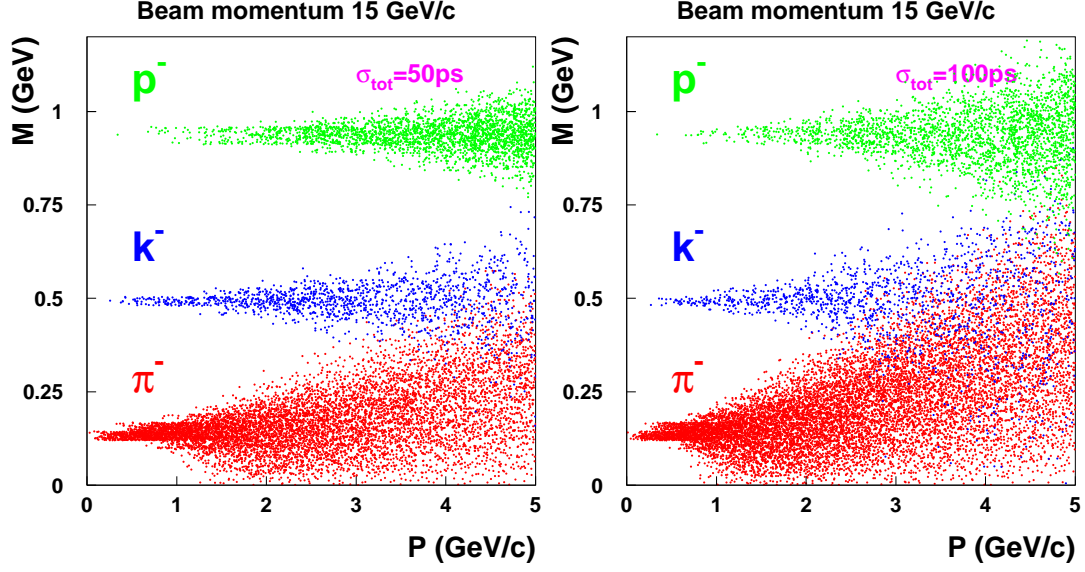
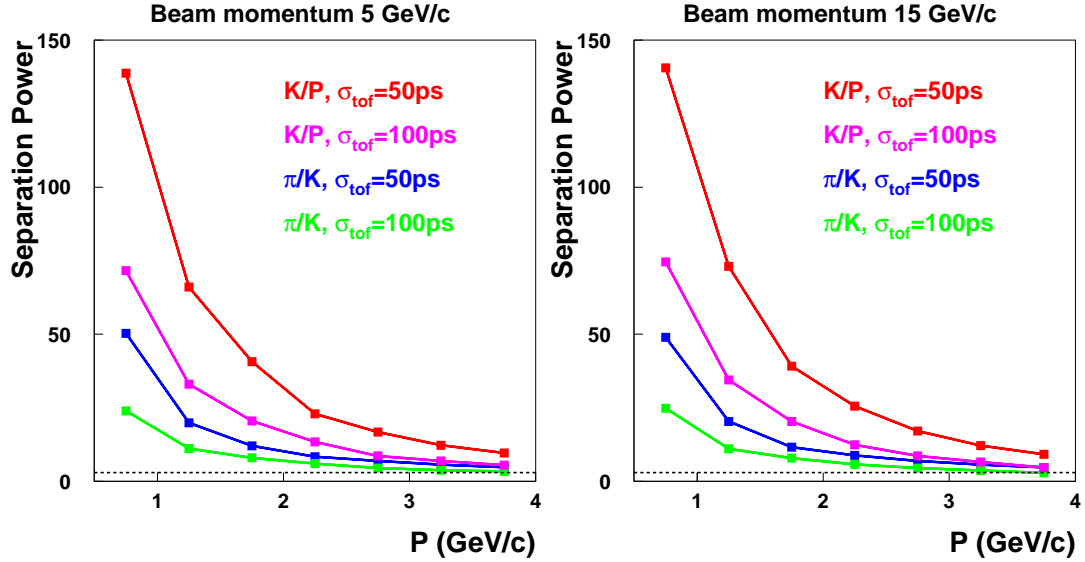
Figure 37: Anti-proton hit distributions for \bar{p} momentum in the range 12 to 15 GeV/c (mostly elastically scattered anti-protons). Upper panel: areal distribution over XY-plane at the position of the forward TOF wall ($X=Y=0$ are primary beam coordinates), lower panel: count rate per a scintillation counter. Note that the bin width is taken equal to the central strip width (5 cm).

dent. The forward yields ($\frac{dN}{d\cos\theta}$, where θ is the scattering angle) are peaked at $\theta = 0$ with various slopes. As seen from Table 4 the highest rate is expected for anti-protons, mostly for elastically scattered anti-protons (see the peak of elastic \bar{p} scattering in Fig.36). As the cross section for elastic scattering is a very steep function of θ practically all anti-protons are emitted within the FS acceptance. In Fig.3.9 anti-proton hit distributions for \bar{p} momentum in the range 12 to 15 GeV/c are shown. As seen from the count rate per a scintillation count (lower panel) this rates are low enough even in the central part of the detector and does not restrict its operational capabilities. A momentum p and charge sign of a forward emitted particle is measured by tracking through the dipole magnet of the FS with momentum resolution typically better than 1%.

For a detected particle its mass m can be expressed as

$$m = p \sqrt{\frac{t^2}{t_c^2} - 1}. \quad (5)$$

Here $t_c = L/c$ where c is speed of light, L is the TOF length, i.e. the length of the particle track counted from the interaction point to a "stop" counter; t is the measured time of flight, $\frac{t}{t_c} = \frac{1}{v}$

Figure 38: *Reconstructed masses for hadrons of a negative charge.*Figure 39: *Separation power vs. particle momentum, dashed line - 3σ separation*

850 where v is the particle velocity ($c = 1$). A fractional uncertainty in determination of the particle
 851 mass is

$$\frac{\delta m}{m} = \sqrt{\left(\frac{\delta p}{p}\right)^2 + \gamma^4 \left(\frac{\delta t}{t}\right)^2}, \quad (6)$$

852 where $\gamma = \frac{1}{\sqrt{1-v^2}}$. The TOF wall is positioned at 7.5 m from the target which corresponds to
 853 $t_c^{min} = 25$ ps. Due to relativistic factor γ^4 the TOF resolution of ~ 100 ps dominates the mass
 854 smearing for relativistic particles while the momentum resolution of 1% has just a little effect.
 855 An additional δm may come from uncertainty in L (or t_c) due to tracking in the magnetic field
 856 of the FS dipole. It is estimated to be on the level of a few ps and ignored. An example of

the forward TOF wall capability to identify hadrons is demonstrated in Fig.38 where the hadron masses calculated with the help of Eq.5 are plotted versus the hadron momentum.

Separation power. PID quality of the TOF wall detector is quantified using a value of Separation Power SP defined in section 4.1 of this document. In these calculations the binning has been done in the hadron momentum in the range 0.5 to 4 GeV/c (7 bins). In each bin the hadron mass distribution is approximated with a gaussian. The central (mass) position has been fixed according to PDG while the dispersion σ_{mass} is found by fit to the experimental histogram. Separation powers for pairs of particles π/K and K/P calculated in such a way are presented in Fig.39.

3.10 Forward Calorimeter

The forward calorimeter will consist of two parts: the electromagnetic calorimeter and the hadron calorimeter serving also as a muon filter.

3.10.1 Electromagnetic calorimeter

For the electromagnetic calorimeter, for its large size and high energies of impinging particles, the most suitable seems the Shaslyk technique, allowing to make a reasonable compromise between the energy resolution and the price. It has been proved to work well in other experiments, *e.g.* E865 [23] and KOPIO [24]. In the latter the achieved energy resolution amounted to $4\%/\sqrt{E}$. The calorimeter consists of modules built a form of lead-scintillator sandwiches that are read out via wave length shifting (WLS) fibers penetrating them through prefabricated holes. The module size of $11 \times 11 \text{ cm}^2$ is a compromise between the position resolution and the cost and complexity. The major features of the planned electromagnetic calorimeter are as follows:

- 400 layers of Pb and scintillator (ca. $20 X_0$),
- effective Moliere radius 60 mm,
- thickness of a single lead layer $d(\text{Pb}) = 0.275 \text{ mm}$,
- thickness of a single scintillator layer $d(\text{Scint.}) = 1.5 \text{ mm}$,
- number of fibers per module: 72 or 144,
- readout: PMT
- design resolution: $4\%/\sqrt{E}$,
- active area of $297 \times 143 \text{ cm}^2$, corresponding to 27×13 modules.

Several test setups with modules of different sizes have been built in IHEP–Protvino, and now they are a subject of ongoing beam tests. Fig. 40 presents a test setup of 3×3 modules and a layout of unpacked modules. The results of the tests are very encouraging. Based on the beam tests performed in 2007, the energy resolution was parametrised as follows:

$$\frac{\sigma_E}{E} = \frac{a}{E} \oplus \frac{b}{\sqrt{E}} \oplus c \quad [\%]$$

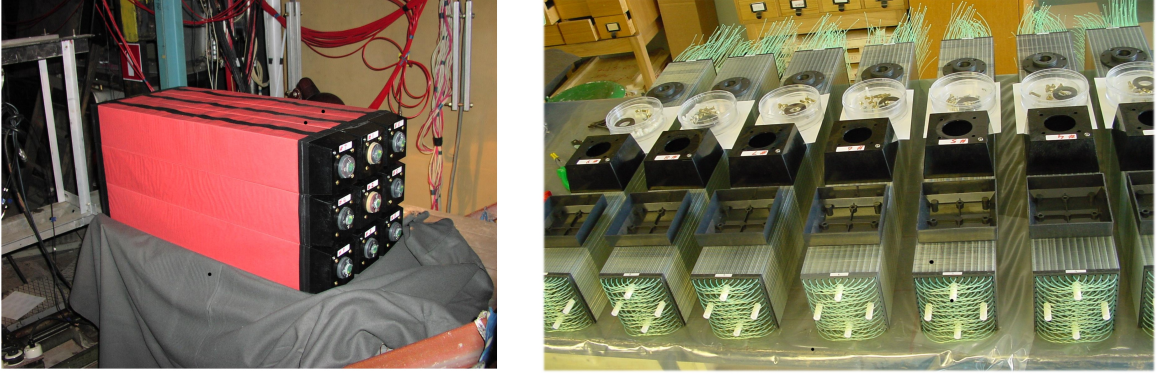


Figure 40: Left: a test setup of 9 modules, right: unpacked shashlyk modules.

where $a = (3.5 \pm 0.3)$ GeV, $b = (2.8 \pm 0.2)$ GeV $^{\frac{1}{2}}$, $c = 1.3 \pm 0.04$. The numbers are in line with the MC simulations and correspond to the energy resolution of 4.7% at 1 GeV and 1.9% at 5 GeV, which is comparable with the design value. Further test beam studies will include prototype energy and position resolution for modules of 55×55 mm 2 size as well as test of π^0 reconstruction capabilities in the energy range up to 15 GeV.

A series of simulations, based on the so-called *old code*, have been done in order to investigate performance of calorimeter of this type for electron/pion separation. Different momenta (1 GeV/c and 5 GeV/c) of electrons and pions as well as different lateral dimensions of the modules were simulated. Detector response and cuts imposed in order to select electrons of 5 GeV/c momentum in the 110×110 mm 2 modules are shown as an example of the procedure, see fig. 41. A particle

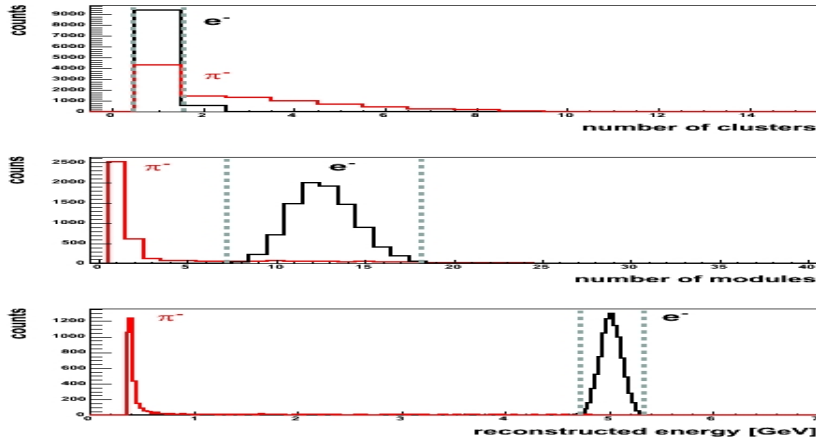


Figure 41: Detector response to single pion (red) and single electron (black) events is shown in terms of number of reconstructed clusters (top), number of fired modules (middle) and reconstructed energy (bottom). Cuts shown by the dashed lines were used to select electrons.

was identified as an electron if the associated signal fulfilled the three cuts presented in fig. 41 by the dashed lines. Results of the simulations are collected in the tables 5 and 6. For both investigated momenta, reduction of the module size from 110×110 mm 2 to 55×55 mm 2 reduces the number of the pions misidentified as electrons by a factor of two.

Module size [mm ²]	e^- identified [%]	π^- misidentified as e^- [%]
30×30	84.6	0.2
55×55	93.3	0.4
110×110	97.4	0.8

Table 5: Results of PID using the shashlyk calorimeter for 5 GeV/ c electrons and pions.

Module size [mm ²]	e^- identified [%]	π^- misidentified as e^- [%]
55×55	96.2	4.7
110×110	98.1	8.7

Table 6: Results of PID using the shashlyk calorimeter for 1 GeV/ c electrons and pions.

3.10.2 Hadron calorimeter

The hadron calorimeter will be placed around 8 m downstream the target and extends 440 cm horizontally and 180 cm vertically. Its task is to measure energies of neutrons and antineutrons, large numbers of which bombard the region of acceptance covered by the Forward Spectrometer. Apart from that, it gives fast signal for triggering on reactions with forward scattered hadrons. Last but not least, the detector will be used to discriminate between charged hadrons and muons. This will be achieved by combining the energy loss information with the information obtained from the muon counters.

Until recently, the option that was considered for hadron calorimetry at $\bar{\text{PANDA}}$ was a detector of MIRAC type [26]. In this design layers of steel are sandwiched with layers of scintillator and read out via WLS fibres attached to PMTs. The obtained energy resolution for the hadronic shower amounted to $0.034 \oplus 0.34/\sqrt{E[\text{GeV}]}$. It was planned to use that detector as a muon filter by placing muon counters behind it.

Currently another option is being investigated and seems more adequate solution for the $\bar{\text{PANDA}}$ needs, called Hadron & Muon Identifier based on a Range System, HMI/RS [27]. In this design sections of steel–scintillator sandwich are interlaced with gas detectors allowing observation of the cascade or tracking of muons. HMI/RS allows much better muon identification, for the price of only slight deterioration of the relative energy resolution. Currently the detector is in the phase of MC optimisation and prototyping [27].

4 Tools

In this section the TAG work is described. To evaluate the performance of the detectors the PID TAG defined the "Separation Power" as the right tool. With the help of "Phase Space Plots" (section 4.2) the angular coverage and the corresponding particle momenta could be determined. The "Fast Simulation" (section 4.3) was used to map the separation power over the full angular and momentum range. In a second step important reactions and their relevant background channels were simulated. Thus the regions where a good separation power is needed could be identified and checked whether the detector performance is sufficient there.

4.1 Separation Power

This document completely deals with the quality of the particle identification of the projected PANDA detector. Thus the major issue upon which decisions can be made is a proper definition of classification quality or performance.

The according concept chosen for that purpose called 'Separation Power' bases on the assumption that the particular observables of objects of different classes exhibit more or less gaussian distributions.

Consider the situation illustrated in fig. 42:

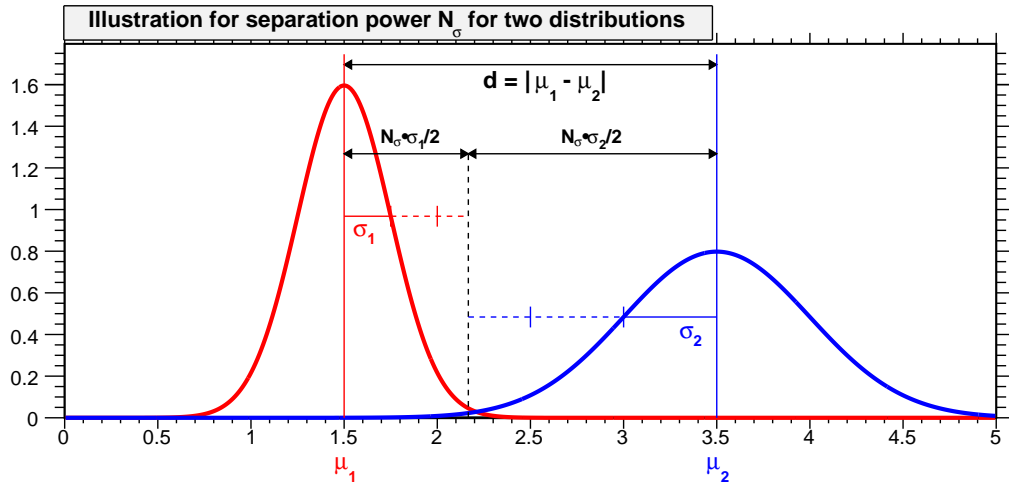


Figure 42: Illustration for the definition of separation power.

There are plotted two gaussian distributions $G_1(x) \equiv G(x; \mu_1, \sigma_1)$ and $G_2(x) \equiv G(x; \mu_2, \sigma_2)$ with mean values $\mu_1 = 1.5$ and $\mu_2 = 3.5$ and standard deviations $\sigma_1 = 0.25$ and $\sigma_2 = 0.5$. This could be e. g. the probability density distributions of the dE/dx measurements for two particle species in a small momentum range. Obviously the distributions are separable quite reasonably, but what is the measure for the separation potential?

A proper definition would be to define a particular classifier, e.g. every particle with property $x_0 < 2$ is considered as member of class 1 (red). Then one can determine two quantities which are of relevance for the quality of classification. The first one is the efficiency, which is part of the distribution 1 (or a random sample of measurements following this distribution) which is identified correctly analytically corresponding to the integral

$$\epsilon = \int_{-\infty}^{x_0} G_1(x) dx \quad (7)$$

for a normalized Gaussian. The second quantity is the misidentification level given by the integral

$$\text{mis-id} = \int_{-\infty}^{x_0} G_2(x) dx \quad (8)$$

which is part of the distribution 2 in the same region thus identified incorrectly as being of class

1. These two values would define clearly the performance of the classifier³. But this solution cannot be applied in case when one does not want to define a particular selector. It rather has to be defined a measure for the prospective performance of a possible selector.

Exactly this is the aim of the separation power N_σ which relates the distance of the mean values $d = |\mu_1 - \mu_2|$ of the two distributions to their standard deviations σ_1 and σ_2 . The usual unit of N_σ is 'number of gaussian sigmas of the separation potential', which is supposed to relate the number with gaussian integral values.

There are actually a lot of different definitions for that quantity on the market but it has been found an agreement within the PID TAG on the following definition:

$$N_\sigma = \frac{|\mu_1 - \mu_2|}{\sigma_{\text{avg}}} = \frac{|\mu_1 - \mu_2|}{(\sigma_1/2 + \sigma_2/2)} \quad (9)$$

This relationship is illustrated in fig. 42. The black dashed line marks the position x_0 between the two distributions, for which the differences to each mean value $|\mu_1 - x_0| = N_\sigma \cdot \sigma_1/2$ and $|\mu_2 - x_0| = N_\sigma \cdot \sigma_2/2$ are the same in terms of σ 's.

This means a separation of e. g. $N_\sigma = 4\sigma$ corresponds to a gaussian integral

$$I = \int_{-\infty}^{\mu+4\sigma/2} G(x; \mu, \sigma) dx = 0.9772 \quad (10)$$

which shall express an efficiency around $\epsilon \approx 97.7\%$ or a mis-ID level around $\text{mis} = 100\% - 97.7\% \approx 2.3\%$ or both. This integration up to half the number of sigmas $N_\sigma/2$ seems a bit contra intuitive but is common notion and therefore has been kept for the considerations in this document. Another feature of this definition is that it is symmetric for both classes or distributions, even with different σ 's. Furthermore for the particular case of normalized gaussian distributions and a selector requiring $x < x_0$ for classifying class 1 objects in the upper example, the efficiency ϵ and purity π for this selection have the same value, since

$$\epsilon = \frac{\int_{-\infty}^{x_0} G_1(x) dx}{\int_{-\infty}^{+\infty} G_1(x) dx} = \frac{\int_{-\infty}^{x_0} G_1(x) dx}{1} = \frac{\int_{-\infty}^{x_0} G_1(x) dx}{\int_{-\infty}^{x_0} G_1(x) dx + \int_{x_0}^{+\infty} G_1(x) dx} \quad (11)$$

$$= \frac{\int_{-\infty}^{x_0} G_1(x) dx}{\int_{-\infty}^{x_0} G_1(x) dx + \int_{-\infty}^{x_0} G_2(x) dx} = \frac{\int_{-\infty}^{x_0} G_1(x) dx}{\int_{-\infty}^{x_0} G_1(x) + G_2(x) dx} = \pi \quad (12)$$

Tab.7 lists on the left hand side the mis-id levels $1 - \int G(x)dx$ with one-sided (1s) and two-sided (2s) gaussian integrals for different values of N_σ , on the right hand side the corresponding values of the separation power for given levels of mis-id according to the upper definition. It shall be emphasized again that for given values N_σ the integration is only performed up to $N_\sigma/2$, therefore the mis-id levels might seem surprisingly high for given number of σ 's separation.

Taking into account that quantities in reality never have gaussian shape the values σ in fact are not necessarily gaussian sigmas but calculated as the root-mean-square (which actually is the standard deviation)

$$\sigma_{\text{rms}} = \sqrt{\sum_i (x_i - \mu)^2} \quad (13)$$

³For Bayes' classification a flux correction would have to be taken into account additionally. This requires of course knowledge about a posteriori probabilities of particle fluxes which not necessarily is available since significantly dependent on the given trigger and reaction type.

what in case of gaussian distributions would be indeed identical with the gaussian σ from above.
For the given example in fig. 42 the definition (9) computes to

$$N_{\sigma,1} = \frac{2}{0.25/2 + 0.5/2} = \frac{2}{0.375} = 5.333 \quad .$$

Another issue which directly is connected with the definition above is the question how to define the combined separation $N_{\sigma,\text{tot}}$ e.g. for values $N_{\sigma,i}$ achieved by various detector components to express the overall performance. The agreement of the PID-TAG concerning this was to consider the quadratic sum

$$N_{\sigma,\text{tot}} := \left(\sum_i N_{\sigma,i}^2 \right)^{1/2} \quad (14)$$

as a good measure. In order to evaluate the goodness of that expression it first of all is necessary to make aware what meaning the value N_σ has in terms of probability. When considering something similar to equation (10) as a appropriate measure, namely the integral of a Gaussian from $-N_\sigma/2$ to $+N_\sigma/2$ the expression for the corresponding probability of mis-identification is given by

$$P_{\text{mis}}(N_\sigma) = 1 - \int_{-N_\sigma/2}^{+N_\sigma/2} G(x; \mu = 0, \sigma = 1) dx \quad (15)$$

which directly defines the mis-identification probability for n statistically independent separation capabilities as the product

$$P_{\text{mis,tot}} = P_{\text{mis}}(N_{\sigma,1}) \times \cdots \times P_{\text{mis}}(N_{\sigma,n}) \quad (16)$$

in addition. Hence equation (15) implicitly specifies $N_{\sigma,\text{tot}}$ as that value where the integral yields exactly $P_{\text{mis,tot}}$. This procedure has been pursued for two values $N_{\sigma,1}$ and $N_{\sigma,2}$ as presented in fig. 43. In (a) the combined separation power is shown as 2-dimensional function of the two input values, (b) presents the difference

$$\Delta = \left| N_{\sigma,\text{tot}} - \sqrt{N_{\sigma,1}^2 + N_{\sigma,2}^2} \right| \quad (17)$$

of the resulting value and equation (14), which obviously reasonably reproduces the correct value with a maximum deviation of about 0.5σ in the range of single values up to $N_\sigma = 6$.

4.1.1 Parameterization of the Electromagnetic Calorimeter

Although not implemented in the Fast Simulation, a parameterization of part of the response of the EMC has been pursued for the estimation of an overall PID quality. It is based on fully simulated data but only information about electron-pion-separation was taken into account up to now. Fig. 44 (a) shows the distributions of the parameterized ratio of the calibrated cluster energy in the electromagnetic calorimeter and the reconstructed track momentum E_{clus}/p for simulated electrons (green) and pions (black). The source for modelling the parameterizations can be found in the PANDA Physics Book [3]. It is clearly visible that above momenta of approximately 500 MeV this quantity is a powerful tool to separate electrons from pions, demonstrated in fig.44 (b), where the separation power has been determined dependent of the track momentum p by the

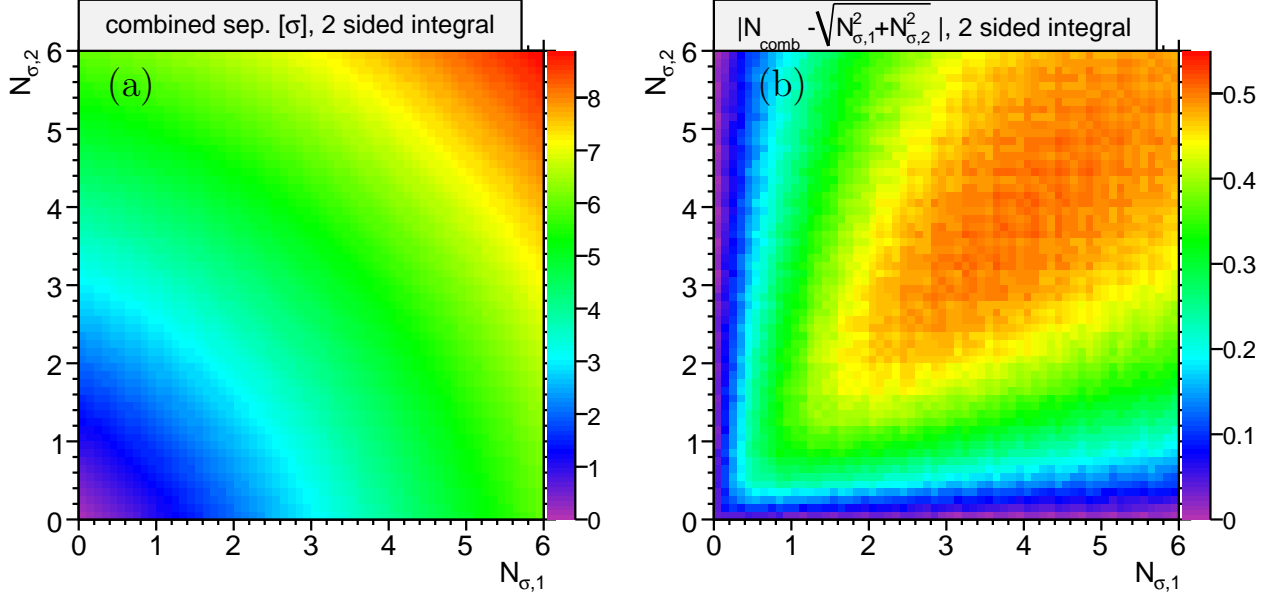


Figure 43: (a) Graphical representation of the combined separation power $N_{\sigma,\text{tot}}$ of two values $N_{\sigma,1}$ and $N_{\sigma,2}$, (b) the corresponding difference $|N_{\sigma,\text{tot}} - \sqrt{N_{\sigma,1}^2 + N_{\sigma,2}^2}|$.

N_σ	mis-id (1s) [%]	mis-id (2s) [%]	mis-id [%]	N_σ (1s)	N_σ (2s)
1.0	30.854	61.708	10.000	2.6	3.3
2.0	15.769	31.538	5.000	3.3	3.9
3.0	6.681	13.361	1.000	4.6	5.1
4.0	2.254	4.507	0.500	5.1	5.6
5.0	0.621	1.242	0.100	6.2	6.6
6.0	0.133	0.266	0.050	6.6	7.0
7.0	0.023	0.047	0.010	7.4	7.8
8.0	0.003	0.006	0.005	7.8	8.1
9.0	0.000	0.001	0.001	8.5	8.8

Table 7: Relation between separation power and mis-id level

definitions given above. Since no θ dependence was available this separation power is assumed to be constant over the complete θ range.

According to the software chapter of the PANDA Physics Book e/π separation is the most difficult one. Therefore this distribution is assumed to also hold for separating electrons from any other particle species.

As a very naive assumption without a proof the additional separation power provided by the EMC for any other particle combination is taken to be 1σ over the complete phase space covered by the EMC.

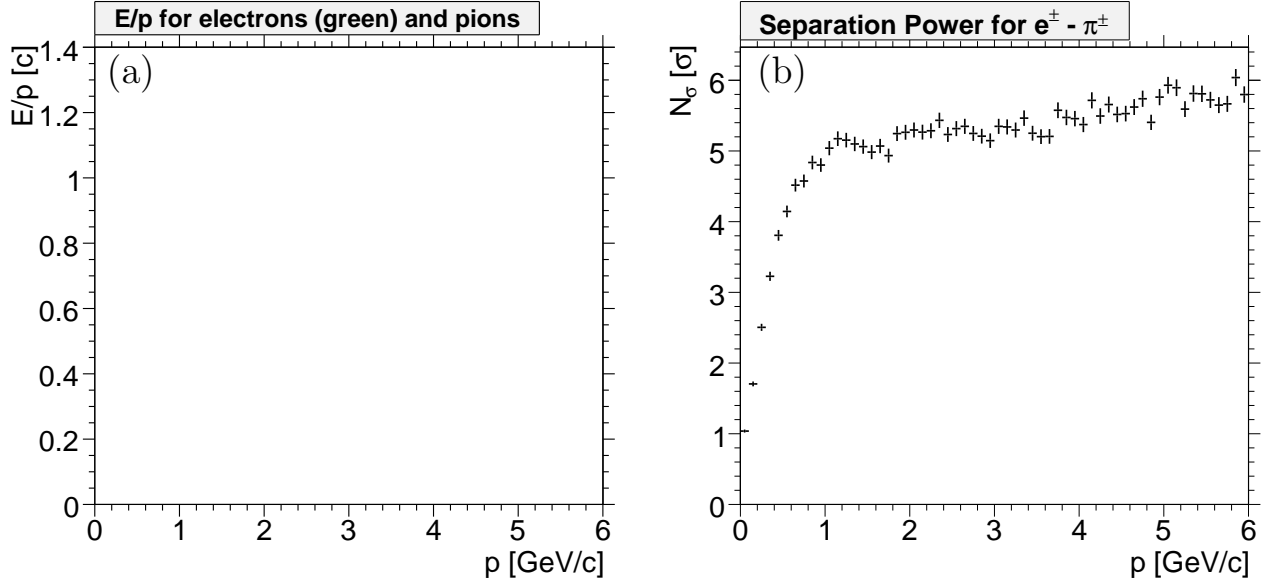


Figure 44: (a) Parameterized distribution of E_{clus}/p for electrons and pions and (b) the resulting separation power N_σ as function of the track momentum p .

4.1.2 Mapping Separation Power

For the purpose of illustration the relationship between kinematic distributions of physics channels and the PID quality the separation power defined in (9) has been determined as 2-dimensional histogram in phase space (p, θ) . Therefore it was necessary to compute the mean value μ and standard deviation σ for every bin i with $[p_i \dots p_i + dp; \theta_i \dots \theta_i + d\theta]$ for bin widths dp and $d\theta$ for every detector and particle species.

One technical remark: To avoid the computation of $(x - \mu)$ for every measurement in order to determine σ , which is very time consuming for large datasets, the relationship

$$\sigma^2 = \frac{\sum x_i^2 - N \cdot \mu^2}{N - 1} = \frac{N \cdot \sum x_i^2 - (\sum x_i)^2}{N^2 - N} \quad (18)$$

has been exploited which does not require a previous calculation of the mean value $\mu = \bar{x}$.

In order to evaluate the contributions of the various detectors to the overall classification potential, the separation power defined above has been determined for every single detector component and all possible particle combinations, which add up to the following 10 possibilities:

1. $e^\pm - \mu^\pm, e^\pm - \pi^\pm, e^\pm - K^\pm, e^\pm - p/\bar{p},$
2. $\mu^\pm - \pi^\pm, \mu^\pm - K^\pm, \mu^\pm - p/\bar{p},$
3. $\pi^\pm - K^\pm, \pi^\pm - p/\bar{p},$
4. $K^\pm - p/\bar{p}.$

The results are determined based upon 5 million isotropic distributed single track events with particle momenta up to 6 GeV/ c .

Figs. 45 and 47 show as examples the p - θ -dependent separation power for $e^\pm - \pi^\pm$, $\pi^\pm - K^\pm$ and $K^\pm - p/\bar{p}$ for all 8 detector components

- Micro Vertex Detector (MVD)
- Barrel Time of Flight System (TOF)
- Barrel DIRC
- Disc DIRC
- Ring Image Cherenkov Detector (RICH)
- Electro Magnetic Calorimeter (EMC)
- Straw Tube Tracker (STT)
- Time Projection Chamber (TPC)

under investigation. The color codes in these 2 dimensional representations correspond to the numbers of σ 's (N_σ) of separation with a cutoff $N_\sigma > 8$. Thus in the red regions are possibly values above that limit.

To get an impression of the overall particle identification performance the values $N_{\sigma,i}$ from the different detectors i have been combined by quadratic summation according to (14) under the assumption of statistically uncorrelated $N_{\sigma,i}$. Since there are two central tacker options (STT and TPC) which cannot contribute to the same total separation, two different scenarios with either the STT or the TPC are considered separately. Fig. 48 shows the combined information for the STT option and fig. 49 for the detector setup with the TPC as central tracker. All maps are based on the requirement of positive identification of a particle species. This means, that particle type A is only considered to be distinguishable from another particle type B when both create a signal in the particular detector and the given phase space region.

One should keep in mind that the conclusive power of separations involving electrons and muons is limited for the time being since only limited information from the electromagnetic calorimeters and none for the muon detectors has been incorporated so far, which has significant impact on electron and muon identification respectively.

4.2 Phase Space Plots

The question which has to be answered concerning particle identification is not only how good the classification works or has to work, but also in which region of the phase space one needs good separation, and in which parts one possibly doesn't need almost any.

Therefore it is a crucial task to visualize the kinematic behaviour of various important physics channels to get a better insight to the above issue. Furthermore not only kinematic distributions of signal events are relevant, since good PID is only useful in cases where kinematic overlap of particles of species A from signal events and particles of species B from background events really

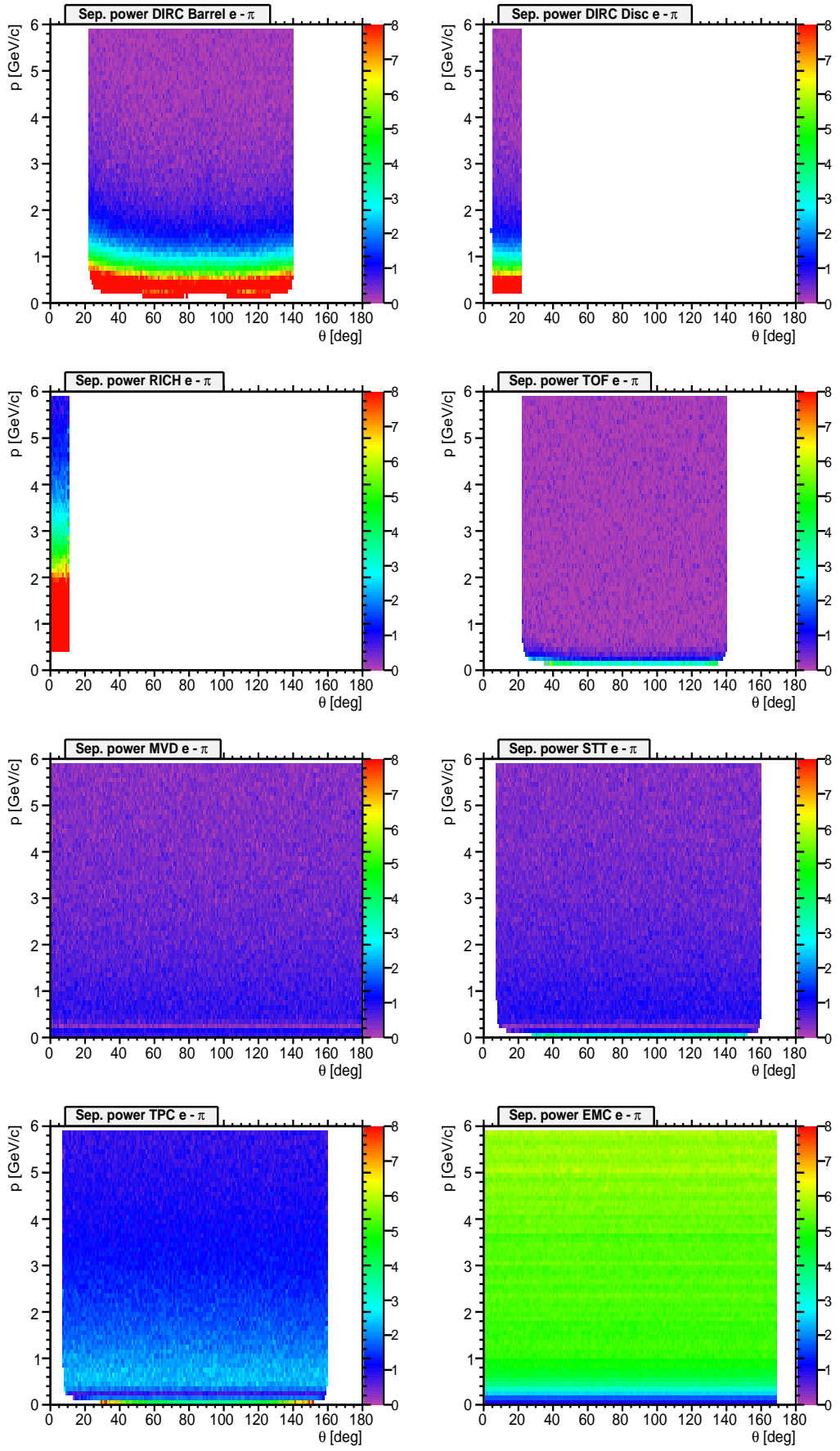


Figure 45: Map of separation power for $e^\pm\pi^\pm$ separation. Color code corresponds to $N_\sigma = 0 \dots 8$.

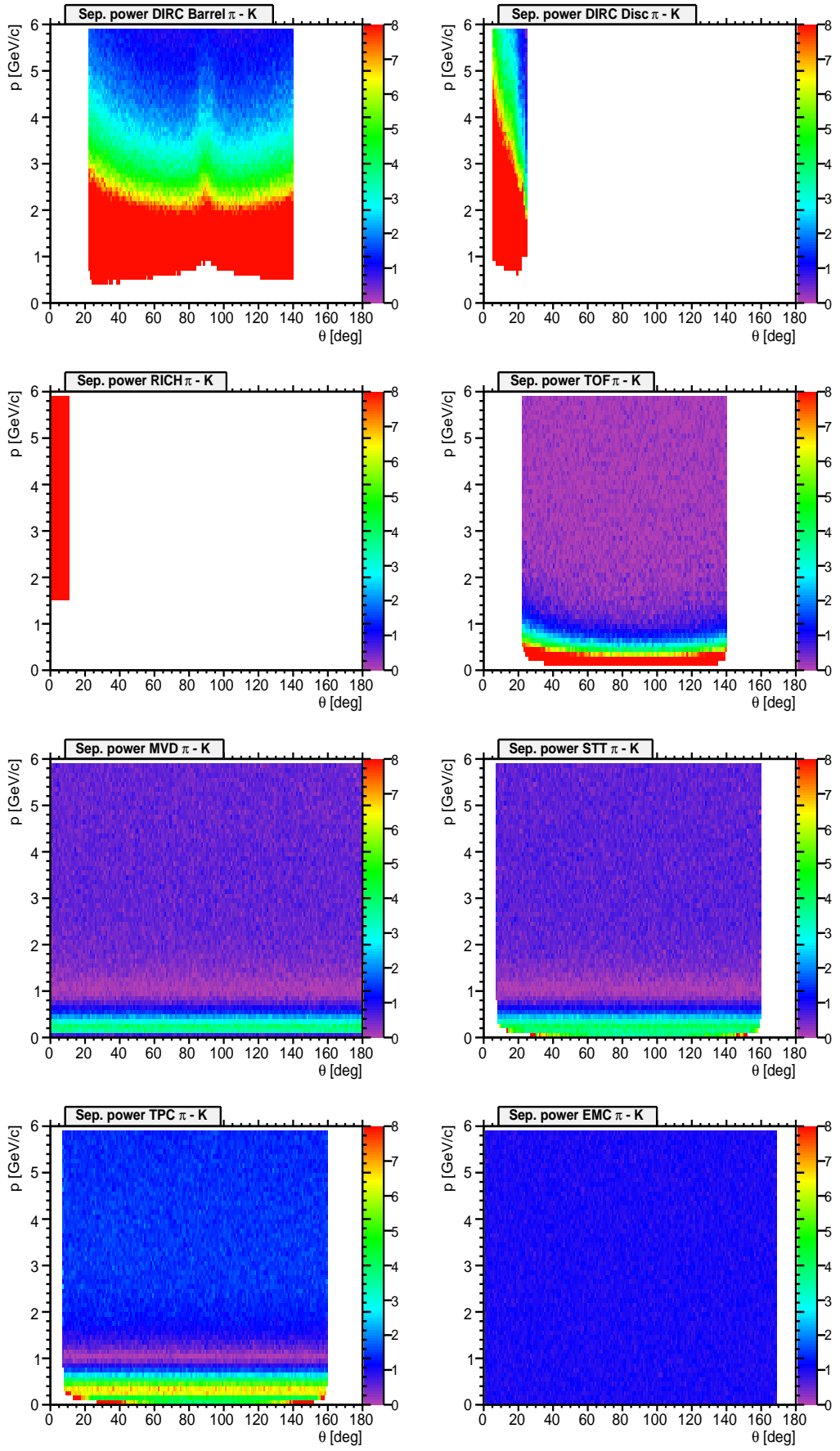


Figure 46: Map of separation power for π^\pm - K^\pm separation. Color code corresponds to $N_\sigma = 0 \dots 8$.

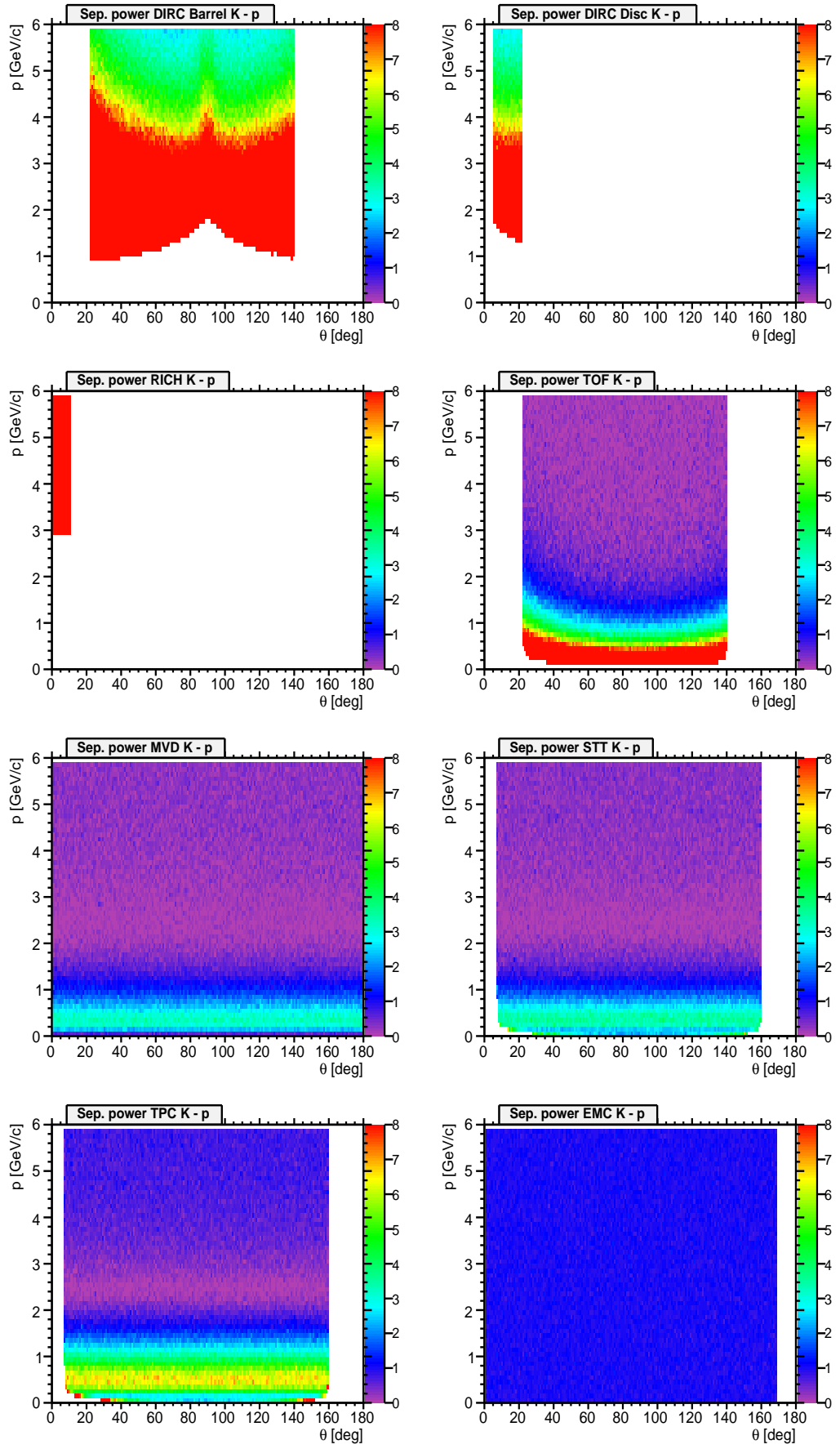


Figure 47: Map of separation power for K^\pm - p/\bar{p} separation. Color code corresponds to $N_\sigma = 0 \dots 8$.

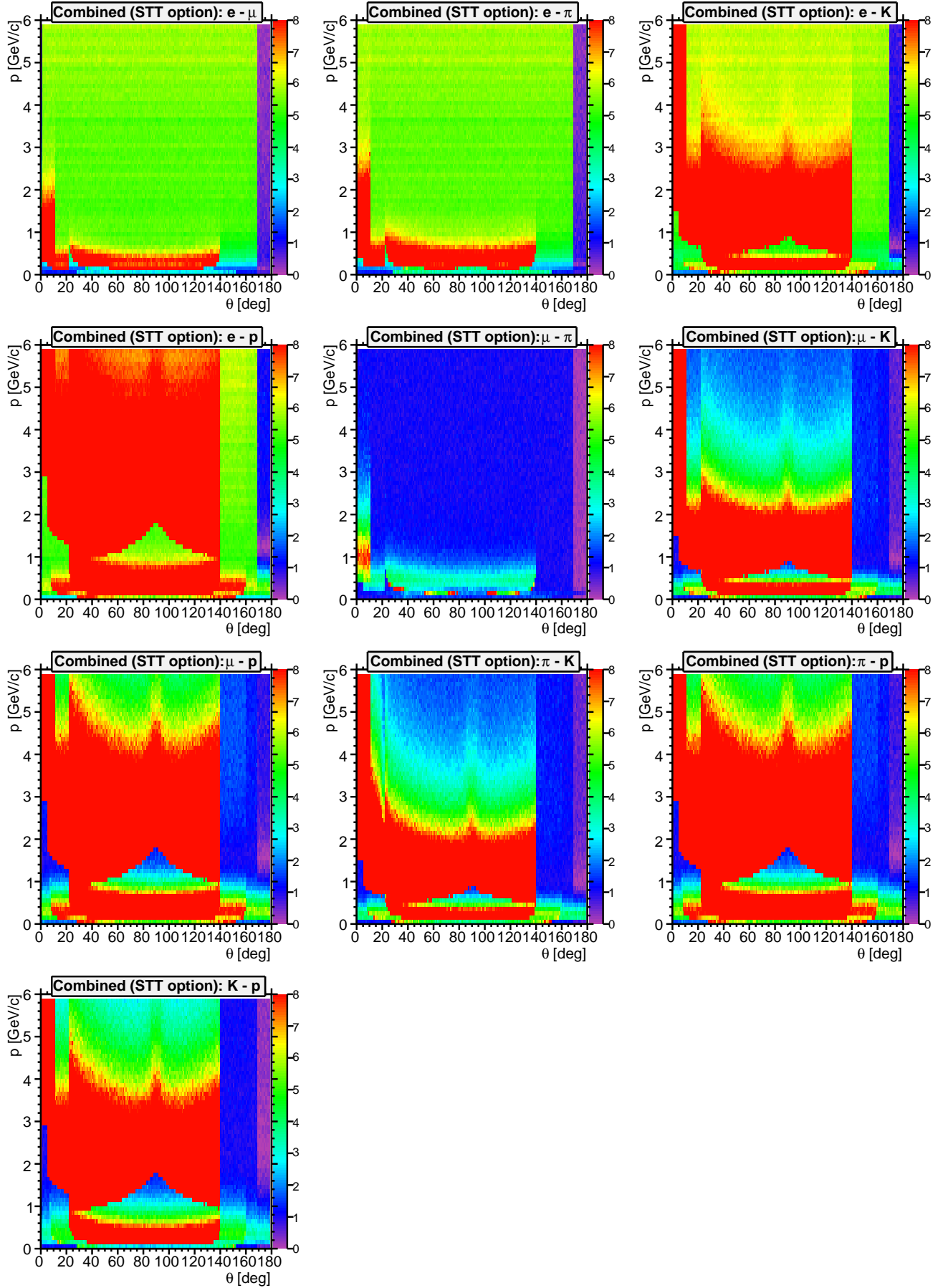


Figure 48: Combined map of Separation Power with STT as central tracker option including the TOF system. Color code corresponds to $N_\sigma = 0 \dots 8$.

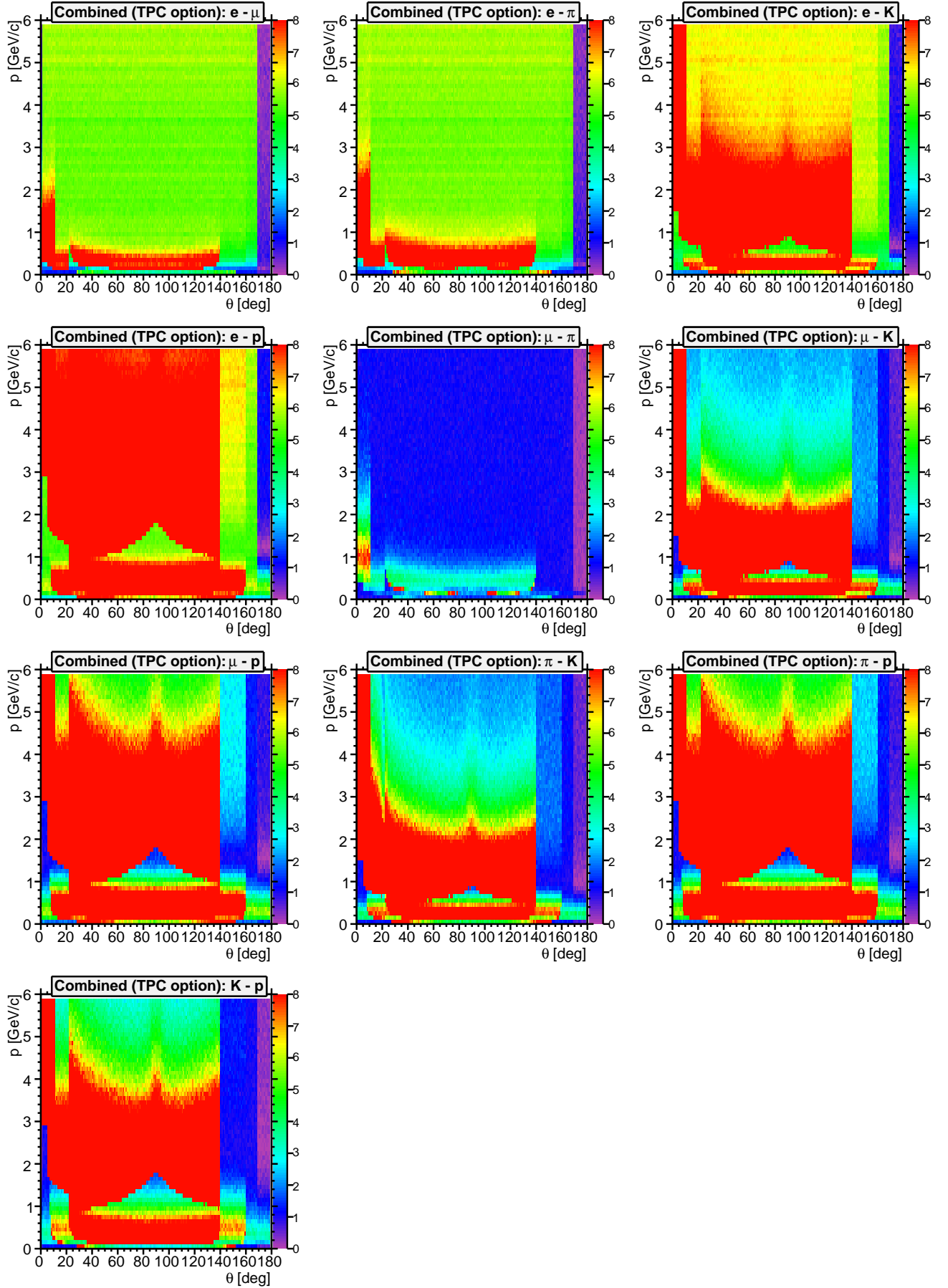


Figure 49: Combined map of Separation Power with TPC as central tracker option including the TOF system. Color code corresponds to $N_\sigma = 0 \dots 8$.

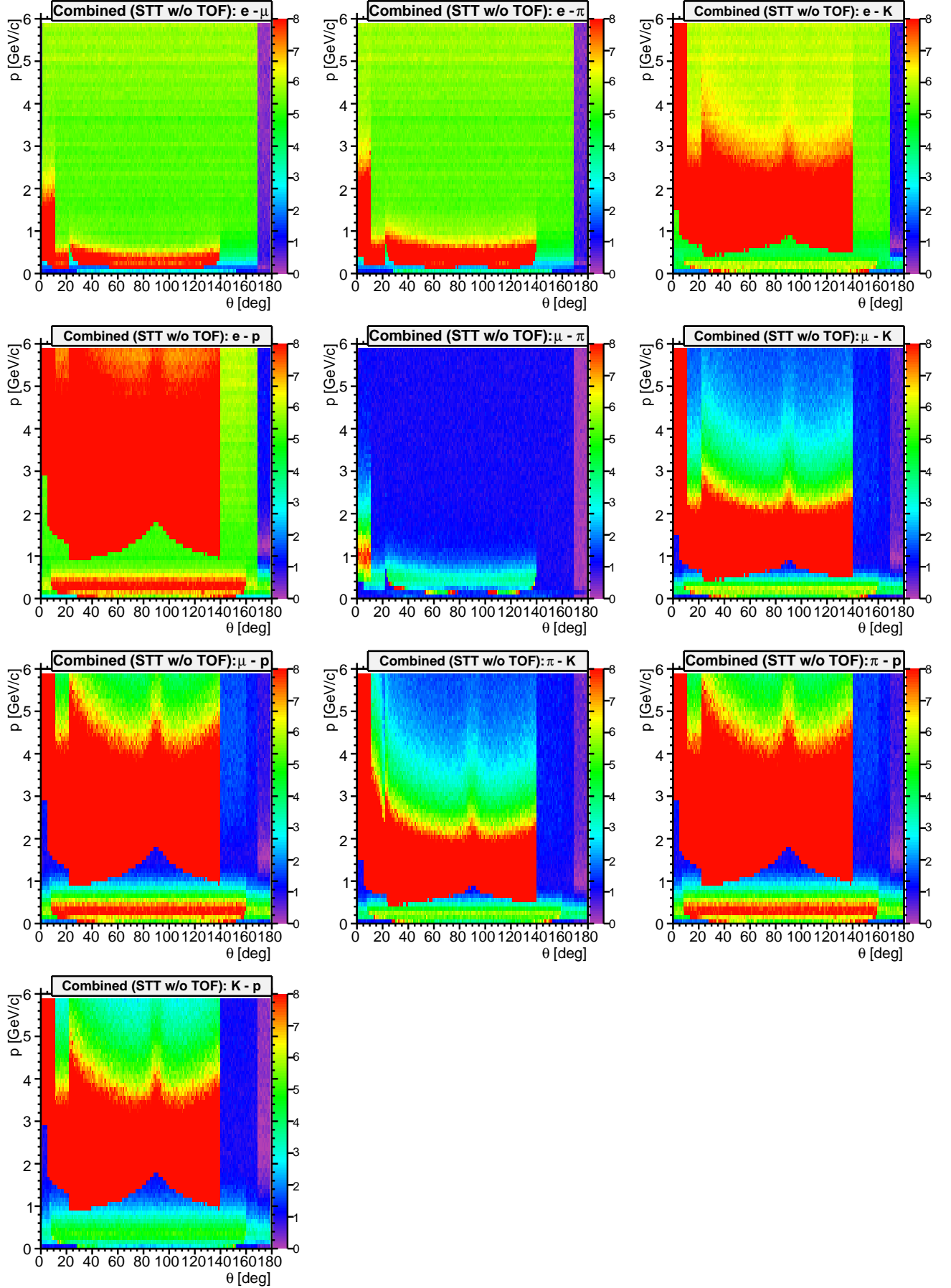


Figure 50: Combined map of Separation Power with STT as central tracker option without the TOF system. Color code corresponds to $N_\sigma = 0 \dots 8$.

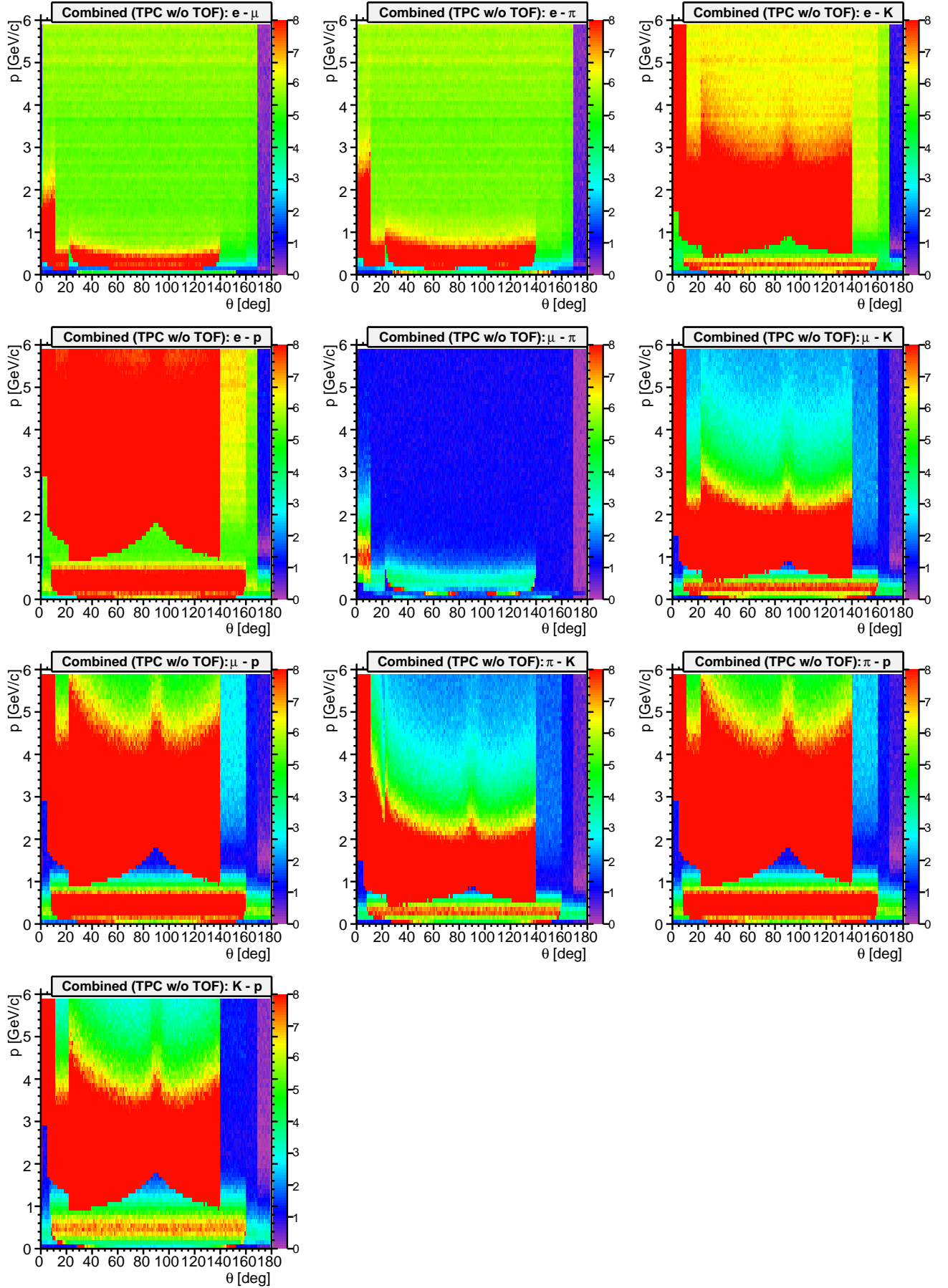


Figure 51: Combined map of Separation Power with TPC as central tracker option without the TOF system. Color code corresponds to $N_\sigma = 0 \dots 8$.

exists. In scenarios where particles of the same type A appear in signal as well as background events in the same phase space location the background suppression cannot be improved by means of PID.

Following a request of the PID TAG phase space plots from all the reactions relevant for the physics book were produced. The set of plots shows for each particle species of the reaction the particle momentum versus theta angle.

Tab. 9 lists part of the benchmark channels discussed in the PANDA Physics Booklet and some additional ones to study inclusive open charm analysis together with relevant background channels. In particular channels were investigated which might suffer significantly from insufficient PID capabilities⁴.

The acronym DPM in the table refers to generic background events generated with the **D**ual **P**arton **M**odel generator. In the last column references to the corresponding figures are given. Tab. 8 gives some standard decay channels which apply to cases where nothing different is specified in tab. 9.

In figs. 52 - 56 kinematic distributions (momentum p vs. dip angle θ) at various beam momenta are shown for some of the signal-background scenarios listed in 9, one particle species per plot. To easier spot signal and background, the latter ones are colored blue.

Particle	Decay channel
J/ψ	50% e^+e^- , 50% $\mu^+\mu^-$
η	$\pi^+\pi^-\pi^0$
D^0	$K^-\pi^+$
D^+	$K^-\pi^+\pi^+$
D^{*+}	50% $D^0\pi^+$, 50% $D^+\pi^0$
D^{*0}	$D^0\pi^0$
D_s^+	$\phi\pi^+$
ϕ	K^+K^-
Λ	$p\pi^-$
π^0	$\gamma\gamma$

Table 8: Standard decay channels for some particles

4.3 Fast Simulation

In order to get information about phase space (i.e. momentum-polar angle dependence) coverage of the different PID relevant subsystems maps of separation power have been generated. They are based on fast simulations of single track events, i.e. the particles properties are modified with an effective parameterization of detectors responses and the PID information is estimated and attached to the resulting particle candidate. Since no microscopic simulation is performed and no exact geometry information is taken into account, the accuracy of this approach is limited, the computation time on the other hand is orders of magnitude shorter offering the possibility to do studies with higher statistics.

⁴Signal channels with background reactions comprising the same final state can only be identified due to different kinematic behaviour, which goes beyond the capabilities of PID

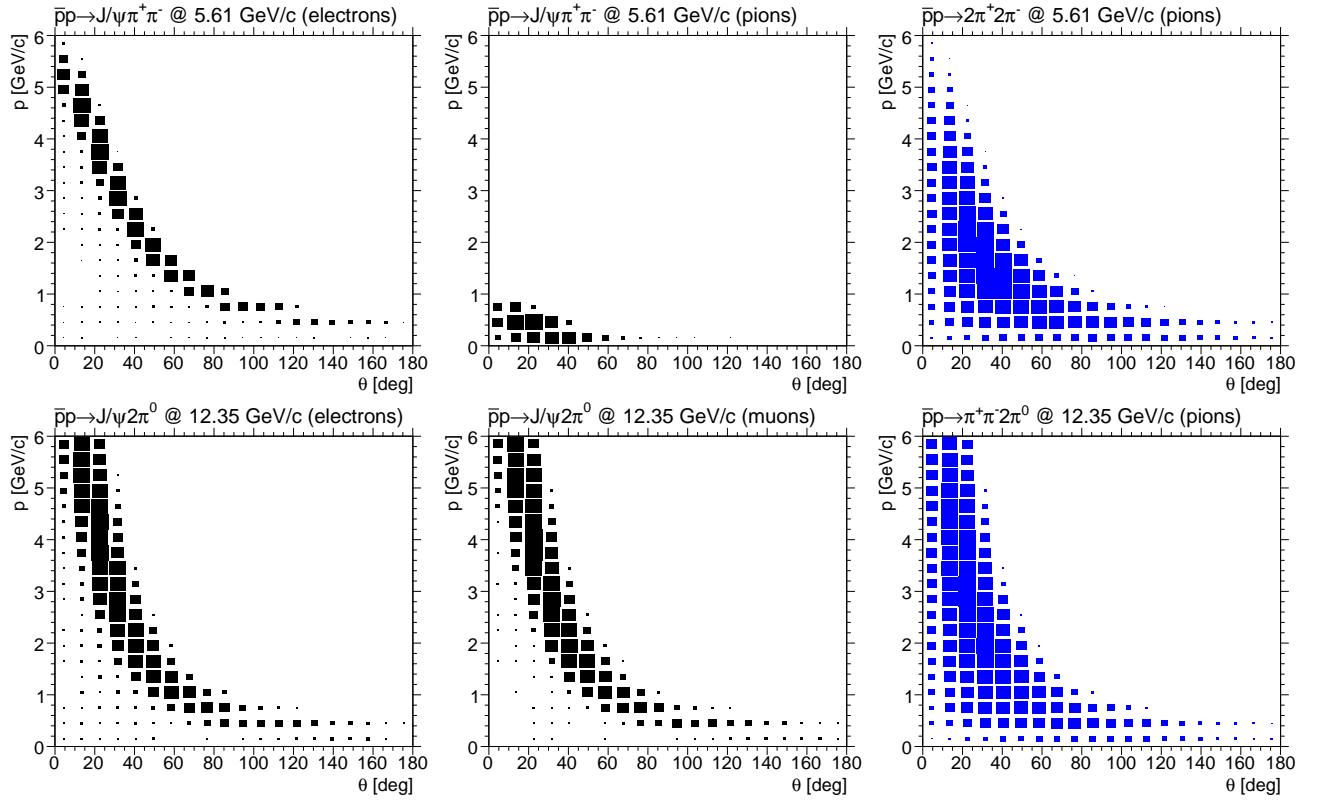


Figure 52: $\bar{p}p \rightarrow J/\psi \pi^+ \pi^-$ @ 5.609 GeV/c (top), $\bar{p}p \rightarrow J/\psi 2\pi^0$ @ 12.3485 GeV/c (bottom)

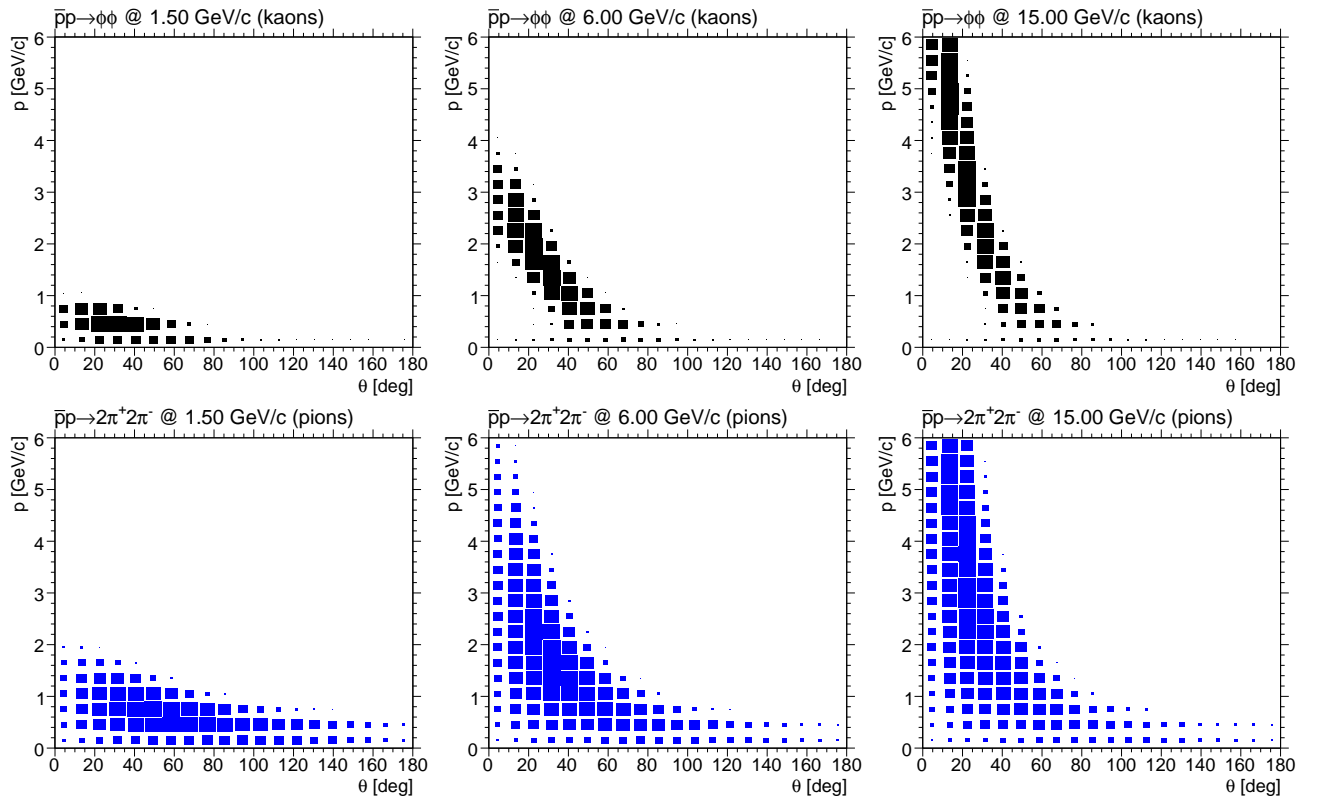
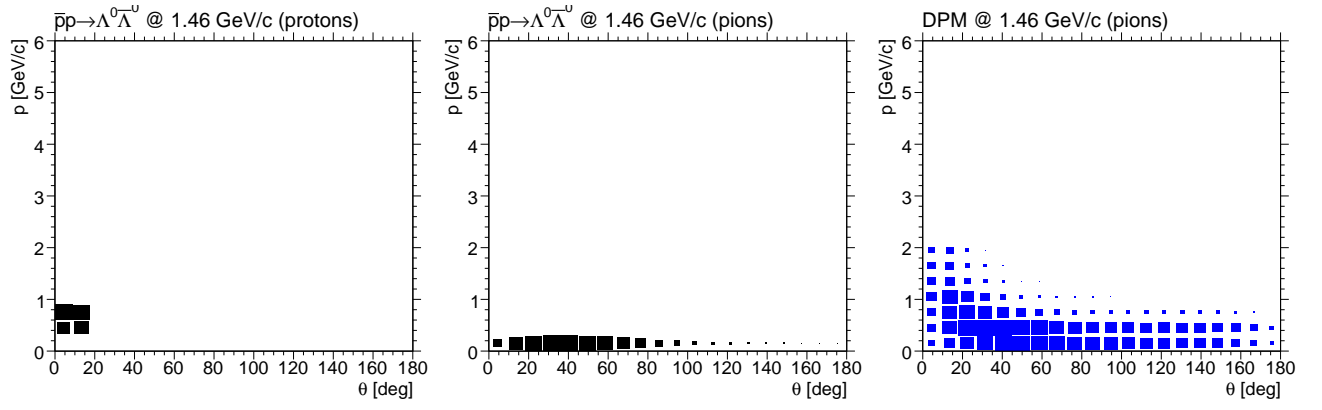
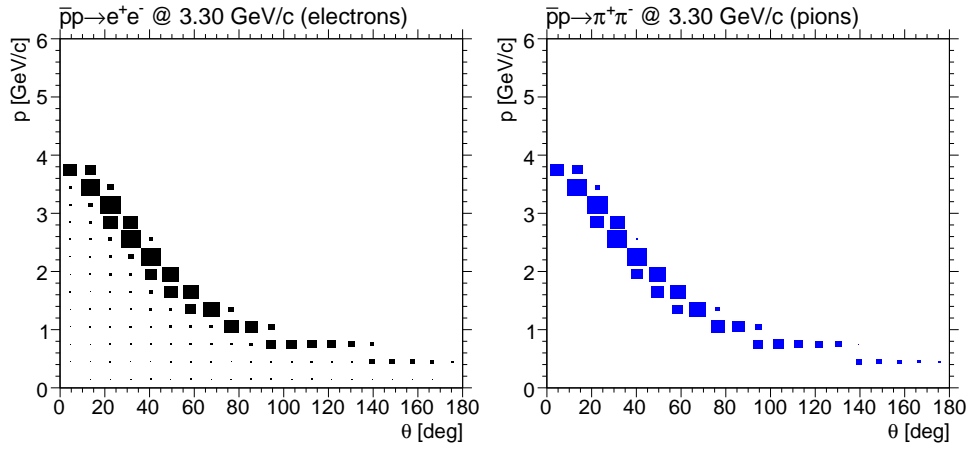
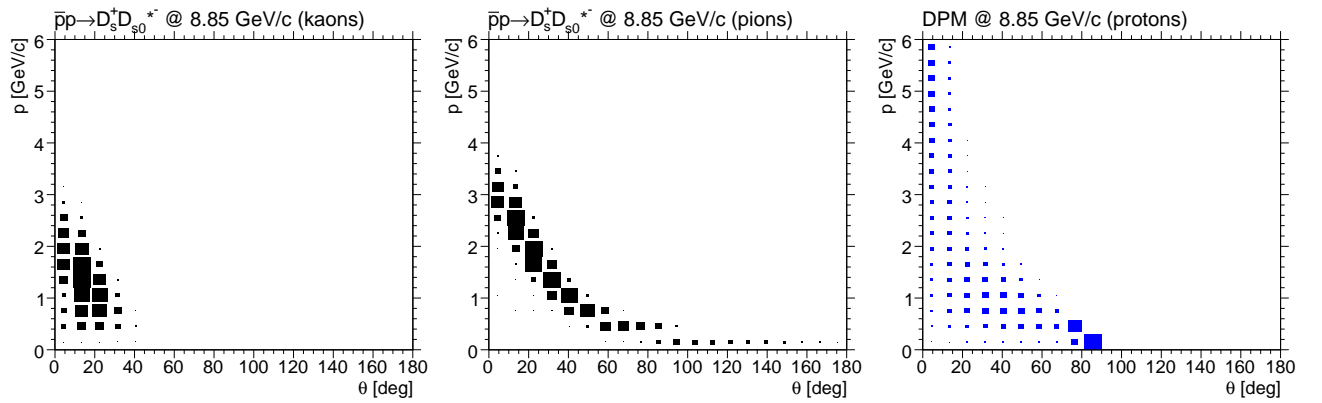


Figure 53: $\bar{p}p \rightarrow \phi \phi$ @ 1.5, 6.0, 15.0 GeV/c

Figure 54: $\bar{p}p \rightarrow \Lambda^0 \bar{\Lambda}^0$ @ 1.4601 GeV/cFigure 55: $\bar{p}p \rightarrow e^+ e^-$ @ 3.30 GeV/cFigure 56: $\bar{p}p \rightarrow D_s^+ D_s^{*-}(2317)^-$ @ 8.847 GeV/c

Signal	Background	$p_{\bar{p}}$ [GeV/c]	Fig.
$J/\psi 2\pi^0$	$\pi^+\pi^-2\pi^0$	5.609 / 6.232 / 8.682 10.295 / 12.349	52
$J/\psi \pi^+\pi^-$	$2\pi^+2\pi^-$	5.609 / 6.232 / 6.988 8.682 / 10.295 / 12.349	-
$J/\psi \eta$	$2\pi^+2\pi^-\pi^0$	6.990 / 8.7	-
	$2\pi^+2\pi^-$	6.080 / 6.990 / 8.7	-
	$3\pi^+3\pi^-$	6.080 / 6.990 / 8.7	-
$\phi\phi$	$2\pi^+2\pi^-$	1.5 / 6.0 / 12.0 / 15.0	53
	$3\pi^+3\pi^-$	1.5 / 6.0 / 12.0 / 15.0	-
$\Lambda^0\bar{\Lambda}^0$	$\Sigma^0\bar{\Sigma}^0$	1.914 / 3.101 / 6.0	54
	DPM	1.460 / 8.0 / 10.0	-
$\Omega^-\bar{\Omega}^+$	DPM	4.954	
$\Lambda_c^+\Lambda_c^-$	D^+D^-	10.187	
	DPM	10.187	
e^+e^-	$\pi^+\pi^-$	1.7 / 3.3 / 7.9 / 10.9 / 15.0	55
$D_s^+D_{s0}^*(2317)^-$	DPM	8.847	56
	$3\pi^+3\pi^-\pi^0$	8.847	-
$D_s^+D_s^-\gamma$	$3\pi^+3\pi^-$	8.847	-
	DPM	7.361 / 7.746 / 8.0 / 12.0 / 15.0	-
$D^{*0}\bar{D}^{*0}\gamma$	DPM	7.746 / 8.0 / 12.0 / 15.0	-
$D^{*+}D^{*-}\gamma$	DPM	7.746 / 8.0 / 12.0 / 15.0	-
$D^0\bar{D}^0\gamma$	DPM	6.488 / 8.0 / 12.0 / 15.0	-
$D^+D^-\gamma$	DPM	6.488 / 8.0 / 12.0 / 15.0	-

Table 9: Table of Phase Space Channels

4.3.1 General Technique

In contrast to microscopic simulations using software systems like Geant or Fluka the Fast Simulation is based on acceptance filtering and effective parameterization of all observables of the particular subsystems. Underlying assumption is that the detector system will be able to reconstruct the true particles properties like momentum, direction, energy, charge and particle identification information with uncertainties which are basically uncorrelated and can be described reasonable by parametric models. That could, as simple example, be a gaussian uncertainty for momentum reconstruction with $\delta p/p = \sigma_p = 2\%$, which will be used to modify the true (i.e. generated) track parameters accordingly. Additionally a simple geometric acceptance requirement will decide whether a track has been detected by a particular detector component or not.

There is a lot of freedom for the implementation of the subsystems, but a minimalistic detector description comprises

- Sensitivity information: Detects charged or neutral particles or both?

- Polar angle coverage: $\theta_{\min} < \theta < \theta_{\max}$
- Gaussian resolution of observables: $\sigma_1, \dots, \sigma_n$

In order to apply these simulation scheme for every trackable particle coming from the event generator the following procedure is processed:

1. For all detectors D_j , $1 < j < m$
 - In case D_j detects the particle, collect resolution information for all measurable quantities.
2. When no detector detected the track, skip it.
3. Merge all resolution information; when e.g. the particle has been detected by n devices capable of measuring momentum p with resolutions $\sigma_{p,1}, \dots, \sigma_{p,n}$, the total resolution is

$$\sigma_p = \left(\sum_{i=1}^n \frac{1}{\sigma_{p,i}^2} \right)^{-\frac{1}{2}}$$

4. Modify the according quantities x of the original track in the way $x' = x + \delta x$, with δx randomly chosen from gaussian distribution $G(\mu = 0, \sigma_x)$
5. Create PID information according to the particles properties and attach to the particle; add particle to the track list
6. (Optional) Create secondary particles related to particles properties and add to the track list

With the so prepared track list analysis can be performed. The interface for doing that is exactly the same as the one for fully simulated events.

Since this document is focussing on PID the relevant features will be describe in more detail in the following chapters. This will be done effect- or observable-wise instead of detector-wise, since the observed quantities

- specific energy loss dE/dx (MVD, TPC, STT)
- Cherenkov angle θ_C (Barrel DIRC, Disc DIRC, RICH)
- reconstructed squared mass m^2 (TOF)
- EMC related measurements like E_{cluster}/p or Zernike momenta
- signals from Muon Chambers

govern the PID quality and performance and thus are a better ordering criterion. Unfortunately the latter two informations from electromagnetic calorimetry and the muon detectors are not implemented in the Fast Simulation for the time being.

4.3.2 Tracking Detectors

Although not of direct impact to the field of PID the process of tracking delivers vital information for many of the PID relevant systems. Most of these like e.g. the Time-of-flight (TOF) system or Cherenkov devices (DIRCs and RICH) do not allow for performing a stand alone position measurement, thus their information have to be linked to tracks reconstructed by tracking devices. In addition for the purpose of evaluating PID likelihood functions one usually needs to compute expected values for observables like the Cherenkov angle θ_C or energy loss dE/dx which will be computed for the reconstructed momentum value of the track. This certainly will differ from the true momentum value and therefore track reconstruction accuracy has important impact on likelihood based classification methods.

The approach for the reconstruction of momenta in the Fast Simulation nevertheless is a very simple one assuming a global momentum resolution $\delta p/p$ for the track reconstruction, since due to technical reasons the particular detector components cannot exchange information. This implies that the tracking devices are not able to feed their information into the PID systems.

4.3.3 Energy Loss Parameterization

The computation of the specific energy loss is based on the Bethe-Bloch formula

$$-\frac{dE}{dx} = \kappa \cdot \frac{Z}{A} \cdot \frac{e^2}{\beta^2} \cdot \left[\ln \left(\frac{2m_e \beta^2 \gamma^2 T_{\max}}{I^2} \right) - 2\beta^2 - \delta \right] \quad \left[\frac{\text{MeV} \cdot \text{cm}}{\text{g}} \right] \quad (19)$$

which very precisely takes into account the processes of charged particles interacting with matter. The formula and detailed information about parameter meanings in this term can be found in [22].

The expression looks quite complicated but can be evaluated straight forward with momentum p and mass m given as input. Additionally one has to substitute a lot of other, material related constants. Since we are not interested in the absolute energy loss but only in relative losses for different particle species it is not crucial to have very precise knowledge about the fixed parameters.

In order to generate a simulated detector response for detectors capable of measuring dE/dx a gaussian resolution $\sigma_{dE/dx}$ has been set for each of them. The simulated measured $(dE/dx)_{\text{sim}}$ value thus has been simply computed with formula (19) to

$$\left(\frac{dE}{dx} \right)_{\text{sim}} = \left(\frac{dE}{dx} \right) + \delta \left(\frac{dE}{dx} \right) \quad (20)$$

with randomly chosen value $\delta(dE/dx)$ from a gaussian distribution $G(\mu = 0, \sigma_{dE/dx})$.

4.3.4 Cherenkov Angle Parameterization

Basic theoretical information about the origin of Cherenkov radiation can be found elsewhere and will not be discuss here. The Cherenkov angle defined as the opening angle of the cone of radiation relative to the direction of the incident charged particles momenta in medium with refractive index n is given by the expression

$$\theta_C = \arccos \left(\frac{1}{\beta \cdot n} \right) \quad (21)$$

with $\beta = p \cdot c/E$ being the velocity of the particle. Obviously computation of the expected Cherenkov angle for any given particle detected by the specific detector is straight forward. Key ingredient of the parameterization of the detector response is the resolution estimation. In case of DIRC detectors experience from the working device in the BaBar experiment tells us that the overall reconstruction resolution of the Cherenkov angle can be based on a single photon resolution $\sigma_{\text{s.phot.}} \approx 10 \text{ mrad}$. Responsible for the overall resolution then exclusively is the number of detected Cherenkov photons N through

$$\sigma_{\text{tot}} = \frac{\sigma_{\text{s.phot.}}}{\sqrt{N}},$$

which is simple count statistics. This number N has to be estimated and depends on

- the number of generated photons

$$N_0 = 2\pi \cdot \alpha \cdot L \left(\frac{1}{\lambda_{\min}} - \frac{1}{\lambda_{\max}} \right) \cdot \sin^2 \theta_C = 2\pi \cdot \alpha \cdot L \left(\frac{1}{\lambda_{\min}} - \frac{1}{\lambda_{\max}} \right) \cdot \left(1 - \frac{m^2 + p^2}{p^2 \cdot n^2} \right) \quad (22)$$

with parameters

- fine structure constant α
- trajectory length L in the radiator material
- mass and momentum m and p of the incident track
- wave length region λ_{\min} and λ_{\max} where the photon detector is sensitive and
- refraction index n
- the trapping fraction r_{trap} which is the fraction of the photons kept in the radiator/lightguide due to total reflection and
- the detection efficiency ϵ of the photon detector, e.g. a photo multiplier tube (PMT)

In order to derive the path length L in the material one has to distinguish between the different Cherenkov devices.

In case of the **Barrel DIRC** on first of all has to compute the curvature due to the motion of a charged particle in a magnetic solinoidal field $B = B_z$. The radius r of the circular shape in (x, y) projection is given by

$$r = \frac{p_t}{q \cdot B} = \frac{3.3356 \cdot p_t [\text{GeV}/c]}{B [\text{T}]} \quad (23)$$

for a particle with charge $q = \pm e$ and transverse momentum $p_t = p \cdot \sin \theta$. Based on this one can calculate the entering angle ψ in ϕ direction to

$$\psi = \arccos \frac{r_B}{2 \cdot r} \quad (24)$$

with r_B being the radius of the DIRC Barrel i.e. the distance between the bars and the beam line. Here it is obvious that particles with $2 \cdot r < r_B$ will not hit the detector at all defining a minimum transverse momentum $p_{t,\min}$. The path length after some geometrical considerations then computes to

$$L \approx d_{\text{bar}} \cdot \sqrt{\frac{1}{\sin^2 \theta} + \frac{1}{\tan^2 \psi}} \quad (25)$$

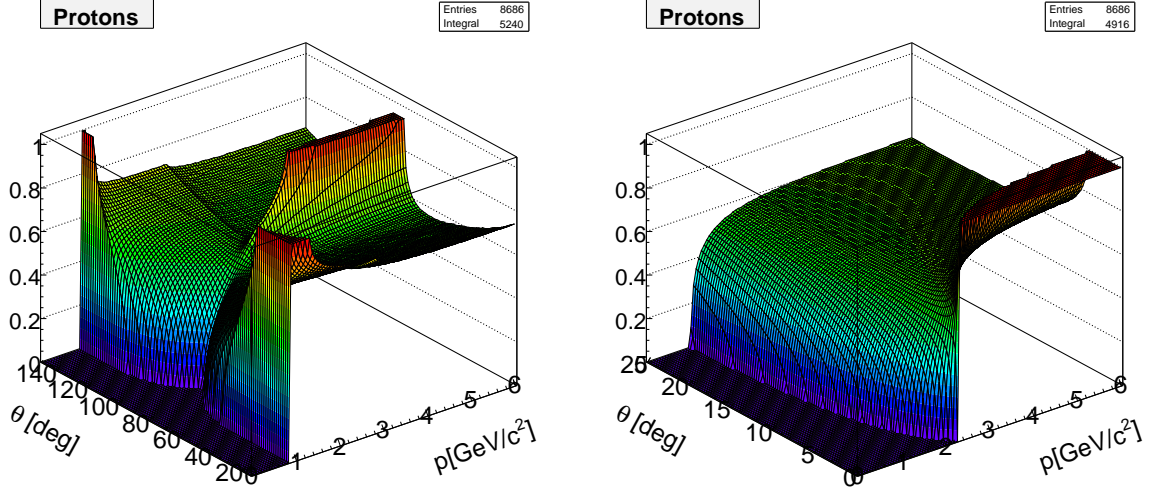


Figure 57: 2-dimensional picture of the trapping fraction for protons in the Barrel DIRC (left) and the Disc DIRC as a function of momentum p and dip angle θ .

where d_{bar} is the thickness of the radiator bars and θ the dip angle of the helix of the track. The expression is an approximation because curvature within the bar has been neglected. This leads to significant wrong values for particles with $2 \cdot r \approx r_B$.

For the **Disc DIRC** and the **RICH** computing the radiator path length is much simpler. Here L only depends on the dip angle and the radiator thickness d_{rad} resulting in

$$L = \frac{d_{\text{rad}}}{\cos \theta}. \quad (26)$$

Also here no curvature within the radiators has been taken into account. This anyway would lead to more complicated estimates since angular changes along the radiator path results in systematic worsening of the Cherenkov angle which is neglected completely.

Finally we still need the trapping fraction r_{trap} to determine the number of detected photons. There is no known analytic expression to compute this, thus 2 dimensional lookup tables $r_{\text{trap}}(\theta, p)$ for every particle species have been prepared. Figure 57 shows as an example the trapping fraction in the Barrel DIRC bars for muons and protons as a function of momentum p and dip angle θ .

With the path length L one can evaluate expression (22) so that the detected number of photons can be estimated to

$$N = N'_0 \cdot \epsilon \cdot r_{\text{trap}} \quad (27)$$

where the N'_0 is randomly generated from Poisson distribution with input value $\lambda = N_0$. This directly leads to the expected resolution σ_{tot} which is taken as the absolute uncertainty of the measurement of the Cherenkov angle. The simulated measured Cherenkov angle thus has been computed with formula (21) to

$$\theta_{C,\text{sim}} = \theta_C + \delta\theta_C \quad (28)$$

with randomly chosen value $\delta\theta_C$ from a gaussian distribution $G(\mu = 0, \sigma_{\text{tot}})$.

4.3.5 Time Of Flight Parameterization

From the geometrical point of view the calculation of the expected time of flight of a particle has similarities to the considerations done in 4.3.4 for the Barrel DIRC, since the TOF detector has also cylindrical shape. This requires also the particles with curvatures given by equation (23) to have a minimum transverse momentum p_t to reach the detector and produce a signal.

In order to compute the time of flight $t_{\text{TOF}} = s/v$ one in principal only needs the traveled distance s and the velocity v of the particle. While the latter one is simple to get by via the particles $\beta = p \cdot c/E$, the distance is not so easy to calculated due to the tracks curvature in the magnetic field. Nevertheless the calculation can be simplified exploiting the fact that the particles motion in z direction is independent of that one in the (x, y) plane. Therefore t can also be calculated via the ratio of the travelled angle Φ and the angular velocity ω

$$t_{\text{TOF}} = \frac{\Phi}{\omega} = \frac{1}{\omega} \cdot 2 \arcsin \frac{r_B}{2r} \quad (29)$$

with the determination of Φ illustrated in fig. 58. The angular velocity in the projected plane is given by

$$\omega = \frac{B}{3.3356 \cdot E} \quad (30)$$

for a magnetic field B [T] and E [GeV]. With these expressions one can derive the true expected time of flight. What now has to be simulated is the expected accuracy of the measurement achieved by the detector. This depends on the time resolution on one hand and on the resolution connected to track reconstruction on the other hand since the transverse momentum $p_t = p \cdot \sin(\theta)$ is needed to compute the flight length. Concerning the total time resolution it is assumed to have a start and a stop detector with uncertainties of $\delta t \approx 100$ ps each resulting in a total of $\sigma_t \approx \sqrt{2} \cdot 100$ ps = 141 ps⁵. For the momentum resolution only a relative uncertainty $\sigma_p = \delta p/p \approx 2\%$ for the reconstructed absolute value has been taken into account neglecting uncertainties of angular measurements.

This results in measured values

$$t'_{\text{TOF}} = t_{\text{TOF}} + \delta t \quad (31)$$

$$p' = p \cdot (1 + \delta p) \quad (32)$$

with gaussian distributed deviations δt and δp according to $G(\mu = 0, \sigma_t)$ and $G(\mu = 0, \sigma_p)$. The primes denote from now the 'measured' or 'simulated' quantities. Now one basically has to reverse the process from above to get the simulated reconstructed value for the energy E needed to compute the squared mass

$$m'^2 = E'^2 - p'^2 \quad (33)$$

which acts as the observable of the TOF detector. Starting point is eq. (30) which forms to $E' = B/(3.3356 \cdot \omega')$ etc. The resulting term depending only on the quantities t'_{TOF} , p' and θ looks like

$$m'^2 = \left(\frac{B \cdot t'_{\text{TOF}}}{2 \cdot 3.3356 \cdot \arcsin \left(\frac{r_B}{2 \cdot 3.3356 \cdot p' \sin(\theta)} \right)} \right)^2 - p'^2 \quad (34)$$

⁵At the moment it is planned to run without a start detector, which leads to a improved time resolution but requires to operate the TOF with relative timing.

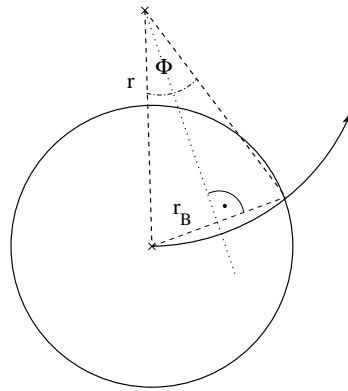


Figure 58: Projection of particle trajectory to (x, y) plane in order to determine Φ .

4.3.6 Parameter Settings

Tab. 10 presents the complete set of relevant parameters which were used in the Fast Simulation to extract most of the results presented in this note, in particular in section 5.1.

Meaning	Quantifier	Value
Global		
Magnetic Field Strength	$B = B_z$	2 T
Relative Momentum Resolution	σ_p/p	1 %
Micro Vertex Detector (MVD)		
Angular Acceptance	$[\theta_{\min}; \theta_{\max}]$	$[0.0^\circ; 180.0^\circ]$
Relative dE/dx Resolution	$\sigma_{dE/dx}$	22 %
Straw Tube Tracker (STT)		
Angular Acceptance	$[\theta_{\min}; \theta_{\max}]$	$[7.765^\circ; 159.44^\circ]$
Relative dE/dx Resolution	$\sigma_{dE/dx}$	20 %
Inner Radius	R_I	15 cm
Time Projection Chamber (TPC)		
Angular Acceptance	$[\theta_{\min}; \theta_{\max}]$	$[7.765^\circ; 159.44^\circ]$
Relative dE/dx Resolution	$\sigma_{dE/dx}$	8 %
Inner Radius	R_I	15 cm
Barrel DIRC		
Angular Acceptance	$[\theta_{\min}; \theta_{\max}]$	$[22.0^\circ; 140.0^\circ]$
Inner Radius	R_I	48 cm
Single Photon Resolution	σ_{ph}	10 mrad
Thickness of Slab	d_S	1.7 cm
Refractive Index of Quarz	n_Q	1.472
Total Photon Detector Efficiency	ϵ_{PD}	7.5 %
Disc DIRC		
Angular Acceptance	$[\theta_{\min}; \theta_{\max}]$	$[5.0^\circ; 22.0^\circ]$
Single Photon Resolution	σ_{ph}	10 mrad
Thickness of Disc	d_D	1.7 cm
Refractive Index of Quarz	n_Q	1.472
Total Photon Detector Efficiency	ϵ_{PD}	7.5 %
Ring Image Cherenkov Detector (RICH)		
Angular Acceptance	θ_{\min}	0.0°
	$\alpha_{\max} \text{ (vert.)}$	5.0°
	$\alpha_{\max} \text{ (hor.)}$	10.0°
Single Photon Resolution	σ_{ph}	10 mrad
Thickness of Radiator	d_D	1 m
Refractive Index of Radiator	n_R	1.05
Total Photon Detector Efficiency	ϵ_{PD}	7.5 %
Time of Flight system (TOF)		
Angular Acceptance	$[\theta_{\min}; \theta_{\max}]$	$[22.0^\circ; 140.0^\circ]$
Inner Radius	R_I	38 cm
Total Time Resolution	σ_t	141 ps

Table 10: Parameter Settings used for the Fast Simulation

5 Evaluation

5.1 Maps of Separation

In order to evaluate the PID performance applied to specific physics channels the information about

1. kinematic distribution of signal channel
2. kinematic distribution of possible background
3. separation power/mis identification level in phase space

have been combined in the way, that signals distributions for every particle species have been projected on the according map of separation power with either STT or TPC option. Since the implementation of the TOF detector is still under investigation at the time of writing, the studies for both options also have been performed without the information of the TOF system.

Background has been taken into account by punching the according separation map with its distribution leaving only regions colored where in fact background particles appear.

For instance to determine the PID quality for kaons from $\bar{p}p \rightarrow D^+D^-\gamma$ reactions at a particular energy against pions from DPM background, the phase space histogram of kaons from the signal channel has been projected on the $\pi^\pm - K^\pm$ separation map which has been punched with the distribution of pions from DPM events at the same total energy.

This procedure gives access to the information how good a particle type for a specific signal channel can be identified. In particular it offers the possibility to identify regions with insufficient PID quality.

As a quantitative measure for the goodness or badness of a certain detector performance the average separation capability has been determined. Since the value of separation power itself is less sensitive to smaller differences than the corresponding value for the average mis-identification fraction f_{mis} (see tab. 7), the latter has been computed over the whole phase space where overlap between signal and background distributions appear.

For scenarios with $f_{mis} > 0.1\%$ the information has been summarized in tables 11 - 13 for the four different detector setups described above. Listed is the momentum of the antiproton beam $p_{\bar{p}}$, the signal channel, the particular particle species of signal and background, the minimum average separation power of the four setups, the maximum average mis-identification level $f_{mis,max}$ and the relative ratio $f_{mis,i}/f_{mis,max}$ for the four detector combinations. There are cases where the ratios are unexpectedly better for setups without additional TOF information; the reason is, that the averages are determined statistically which leads sometimes to fluctuations. Nevertheless the order of magnitude is reflected correctly.

Figs. 59 – 61 present the corresponding plots for some selected channels. Each column shows the results for one particular channel and the four different detector setups in the same order from top to bottom as given in the list. In tabs. 11 and 13 those channels are marked with a bullet (•) in the PID column.

$p_{\bar{p}}$ [GeV/c]	Signal	PID	min σ	mis[%]	STT	STT+TOF	TPC	TPC+TOF
1.460	$\Lambda^0 \bar{\Lambda}^0$	$\pi - e \bullet$	3.0	7.0	1.0	0.8	0.7	0.6
		$\pi - K$	4.9	0.7	1.0	0.9	0.8	0.8
		$p - e$	4.8	0.8	0.8	1.0	0.9	1.0
		$p - \pi$	3.6	3.5	1.0	1.0	0.7	0.7
		$p - K$	3.3	5.0	1.0	1.0	0.6	0.6
1.500	$\phi\phi$	$K - \pi$	3.6	3.6	1.0	0.8	0.5	0.5
		$K - \pi$	3.6	3.6	1.0	0.8	0.5	0.5
1.700	e^+e^-	$e - \pi$	5.3	0.4	1.0	1.0	0.7	0.7
3.300	e^+e^-	$e - \pi$	5.2	0.4	1.0	1.0	0.8	0.8
4.954	$\Omega^- \bar{\Omega}^+$	$\pi - K$	3.8	2.9	1.0	1.0	0.5	0.5
		$\pi - p$	4.1	2.0	1.0	1.0	1.0	1.0
		$K - \pi$	2.8	8.3	1.0	1.0	0.7	0.7
		$K - p$	2.6	9.2	1.0	1.0	0.5	0.4
		$p - \pi$	1.5	22.3	1.0	1.0	0.9	0.9
		$p - K \bullet$	1.7	19.8	1.0	1.0	0.9	0.9
5.609	$J/\psi 2\pi^0$ $J/\psi \pi^+\pi^-$	$e - \pi$	5.2	0.5	1.0	1.0	0.9	0.8
		$e - \pi$	5.2	0.5	1.0	1.0	0.9	0.9
6.000	$\phi\phi$	$K - \pi \bullet$	5.5	0.3	1.0	0.3	0.2	0.1
		$K - \pi$	5.5	0.3	1.0	0.2	0.2	0.1
6.080	$J/\psi\eta$	$e - \pi$	5.2	0.4	1.0	0.9	0.9	0.8
		$e - \pi$	5.1	0.6	1.0	1.0	0.7	0.8
6.232	$J/\psi 2\pi^0$ $J/\psi \pi^+\pi^-$	$e - \pi$	5.1	0.5	1.0	0.9	1.0	0.8
		$e - \pi$	5.1	0.5	1.0	1.0	0.9	0.8
6.488	$D^0 \bar{D}^0 \gamma$	$\pi - K$	6.0	0.1	1.0	0.2	0.1	0.0
		$\pi - p$	4.8	0.8	1.0	0.2	0.4	0.3
		$K - \pi$	5.4	0.3	1.0	0.2	0.2	0.1
		$K - p \bullet$	4.8	0.8	1.0	0.1	0.1	0.1
	$D^+ D^- \gamma$	$\pi - e$	5.2	0.5	1.0	0.7	0.6	0.5
		$\pi - K$	4.9	0.8	1.0	0.7	0.5	0.5
		$\pi - p$	3.8	2.8	1.0	0.8	0.6	0.6
		$K - e$	6.1	0.1	1.0	0.7	0.7	0.8
		$K - \pi$	4.8	0.9	1.0	0.8	0.6	0.7
		$K - p$	3.6	3.6	1.0	0.8	0.6	0.6
6.988	$J/\psi \pi^+\pi^-$	$e - \pi$	5.2	0.5	1.0	1.0	0.8	0.9
6.990	$J/\psi\eta$	$e - \pi$	5.2	0.5	1.0	1.0	0.8	0.8
		$e - \pi$	5.2	0.4	1.0	1.0	0.8	0.9
		$e - \pi$	5.2	0.5	1.0	0.9	0.9	0.8
7.314	$D_s^+ D_s^- \gamma$	$\pi - K$	4.4	1.3	1.0	0.9	0.6	0.5
		$\pi - p$	4.1	2.1	1.0	0.8	0.7	0.7
		$K - \pi$	3.9	2.7	1.0	1.0	0.8	0.8
		$K - p$	3.0	6.4	1.0	0.9	0.6	0.6
7.746	$D^{*+} D^{*-} \gamma$	$\pi - K$	4.3	1.5	1.0	0.9	0.7	0.7
		$\pi - p$	4.4	1.3	1.0	0.8	0.6	0.6
		$K - \pi$	5.1	0.5	1.0	0.6	0.4	0.4
		$K - p$	4.2	1.7	1.0	0.7	0.5	0.4
	$D^{*0} \bar{D}^{*0} \gamma$	$\pi - K \bullet$	5.6	0.3	1.0	0.3	0.1	0.0

Table 11:

$p_{\bar{p}}$ [GeV/c]	Signal	PID	min σ	mis[%]	STT	STT+TOF	TPC	TPC+TOF
7.746	$D^{*+}D^{*-}\gamma$	$\pi - p$	5.1	0.5	1.0	0.1	0.1	0.0
		$K - \pi$	5.6	0.3	1.0	0.2	0.2	0.1
		$K - p$	4.8	0.8	1.0	0.1	0.1	0.0
		$D_s^+ D_s^- \gamma$	4.3	1.6	1.0	0.8	0.5	0.6
		$\pi - p$	4.1	2.1	1.0	0.8	0.7	0.7
		$K - \pi$	3.9	2.5	1.0	1.0	0.8	0.9
		$K - p$	3.0	6.3	1.0	0.9	0.6	0.6
7.900	e^+e^-	$e - \pi$	5.4	0.3	1.0	1.0	0.8	0.7
8.000	$\Lambda^0 \bar{\Lambda}^0$	$\pi - K$	3.7	3.1	1.0	0.9	0.6	0.7
		$\pi - p$	3.4	4.5	1.0	0.9	0.6	0.6
		$p - \pi$	5.6	0.3	1.0	0.1	0.1	0.0
		$p - K$	5.4	0.3	1.0	0.1	0.1	0.0
		$D^{*0} \bar{D}^{*0} \gamma$	5.4	0.4	1.0	0.2	0.1	0.0
		$\pi - p$	5.1	0.5	1.0	0.2	0.1	0.1
		$K - \pi$	5.6	0.3	1.0	0.2	0.1	0.1
	$D^+ D^- \gamma$	$K - p$	4.8	0.8	1.0	0.1	0.1	0.1
		$\pi - K$	4.5	1.2	1.0	0.7	0.5	0.5
		$\pi - p$	3.8	2.8	1.0	0.8	0.7	0.7
		$K - \pi$	4.7	0.9	1.0	0.8	0.6	0.6
		$K - p$	3.6	3.5	1.0	0.8	0.6	0.6
	$D^0 \bar{D}^0 \gamma$	$\pi - K$	5.4	0.4	1.0	0.2	0.1	0.0
		$\pi - p$	4.8	0.8	1.0	0.4	0.4	0.4
		$K - \pi$	5.5	0.3	1.0	0.4	0.3	0.2
		$K - p$	4.6	1.0	1.0	0.3	0.3	0.3
		$\pi - K$	4.3	1.6	1.0	0.8	0.6	0.5
	$D_s^+ D_s^- \gamma$	$\pi - p$	4.1	2.0	1.0	0.8	0.6	0.7
		$K - \pi$	3.9	2.6	1.0	0.9	0.8	0.8
		$K - p$	3.1	6.3	1.0	0.9	0.7	0.7
		$\pi - K$	4.1	2.1	1.0	1.0	0.8	0.8
		$\pi - p$	4.2	1.9	1.0	0.9	0.7	0.8
		$K - \pi$	5.2	0.5	1.0	0.5	0.5	0.6
		$K - p$	4.2	1.7	1.0	0.6	0.4	0.5
	$D^{*+} D^{*-} \gamma$	$\pi - K$	4.1	2.1	1.0	1.0	0.8	0.8
		$\pi - p$	4.2	1.9	1.0	0.9	0.7	0.8
		$K - \pi$	5.2	0.5	1.0	0.5	0.5	0.6
		$K - p$	4.2	1.7	1.0	0.6	0.4	0.5
		$\pi - K$	4.1	2.1	1.0	1.0	0.8	0.8
		$\pi - p$	4.2	1.9	1.0	0.9	0.7	0.8
		$K - \pi$	5.2	0.5	1.0	0.5	0.5	0.6
		$K - p$	4.2	1.7	1.0	0.6	0.4	0.5
	$J/\psi \pi^+ \pi^-$	$e - \pi$	5.2	0.4	1.0	0.9	0.8	0.7
		$J/\psi 2\pi^0$	5.3	0.4	1.0	0.9	0.9	0.8
		$e - \pi$	5.3	0.4	1.0	0.9	0.9	0.8
	$J/\psi \eta$	$e - \pi$	5.2	0.5	1.0	0.8	0.8	0.7
		$e - \pi$	5.3	0.4	1.0	1.0	0.9	0.8
		$e - \pi$	5.3	0.4	1.0	1.0	0.8	0.7
	$D_s^+ D_{s0}^{*-} \gamma$	$\pi - K \bullet$	5.2	0.5	1.0	0.2	0.1	0.0
		$\pi - p$	4.5	1.2	1.0	0.6	0.6	0.6
		$K - \pi$	4.2	1.8	1.0	1.0	0.7	0.8
		$K - p$	2.8	7.8	1.0	1.0	0.7	0.7
		$K - \pi$	4.2	1.9	1.0	1.0	0.7	0.6
		$K - p$	4.2	1.9	1.0	1.0	0.7	0.6
		$K - \pi$	4.0	2.4	1.0	1.0	0.8	0.8
	$D_s^+ incl$	$K - \pi$	4.0	2.4	1.0	1.0	0.8	0.8
10.000	$\Lambda^0 \bar{\Lambda}^0$	$\pi - K$	3.8	2.7	1.0	1.0	0.7	0.7
		$\pi - p$	3.4	4.6	1.0	1.0	0.7	0.7
		$p - \pi$	5.5	0.3	1.0	0.1	0.1	0.1
		$p - K \bullet$	5.4	0.4	1.0	0.1	0.1	0.0

Table 12:

$p_{\bar{p}}$ [GeV/c]	Signal	PID	min σ	mis[%]	STT	STT+TOF	TPC	TPC+TOF
10.187	$\Lambda_c^+ \Lambda_c^-$	$\pi - K$	4.3	1.5	1.0	0.9	0.6	0.6
		$\pi - p$	3.6	3.7	1.0	0.9	0.7	0.8
		$K - \pi$	4.5	1.2	1.0	1.0	0.8	0.8
		$K - p$	3.4	4.6	1.0	0.9	0.7	0.7
		$p - \pi$	3.5	4.1	1.0	0.9	0.9	0.8
		$p - K$	3.5	4.1	1.0	1.0	0.8	0.8
		$\pi - K \bullet$	4.3	1.7	1.0	0.8	0.6	0.6
		$K - \pi$	4.5	1.2	1.0	1.0	0.8	0.8
		$p - \pi$	3.5	4.0	1.0	1.0	0.8	0.9
		$p - K$	3.5	4.1	1.0	0.9	0.8	0.8
12.000	$D^{*0} \bar{D}^{*0} \gamma$	$\pi - K$	5.6	0.3	1.0	0.3	0.2	0.1
		$\pi - p$	5.1	0.5	1.0	0.4	0.4	0.3
		$K - \pi$	5.1	0.5	1.0	0.8	0.6	0.5
		$K - p$	4.8	0.8	1.0	0.4	0.4	0.3
	$D_s^+ D_s^- \gamma$	$\pi - K$	4.4	1.4	1.0	0.9	0.6	0.7
		$\pi - p$	4.0	2.2	1.0	0.9	0.7	0.7
		$K - \pi$	4.2	1.7	1.0	1.0	0.8	0.8
		$K - p$	3.2	5.3	1.0	1.0	0.7	0.8
	$D^+ D^- \gamma$	$\pi - K$	4.6	1.0	1.0	0.7	0.6	0.6
		$\pi - p$	3.8	2.8	1.0	0.8	0.7	0.7
		$K - \pi$	4.7	0.9	1.0	1.0	0.7	0.7
		$K - p$	3.7	3.1	1.0	0.9	0.7	0.7
	$D^0 \bar{D}^0 \gamma$	$\pi - K$	5.7	0.2	1.0	0.3	0.2	0.2
		$\pi - p$	5.0	0.6	1.0	0.6	0.5	0.4
		$K - \pi$	5.0	0.6	1.0	0.8	0.6	0.5
		$K - p$	4.8	0.8	1.0	0.5	0.4	0.3
	$D^{*+} D^{*-} \gamma$	$\pi - K$	3.7	3.1	1.0	1.0	0.7	0.7
		$\pi - p$	4.4	1.4	1.0	0.8	0.7	0.7
		$K - \pi$	5.0	0.6	1.0	0.9	0.7	0.7
		$K - p$	4.3	1.6	1.0	0.7	0.7	0.5
	$\phi \phi$	$K - \pi$	4.8	0.8	1.0	0.8	0.6	0.6
15.000	$D^+ D^- \gamma$	$\pi - e$	5.4	0.3	1.0	0.8	0.7	0.6
		$\pi - K$	4.8	0.9	1.0	0.8	0.5	0.6
		$\pi - p$	3.9	2.5	1.0	0.9	0.7	0.7
		$K - \pi$	4.7	0.9	1.0	1.0	0.7	0.8
	$e^+ e^-$	$e - \pi$	5.5	0.3	1.0	1.0	0.8	0.9
		$\pi - e$	4.5	1.3	1.0	0.9	1.0	0.9
		$\pi - K$	3.6	3.4	1.0	1.0	0.7	0.7
		$\pi - p$	4.2	1.7	1.0	0.9	0.7	0.8
	$D^{*+} D^{*-} \gamma$	$K - p$	4.3	1.6	1.0	0.7	0.5	0.6
		$\pi - e$	6.2	0.1	1.0	0.7	0.6	0.4
		$\pi - K$	6.0	0.1	1.0	0.4	0.3	0.3
		$K - \pi$	5.2	0.5	1.0	0.9	0.6	0.6
	$D^{*0} \bar{D}^{*0} \gamma$	$K - p$	4.7	0.9	1.0	0.6	0.4	0.4
		$K - \pi$	4.4	1.4	1.0	0.9	0.7	0.7
		$\pi - e$	5.2	0.4	1.0	0.8	0.8	0.6
		$\pi - K$	4.5	1.2	1.0	0.9	0.6	0.7
	$\phi \phi$	$K - \pi$	4.4	1.4	1.0	0.9	0.8	0.8
		$K - p$	3.4	4.6	1.0	1.0	0.8	0.8
		$\pi - K$	6.0	0.1	1.0	0.4	0.3	0.3
		$K - p \bullet$	4.7	1.0	1.0	0.7	0.4	0.5

Table 13:

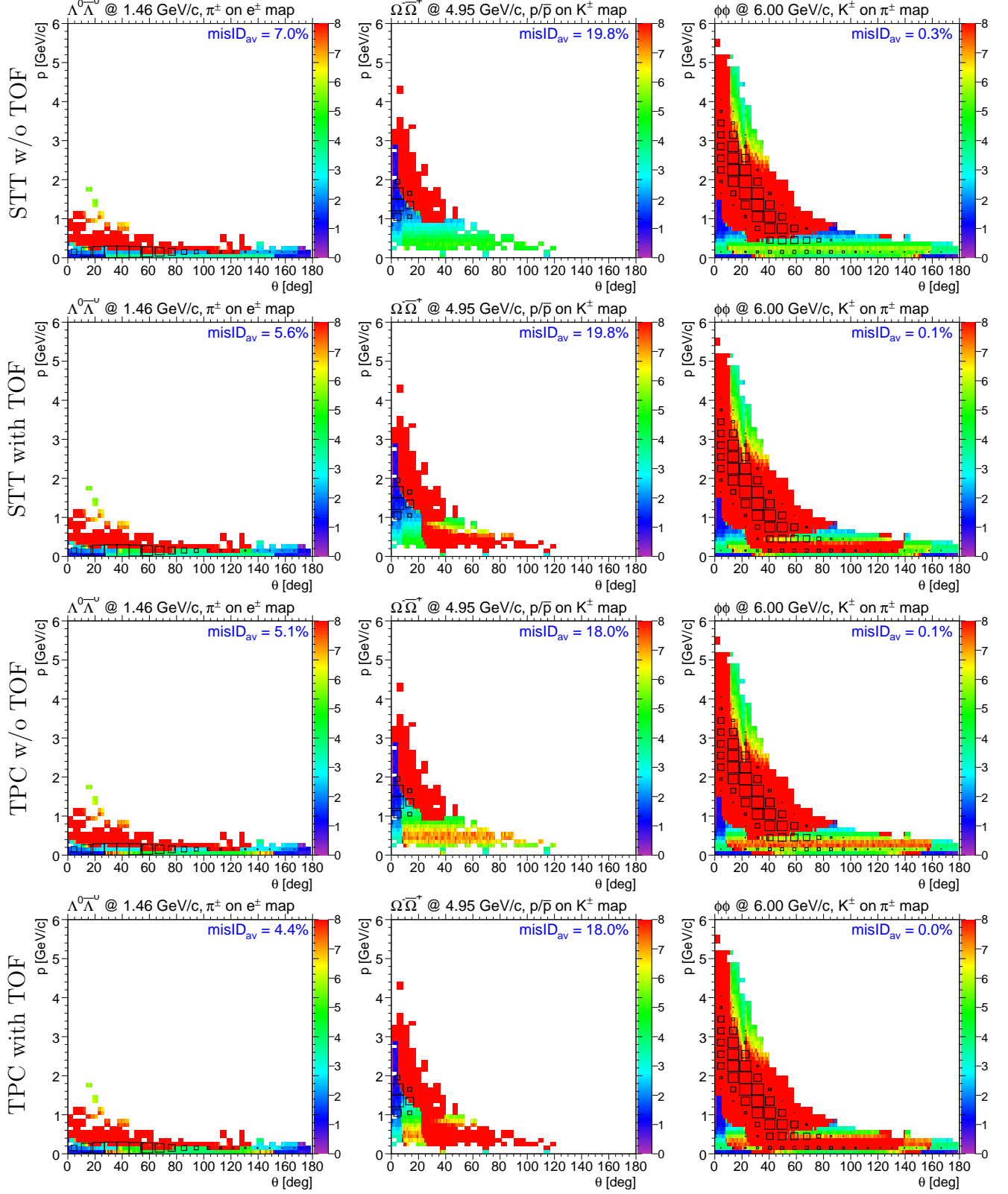


Figure 59: Projection of kinematic distributions on separation maps (1).

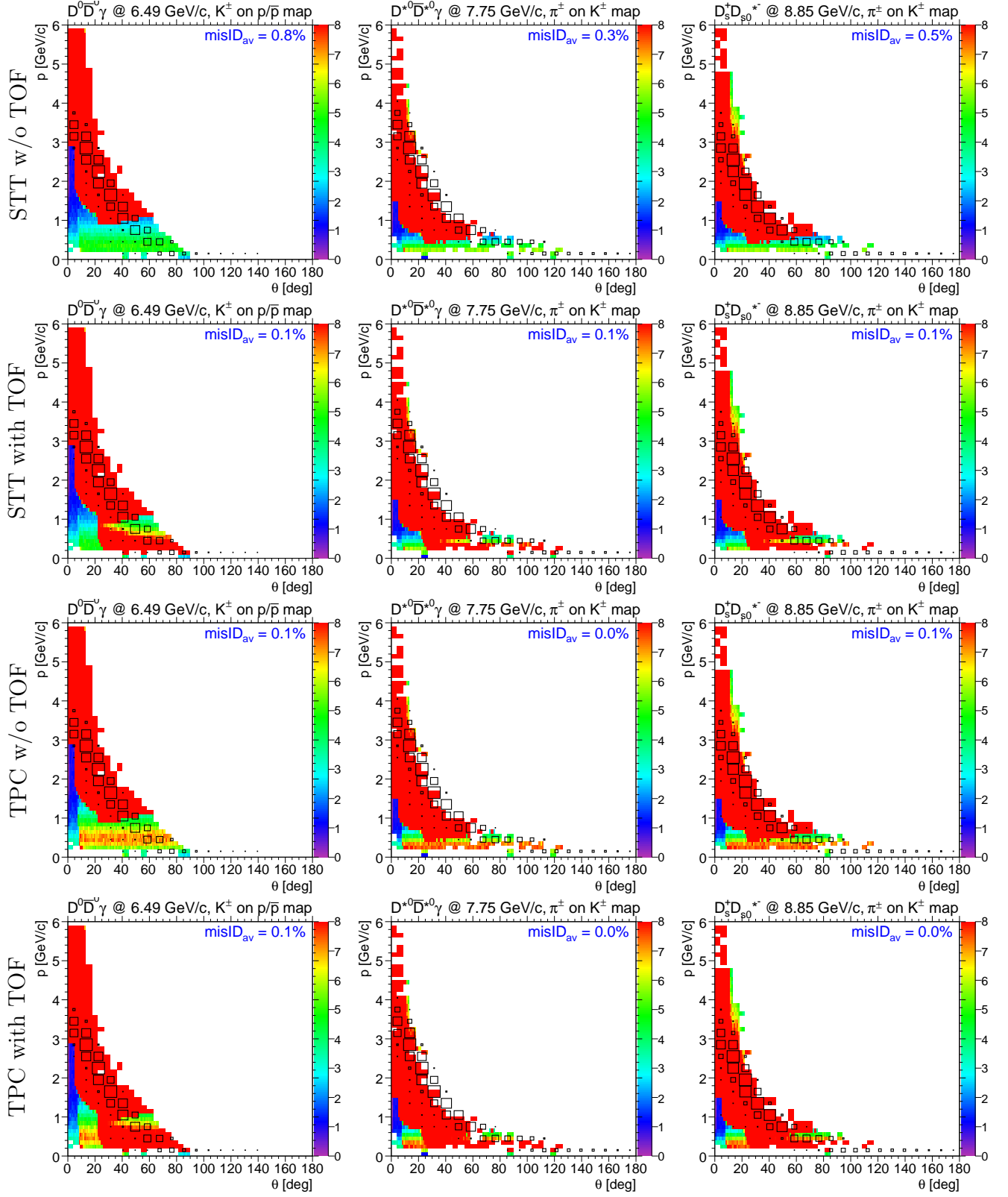


Figure 60: Projection of kinematic distributions on separation maps (2).

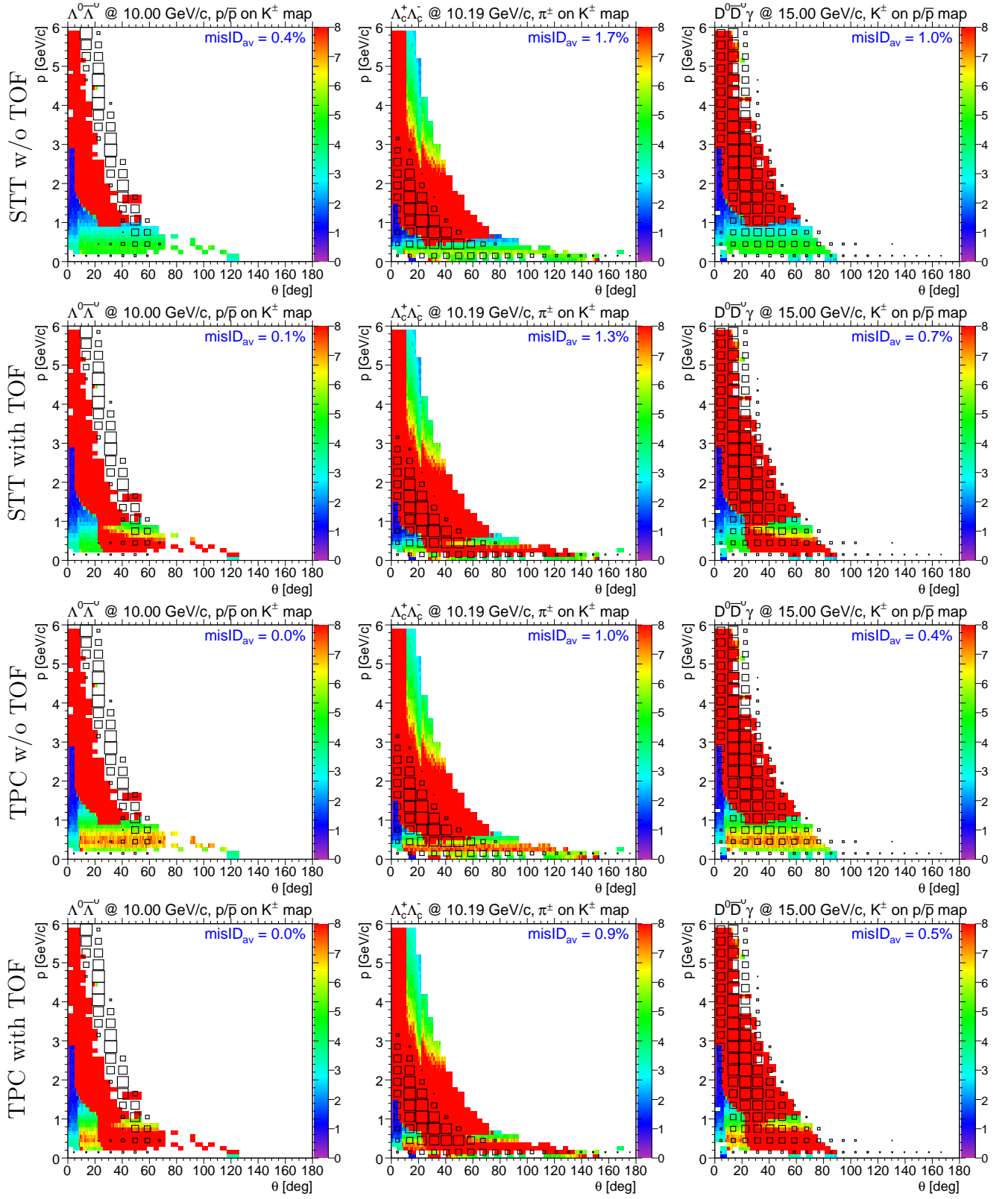


Figure 61: Projection of kinematic distributions on separation maps (3).

5.2 Crucial channels

As it can be seen clearly in tables 11 - 13, for a significant number of channels either the mis-identification fraction can be considered as large or the capabilities for the particular detector setups exhibit large differences. Since not all channels can be discussed in detail in this document only some of them will be commented on in the following paragraphs.

5.2.1 $\bar{p}p \rightarrow \Lambda^0 \bar{\Lambda}^0$ at 1.46 GeV/c (π/e), fig. 59

The pions of this signal reaction are distributed more or less isotropically with very low momenta. Since neither dE/dx nor t_{TOF} differs much between electrons and pions in this phase space region the mis-ID frations is about 5%. The scenario is a representative for all channels with very low energetic particles.

5.2.2 $\bar{p}p \rightarrow \Omega^- \bar{\Omega}^+$ at 4.954 GeV/c (p/K), fig. 59

Most noticable for this channel is its compact phase space distribution for protons in the region around $(p, \theta) = (1.5\text{GeV}/c, 5^\circ)$. Directly in that region the corresponding separation map exhibis some kind of 'hole' leading to a remarkable mis-ID level around 20% which is the highest value in the table. The origin of the hole is the requirement of 'positive identification', i. e. both particle species have to produce a signal in the relevant detectors. In this case the protons are below the Cherenkov threshold in the Disc DIRC and therefore are not separable from background kaons.

This issue might either be tackled with the planned forward TOF wall to be installed behind the dipole magnet or the usage of the Cherenkov devices in threshold mode under certain conditions.

5.2.3 $\bar{p}p \rightarrow D^0 \bar{D}^0 \gamma$ at 6.488 GeV/c (K/p), fig. 59

This channel is a good example for scenarios where the Barrel TOF system can add valuable information for the purpose of proton kaon separation. In particular with STT as the central tracker the mis-ID decreases by a factor of approximatly eight. In case of the TPC option this improvement vanishes since the dE/dx information can be expected to provide sufficiently powerful information for good identification.

5.2.4 $\bar{p}p \rightarrow \Lambda_c^+ \Lambda_c^-$ at 10.187 GeV/c (π/K), fig. 61

The pions originating form this baryonic channel cover a large part of the relevant phase space for π/K separation. The crucial region is the low momentum edge of the distributions below 400 MeV/c. Here it can be seen, that in case of the STT tracker option a Barrel TOF significantly improves the identification power. Obviously in this particular situation the dE/dx information of the TPC alone already provides superior identification potential than the combined information of STT and TOF.

6 Global PID Scheme

The PANDA spectrometer will feature a complete set of innovative detectors for particle identification. The detection of neutral particles will be performed by a highly granular electromagnetic calorimeter. Charged particles will be identified in the low momentum region by their energy deposit and ToF, in all other momentum regions by innovative DIRC detectors. The target spectrometer will be complemented by a forward spectrometer to detect high momentum particles and surrounding muon detectors. Each detector systems performance is optimised in itself. Studies have begun to combine the responses of various detectors in a common framework based on a likelihood scheme or a carefully trained neural network. These combined likelihood schemes are successfully employed at various detector systems like HERMEs, Belle and BaBar. They rely on a reliable parametrisation of the detector component response from simulation and test-beams. This has to be taken into account in testing PANDA's individual components. The combined performance of the system will be significantly better than the individual separation powers.

7 Conclusion

In this report of the Technical Assessment Group PID to the PANDA collaboration all informations to the planed sub detectors are collected as well as a method is introduced to define and evaluate the performance of detector parts and a complete detection system. Dimensions of detectors as well as their performance obtained with simulations of different level of detail are shown.

The Fast Simulation were introduced and the parameterization of the different PID processes and all known specific detector effects being the input for this simulation packet. Please note: The muon system was not included in the evaluation with the Fast Simulation as well as the complete performance of the electromagnetic calorimeter depending on many different parameters. The Forward ToF detector discussed in the text is also absent in the calculations.

With this tool the separation power, defined in the text, could be determined for each combination of two different particle species. The separation power was calculated for a fine binning of the solid angle θ covered (by each sub detector) and the momentum p of the produced particles. The number of sigma separation in each bin is indicated by a color code.

Please note: Only positive particle identification is shown. This means, in case one of the two particles did not overcome the threshold for Cherenkov radiation the separation power is zero. Thus, if one uses the Cherenkov detectors as threshold counters additional information is available.

The combination of the full detector results in a map of separation power over θ and p . In regions (bins) covered by more than one detector the global separation power was calculated as the quadratic sum of the separation power of the contributing detectors. Due to its higher sensitivity to small differences the separation power has been translated into the so called mis-identification level for the process of evaluation and comparison.

The connection to the envisaged physics is achieved by comparing phase space plots over θ and p with the map of separation power, whereas the only interesting regions are that where the signal overlaps with the background particles.

In this report for all PANDA relevant physics channels and its relevant background channels phase space plots were produced and the overlap regions were determined.

Only for these regions the average fraction of mis-identification was determined. For all four scenarios (STT, STT+ToF, TPC and TPC+ToF) of detector setups a factor relative to the above value has been computed. These numbers allow to see and judge the performance of the four options.

Thus the results of the evaluation could be shown by a table which contains the reaction channels exceeding a level of mis-identification defined in the report. Only critical reactions were represented by plots, some were discussed in more detail.

Is has to be noted again: The report is based on a Fast Simulation. This means that for the results no microscopic simulation was done. The PID processes were parameterized and some estimations were done for simplification or since no better knowledge was available.

This document provided by the PID TAG of PANDA should serve as a tool to evaluate the detector setup for an optimal global PID performance. On the one hand side the numbers arrived for the separation power of different setups and reactions give the possibility to compare the value of alternative sub detectors or additional detector parts. On the other hand and maybe

1366 more important, the methods explained here can be used for further studies and specific questions
1367 having particular reactions as well as more detailed and evolved detector setups.

1368 The PID TAG gives no recommendations but numbers and a clue how to read them. They are
1369 strong and serve as a basis for decisions to be taken by the PANDA collaboration.

1370 **8 Acknowledgments**

1371 Thanks to the analyzers from the "PANDA Physics Book", and all who help with their work and
1372 expertise to the success of the PID TAG. It should be emphasized the effort done by Klaus Gtzen
1373 to produce in iterative steps with the input from the PID TAG members and own ideas the maps
1374 of separation power.

1375 This work is supported by EU FP6 grant, contract number 515873, DIRACsecondary-Beams.

References

- [1] $\bar{\text{PANDA}}$ Collaboration, Technical Progress Report, FAI R-ESAC/Pbar 2005
- [2] <http://panda-wiki.gsi.de/cgi-bin/viewauth/Tagpid/WebHome>, Wiki page of the $\bar{\text{PANDA}}$ PID TAG
- [3] $\bar{\text{PANDA}}$ Collaboration, $\bar{\text{PANDA}}$ Physics Book, in progress
- [4] F. Sauli, Nucl. Instrum. Meth. **A386**, 531 (1997)
- [5] <http://cnlart.web.cern.ch/cnlart/237/Pr/garfield.html>
- [6] A. Akindinov, A. Martemiyarov, V. Plotnikov, et al., Preprint ITEP 16-04
- [7] "The HARP resistive plate chambers: Characteristics and physics performance", V.Ammosov et al., NIM **A578** (2007) 119-138
- [8] "Four glass RPC as a candidate to a large area thin time-of-flight detector", V.Ammosov et al., preprint IHEP 2002-10, Protvino 2002
- [9] "Prototype Performance on Novel Muon Telescope Detector at STAR", Lijuan Ruan (for the STAR), 24th Winter Workshop on Nuclear Dynamics, South Padre, USA, April 5-12 2008
- [10] IHEP+JINR proposal, PANDA Workshop, ITEP, Moscow, April 17-18 2008,
[http : //www - panda.gsi.de/html/panda_russia/HARP_PANDA_ITEP.ppt](http://www-panda.gsi.de/html/panda_russia/HARP_PANDA_ITEP.ppt)
- [11] ALICE Collaboration, Time-of-flight system, ALICE TDR 8, CERN/LHCC 2000-12
- [12] A. Akindinov, V. Golovine, A. Martemianov, et al., Nucl. Instr. and Meth. A 494 (2002) 474-479
- [13] R. Aleksan et al., Nucl. Inst. Meth. **A397**, 261 (1997)
- [14] <http://www.zemax.com>
- [15] A. Galoyan, V.V. Uzhinsky, AIP Conf. Proc. 796, pp. 79-8 2, 2005
- [16] $\bar{\text{PANDA}}$ Collaboration, Technical Design Report for the $\bar{\text{PANDA}}$ Electromagnetic Calorimeter, in preparation
- [17] D. I. Glazier, to be published in proceedings of the XIII International Conference on Calorimetry in High Energy Physics (CALOR08), by Journal of Physics: Conference Series
- [18] P. Schönmeier et al., to appear in the proceedings of 6th International Workshop on Ring Imaging Cherenkov Counters (RICH 2007), Trieste, Italy, 15-20 Oct 2007.
- [19] The HERMES Dual-Radiator Ring Imaging Cerenkov Detector, N. Akopov et al. Nucl. Instrum. Meth. A479:511-530, 2002
- [20] A Review of recent techniques of TOF detectors, M. Bonesini, Publ. in Como 2003, Astroparticle, particles and space physics, detectors and medical physics applications, 455-461

- 1408 [21] Characterization of the HADES spectrometer in PP collisions at 2.2 GeV: Elastic Scattering
1409 and Eta reconstructions. Stefano Spataro PhD thesis.
- 1410 [22] W.-M. Yao et al. 2006 J. Phys. G: Nucl. Part. Phys. **33** 1
- 1411 [23] G.S. Atayan et al., Nucl. Instrum. Meth. **A320**, 144 (1992)
- 1412 [24] G. Atayan et al., Test beam study of the KOPIO Shashlyk calorimeter prototype, in *Proceed-*
1413 *ings of "CALOR 2004"*, 2004
- 1414 [25] Acta Phys. Polon. **B38**, 899 (2007)
- 1415 [26] T.C. Awes et al., Nucl. Instrum. Meth. **279**, 479 (1989)
- 1416 [27] G.D. Alexeev, presentation prepared for the $\overline{\text{PANDA}}$ Coll. Meeting in Cracow, June 2008

1417 9 Appendix

1418 Members of the PID TAG

- 1419 • G. Schepers, C. Schwarz - Barrel Dirc (Chairs)
- 1420 • Rene Jaekel - MVD
- 1421 • B. Kopf, R. Novotny - Barrel Calorimeter
- 1422 • B. Seitz - Cherenkov Counter (Global PID)
- 1423 • O. Denisov, M. P. Bussa - Muon Counter
- 1424 • K. Föhl, A. Hayrapetyan - Endcap Cherenkov
- 1425 • J. Smyrski, A. Wronska - Forward Calorimeter
- 1426 • Q. Weitzel, S. Neubert - Time Projection Chamber
- 1427 • C. Schwarz, A. Galoyan - Time of Flight
- 1428 • K. Götzen - Fast Simulation
- 1429 • K. Peters - Physics

1430 Further very important contributions were made by:

- 1431 Bernhard Ketzer (TPC)
- 1432 Alberto Rotondi (STT)
- 1433 Michael Dueren, Markus Ehrenfried, Peter Vlasov (Endcap DISC)
- 1434 Ralf Kaiser, Guenther Rosner, Inti Lehmann, Matthias Hoek (Cherenkov Detector)
- 1435 Thierry Hennino, Martin Kotulla (EMC)
- 1436 Marco Maggiora, George Serbanut (Muon Counter)
- 1437 Piotr Hawranek (Forward Detectors)
- 1438 Alicia Sanchez, Stefano Spataro (Time of Flight Detector)
- 1439 Stanislav Belostotski, Vladimir Vikhrov, Yuri Naryshkin (Forward Time of Flight Detector)
- 1440 Lars Schmitt (physics)